CYCLONE AND COLD FRONT EVOLUTION OVER THE INTERMOUNTAIN WEST

by

Gregory Lucas West

A dissertation submitted to the faculty of
The University of Utah
in partial fulfillment of the requirements for the degree of

Doctor of Philosophy

Department of Atmospheric Sciences

The University of Utah

May 2011

STATEMENT OF DISSERTATION APPROVAL

The dissertation of **Gregory Lucas West**

has been approved by the following supervisory committee members:

W. James Steenburgh	, Chair	**12/14/2009** Date Approved
John D. Horel	, Member	**12/14/2009** Date Approved
Edward J. Zipser	, Member	**12/14/2009** Date Approved
Jan Paegle	, Member	**12/14/2009** Date Approved
Lance F. Bosart	, Member	**1/4/2009** Date Approved

and by **W. James Steenburgh** , Chair of the Department of **Atmospheric Sciences**

and by Charles A. Wight, Dean of The Graduate School.

ABSTRACT

Over the Intermountain West, cyclones and cold fronts can bring about dramatic sensible weather changes that impact the rapidly growing population of the region, yet the basic mechanisms contributing to their intensification and evolution are not well understood. This dissertation investigates these mechanisms using a multi-faceted approach that includes observational analysis, real-data model simulations, and idealized model simulations. Chapter 2 presents an observational analysis of the 15 Apr 2002 Tax Day Storm, which featured the strongest cyclone and cold front to pass through Salt Lake City, Utah in recent history. In particular, we establish the role of a newly identified feature, the Great Basin Confluence Zone (GBCZ), in cyclone and frontal evolution. This region of contraction (confluent deformation and divergence) extends downstream from the Sierra Nevada and is initially nonfrontal, but becomes the locus for frontogenesis and cyclogenesis. Chapter 3 uses real-data and idealized modeling studies to examine the role of the Sierra Nevada in Intermountain cold front evolution. Using model simulations of another strong case of Intermountain frontogenesis from 25 Mar 2006 with and without the Sierra Nevada, we show that the range produces a leeward warm anomaly, increasing the cross-front potential temperature contrast, and also enhances contraction along the front. Idealized baroclinic wave simulations in which we vary the initial cyclone position are used to show how the influence of the Sierra Nevada varies for differing synoptic patterns and frontal orientations. This work advances our understanding of the

mechanisms important to cyclone and frontal evolution over mountainous terrain and should contribute to improved analysis and forecasting of cyclones and fronts over the Intermountain West.

TABLE OF CONTENTS

ACKNOWLEDGMENTS

I would first like to thank my advisor, Dr. Jim Steenburgh, for his expert guidance and support throughout my graduate school career. His passion and drive to be the best scientist and advisor possible is apparent, and I thank him for the invaluable advice, insight, and knowledge he has imparted to me over the past several years. I would also like to thank my other committee members, Dr. Lance Bosart, Dr. John Horel, Dr. Jan Paegle, and Dr. Ed Zipser for their important insights and suggestions for improving this dissertation. Additional thanks go to the faculty and staff of the University of Utah Department of Atmospheric Sciences for providing a great education and experience, and to Kathy Roberts and Leslie Allaire for holding the department together.

Special thanks to Dr. Joseph Olson for his assistance in implementing the idealized initialization program in the WRF, Dr. John Horel and the MesoWest Group for providing MesoWest data, Dr. Sebastian Hoch for providing a meteogram plotting script, the University of Utah Center for High Performance Computing for computer support, Dan Tyndall for further computer support and general computer help, Erik Crosman for providing AVHRR satellite imagery, Dr. David Schultz and Dr. Robert Cohen for their insights in the use of contraction, the National Centers for Environmental Prediction for data, Don Murray, David Taylor, the Unidata Program Center for providing analysis and visualization software, and the Center for Ocean-Land-Atmosphere Studies/Institute of

Global Environment and Study for providing the Grid Analysis and Display System (GrADS).

I also thank my friends and fellow graduate students for their friendship, the good times, and the amazing adventures. I thank my girlfriend Lisa for her love, encouragement, and keeping me sane. Finally, I'm grateful to my family for their unconditional love and support, without which my graduate career and accomplishments certainly would not have been possible.

This research was supported by the National Oceanic and Atmospheric Administration/National Weather Service under a series of grants from the CSTAR program, and the National Science Foundation under grants ATM-0333525 and ATM-0628299.

CHAPTER 1

INTRODUCTION

Much of the adverse sensible weather that occurs over the Intermountain West in the cool season is associated with cyclones and their attendant cold fronts, which impact the region regularly (Petterssen 1956; Zishka and Smith 1980; Whittaker and Horn 1981; Lee 1995; Shafer and Steenburgh 2008, Jeglum 2010), and can bring, amongst other effects, high winds, heavy rain and snow, blowing dust, wild fire runs, and avalanches. For example, in the two events examined in this dissertation, there were reports of < ¼ mile visibility, downed trees and power lines, a roof blown off a house, blown over tractor-trailers, and millions of dollars in property damage (NCDC 2002, 2009; UAC 2009). These events occur over the most rapidly growing region in the United States (in 2008 Utah, Arizona, Idaho, and Nevada were the 1st, 2nd, 6th, and 8th fastest growing states, respectively; United States Census Bureau 2008).

Despite their relatively high frequency and the potentially large impacts of these events, research on the genesis and evolution of cyclones and cold fronts over the region has historically been limited to just a handful of studies (e.g., Conger 1994; Horel and Gibson 1994; Lee 1995), and our understanding and forecasting of these phenomena remains deficient, especially in comparison to other parts of the country (Junker et al. 1989; Junker et al. 1992; Hill 1993; McDonald 1998; Yuan et al. 2007). Consequently,

Prospectus Development Teams of the United States Weather Research Program advocate research to improve the understanding and forecasting of storms over the complex terrain of this region (Smith et al. 1997, Fritsch et al. 1998, Dabberdt et al. 2000).

Recent cyclone and cold front studies have benefitted from the high-density MesoWest observational network and higher-resolution gridded datasets. Most of these are case studies (e.g., Steenburgh and Blazek 2001; Schultz and Trapp 2003; Shafer et al. 2006; Steenburgh et al. 2009), describing in detail the observed evolution of cold fronts and related processes. While such case studies are vital to understanding phenomena, other techniques are often necessary to gain a more thorough understanding. Shafer and Steenburgh (2008) conduct a climatology of strong cold fronts over the region, establishing many of the characteristics and basic ingredients central to their formation, and outlining the important processes deserving of further investigation, like diabatic effects and the apparent influence of the Sierra Nevada. Steenburgh et al. (2009) take this next step, and, in addition to performing a detailed observational case study of discrete propagation of a frontal system across the Sierra-Cascade Ranges, use numerical simulations, including a "fake-dry" sensitivity run. They show that diabatic processes were not responsible for the discrete propagation, but likely contributed to the intense sharpening of the observed cold front over northern Nevada.

The purpose of this dissertation is to further advance our knowledge and understanding of Intermountain cyclones and fronts, especially with respect to the influence of the Sierra Nevada on frontal dynamics and evolution. Chapter 2 provides a detailed case study of the structure and evolution of Tax Day Storm (15 Apr 2002), which

featured the strongest frontal and second strongest cyclone to impact Salt Lake City, Utah in recent history. The study highlights the role of a previously undocumented airstream boundary, which we call the *Great Basin Confluence Zone* (GBCZ) in frontal evolution, and also examines diabatic contributions to frontal development and front-mountain interactions over northern Utah.

The first section of Chapter 3 investigates the role of the Sierra Nevada in the evolution of another strong cold front on 25 Mar 2006 through a terrain sensitivity study using the Weather Research and Forecasting model. The second section of this chapter also employs the Weather Research and Forecasting model, initializing an idealized cyclone at various latitudes, and comparing the resulting frontal interactions with the orography of the western United States.

The paper closes with Chapter 4, the Concluding Remarks, which summarizes the key findings of these studies, and provides suggestions for future work.

References

Conger, M. C., 1994: Forecasting a Great Basin cyclogenic event using the Nested Grid Model: A case study evaluation of model performance. *Natl. Wea. Digest*, **18,** 4, 2-15.

Dabberdt, W. F., and coauthors, 2000: Forecast issues in the urban zone: Report of the 10th Prospectus Development Team of the U.S. Weather Research Program. *Bull. Amer. Meteor. Soc*., **81,** 2047-2064.

Fritsch, J. M., and coauthors, 1998: Quantitative precipitation forecasting: Report of the Eighth Prospectus Development Team, U. S. Weather Research Program. *Bull. Amer. Meteor. Soc*., **79,** 285-299.

Hill, C. D., 1993: Forecast problems in the western region of the National Weather Service: An overview. *Wea. Forecasting*, **8**, 158-165.

Horel, J. D., and C. V. Gibson, 1994: Analysis and simulation of a winter storm over Utah. *Wea. Forecasting*, **9**, 479-494.

Jeglum, M. E., 2010: Multi-Scale Reanalysis Climatology of Intermountain Cyclones. M. S. thesis, Department of Atmospheric Sciences, University of Utah, 59 pp.

Junker, N. W., J. E. Hoke, and R. H. Grumm, 1989: Performance of NMC's regional models. *Wea. Forecasting*, **4**, 368-390.

Junker, N. W., J. E. Hoke, B. E. Sullivan, K. F. Brill, and F. J. Hughes, 1992: Seasonal and geographic variations in quantitative precipitation prediction by NMC's nested-grid model and medium-range forecast model. *Wea. Forecasting*, **7**, 410-429.

Lee, T. P., 1995: Intermountain cyclogenesis: A climatology and multiscale case studies. Ph.D. Dissertation, Department of Atmospheric Sciences, State University of New York at Albany, 399 pp.

McDonald, B. E., 1998: Sensitivity of precipitation forecast skill to horizontal resolution. Ph.D. Dissertation, Dept. of Meteorology, University of Utah, 135 pp.

NCDC, 2002: *Storm Data*, Vol. 44, No. 4, 276 pp

NCDC, 2009: Storm Events. [Retrieved online 1 Dec 2009 at http:// www4.ncdc.noaa.gov/cgi-win/wwcgi.dll?wwEvent~Storms].

Petterssen, S., 1956: *Weather Analysis and Forecasting.* Vol. 1, *Motion and Motion Systems*, 2d ed., McGraw-Hill, 428 pp.

Schultz, D. M., and R. J. Trapp, 2003: Nonclassical cold-frontal structure caused by dry subcloud air in northern Utah during the Intermountain Precipitation Experiment (IPEX). *Mon. Wea. Rev*., **131**, 2222–2246.

Shafer, J. C., and W. J. Steenburgh, 2008: Climatology of strong Intermountain cold fronts. *Mon. Wea. Rev*., **136**, 784-807.

Shafer, J. C., W. J. Steenburgh, J. A. W. Cox, and J. P. Monteverdi, 2006: Terrain influences on synoptic storm structure and mesoscale precipitation distribution during IPEX IOP3. *Mon. Wea. Rev*., **134**, 478-497.

Smith, R., and coauthors, 1997: Local and remote effects of mountains on weather: Research needs and opportunities. *Bull. Amer. Meteor. Soc*., **78,** 877-892.

Steenburgh, W. J., and T. R. Blazek, 2001: Topographic distortion of a cold front over the Snake River Plain and central Idaho Mountains. *Wea. Forecasting*, **16**, 301–314.

Steenburgh, W. J., C. R. Neuman, G. L. West, and L. F. Bosart, 2009: Discrete frontal propagation over the Sierra-Cascade Mountains and Intermountain West. *Mon.*

Wea. Rev., **137**, 2000-2020.

UAC, 2009: Snow and Avalanches in Utah Annual Report 2005-2006. [Retrieved online at http://utahavalanchecenter.org/files/annual_reports/uac/AnnualReport05-06.pdf].

Whittaker, L. M., and L. H. Horn, 1981: Geographical and seasonal distribution of North American cyclogenesis, 1958-1977. *Mon. Wea. Rev.,* **109**, 2312-2322.

Yuan, H., S. L. Mullen, X. Gao, S. Sorooshian, J. Du, and H.-M. H. Juang, 2007: Short-range probabilistic quantitative forecasts over the southwest United States by the RSM ensemble system. *Mon. Wea. Rev.,* **135,** 1685–1698.

Zishka, K. M., and P. J. Smith, 1980: The climatology of cyclones and anticyclones over North America and surrounding ocean environs for January and July, 1950–77. *Mon. Wea. Rev.,* **108**, 387-401.

CHAPTER 2[1]

LIFE CYCLE AND MESOSCALE FRONTAL STRUCTURE OF AN INTERMOUNTAIN CYCLONE

Abstract

High-resolution analyses and MesoWest surface observations are used to examine the life cycle and mesoscale frontal structure of the "Tax Day Storm," an Intermountain cyclone that produced the second lowest sea level pressure observed in Utah during the instrumented period and strongest cold frontal passage at the Salt Lake City International Airport in the past 25 years. A key mesoscale surface feature contributing to the cyclone's evolution is a confluence zone that extends downstream from the Sierra Nevada across the Great Basin. Strong contraction (i.e., deformation and convergence) within this *Great Basin Confluence Zone* (GBCZ) forms an airstream boundary that is

[1]Chapter 2 is reprinted from West and Steenburgh (2010).

initially non-frontal, but becomes the locus for surface frontogenesis as it collects and concentrates baroclinity from the northern Great Basin, including that accompanying an approaching baroclinic trough. Evaporative and sublimational cooling from postfrontal precipitation, as well as cross-front contrasts in surface sensible heating also play an important role, accounting for up to 40% of cross-front baroclinity. As an upper-level cyclonic potential vorticity anomaly and quasi-geostrophic forcing for ascent move over the Great Basin, cyclone development occurs along the GBCZ and developing cold front rather than within the Sierra Nevada lee trough, as might be inferred from classical models of lee cyclogenesis. Front-mountain interactions ultimately produce a very complex frontal evolution over the basin-and-range topography of northern Utah.

The analysis further establishes the role of the GBCZ in Intermountain frontogenesis and cyclone evolution. Recognition of this role is essential for improving the analysis and prediction of sensible weather changes produced by cold fronts and cyclones over the Intermountain West.

Introduction

The Tax Day Storm of 15 Apr 2002 produced the second lowest sea level pressure observed in Utah since observational records began in 1892 and the strongest cold-frontal passage at the Salt Lake City International Airport (KSLC; locations of stations and geographical features shown in Fig. 2.1) in 25 years (Shafer and Steenburgh 2008, hereafter SS08; based on 2-h temperature fall). Cyclones such as the Tax Day Storm traverse the Intermountain West several times per year (Petterssen 1956; Zishka and Smith 1980; Whitaker and Horn 1981; Lee 1995; Jeglum 2010) and can be accompanied

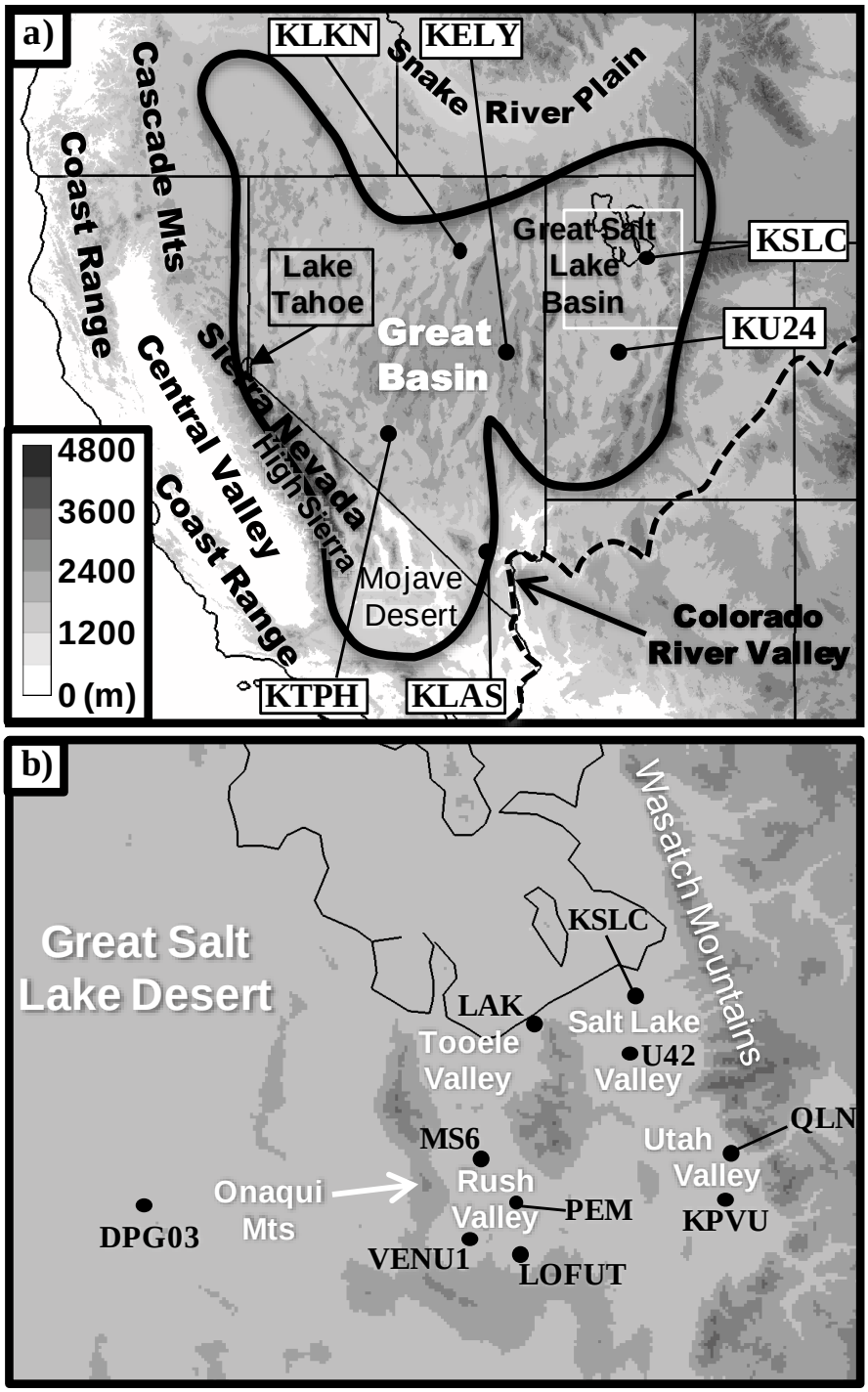

Figure 2.1. Geographic overview. Topography and geography of (a) the Intermountain West and surrounding region [outline of Great Basin from United States Geological Survey National Wetlands Research Center (2010) indicated by thick line] and (b) the northern Utah study area [indicated by the white box in (a)]. Terrain height (m) shaded according to scale at lower left in (a). Geographic features and observing stations discussed in text annotated.

by strong fronts, high winds (> 30 m s^{-1}), power outages, blowing dust, dramatic temperature falls, wild fire runs, and/or heavy snow (SS08). Unfortunately, our understanding of these events is limited (Hill 1993) and, in general, forecast skill is lower over the Intermountain West than other regions of the United States (Junker et al. 1989; Junker et al. 1992; McDonald 1998; Yuan et al. 2007).

Intermountain cyclogenesis is a likely consequence of flow interaction with the Sierra Nevada and Cascade Mountains, which form the western boundary of the region (Fig. 2.1a). In particular, the southern portion of the Sierra Nevada, known as the *high Sierra*, forms a formidable quasi-continuous barrier 3000–4000 m in elevation. Downstream, basin-and-range topography dominates the Intermountain West, with hundreds of narrow, steeply sloped mountain ranges separated by broad alluvial basins and valleys. These ranges greatly complicate analysis and forecasting across the region.

Remarkably few studies, however, have examined Intermountain (a.k.a. Nevada) cyclogenesis. The most comprehensive is Lee (1995) who found that 75% of Intermountain cyclones form in southwesterly to westerly large-scale flow, which hydrostatically induces a surface trough to the lee of the Sierra Nevada. Cyclogenesis occurs as quasi-geostrophic (QG) forcing for ascent moves over lee trough. This evolution is broadly consistent with the view of lee cyclogenesis as a two-stage process, the first being the formation of a lee trough as cross-barrier flow develops in advance of an upper-level cyclonic potential vorticity (PV) anomaly (e.g., Buzzi and Tibaldi 1978; McGinley 1982; Tibaldi et al. 1990; Aebischer and Schär 1998). The second involves the slower, quasi-stationary intensification of the cyclone, as the upper-level cyclonic PV anomaly overtakes the lee trough. Surface development can be inferred through QG

forcing for ascent (Hoskins et al. 1978), which stretches low-level vorticity within the lee trough, or as the phase locking of an upper-level cyclonic PV anomaly with a low-level cyclonic PV maximum manifest as a surface warm anomaly in the lee of the barrier (e.g., Hoskins et al. 1985; Bleck and Mattocks 1984; Mattocks and Bleck 1986). Theoretical studies suggest that this two-stage process is a reflection of baroclinic wave interaction with orography (e.g., Smith 1984; Tibaldi et al. 1990; Bannon 1992; Davis 1997; Davis and Stoelinga 1999).

The frontal life cycle of Intermountain cyclones also remains largely unexplored. The first coherent model of mid-latitude cyclone evolution was developed by the Bergen School early in the 20th century and features the amplification of a frontal wave into an open-wave cyclone, culminating in the formation of an occluded front as the cold front overtakes the warm front (Bjerknes 1919; Bjerknes and Solberg 1922). Although some cases roughly follow this evolution (e.g., Bergeron 1959; Schultz and Mass 1993; Market and Moore 1998; Martin 1998; Schultz et al. 1998), countless deviations have been documented, many of which are related to orography (e.g., Bergeron 1937; Steinacker 1982; Schultz and Mass 1993; Steenburgh and Mass 1994; Hobbs et al. 1996; O'Handley and Bosart 1996; Locatelli et al. 2002; Chien and Kuo 2006).

In one of the few studies of the frontal life cycle of cyclones over the Intermountain West, Horel and Gibson (1994) describe the role of orographic lift in the formation of a warm-core seclusion accompanying a deep tropospheric cyclonic circulation. Beyond this, knowledge of Intermountain cyclone evolution has been limited historically by a lack of observations with sufficient spatial and temporal resolution to identify large-scale airmass and circulation changes generated by the region's complex

terrain (Steenburgh and Blazek 2001). Recently, however, the development of the high-density MesoWest cooperative networks (Horel et al. 2002), execution of field programs like the Intermountain Precipitation Experiment (Schultz et al. 2002), and advancement of high-resolution data assimilation and numerical modeling has enabled the detailed study of several Intermountain cold fronts (e.g., Steenburgh and Blazek 2001; Schultz and Trapp 2003; Shafer et al. 2006; SS08; Steenburgh et al. 2009). In particular, SS08 identify a dramatic increase in the frequency of strong cold frontal passages between the Sierra-Cascade ranges and northern Utah. This increase appears to be related to the development of an area of confluence that develops downstream of the Sierra Nevada in large-scale southwesterly flow (hereafter the *Great Basin Confluence Zone*, GBCZ) and initiates and/or enhances frontogenesis. Steenburgh et al. (2009) show that the GBCZ can also contribute to discrete frontal propagation.

This paper uses high-resolution analyses and MesoWest surface observations to describe the life cycle and frontal evolution of the Tax Day Storm. In particular, we identify the role of the GBCZ in frontal development and cyclogenesis, examine the contribution of diabatic processes to frontogenesis, and describe the complex frontal evolution that ultimately occurs over the basin-and range topography of northern Utah.

Data and Methods

Our analysis employs manual surface analyses, objective upper-air and surface analyses, and satellite and radar imagery. Manual surface analyses use MesoWest observations (Horel et al. 2002), which were quality controlled following Splitt and Horel (1998), with further subjective checks for spatial and temporal consistency during manual analysis. To limit pressure reduction artifacts, we use 1500-m pressure (calculated

following Steenburgh and Blazek 2001) instead of sea level pressure since 1500 m is near the mean elevation of Intermountain observing sites. Following Sanders (1999), we use the term *front* to denote the warm edge of a strong baroclinic zone accompanied by a wind shift and pressure trough, and *baroclinic trough* for a surface feature with a wind shift and/or pressure trough but relatively weak temperature contrast. Following Cohen and Kreitzberg (1997), we classify the GBCZ as an *airstream boundary* because it is a wind shift line separating two relatively distinct airstreams.

Many of the challenges associated with surface analysis (e.g., Sanders 1999) are exacerbated by the topography and climatology of the Intermountain West (e.g., Rossby 1934, Hill 1993; Schultz and Doswell 2000; Steenburgh and Blazek 2001). In particular, thermally and dynamically driven winds, valley and basin cold pools, and large diurnal temperature cycles complicate frontal analysis. Relying on an objective temperature or potential temperature gradient criteria for distinguishing between fronts, baroclinic troughs, and non-frontal troughs can be problematic, but, in general, mobile fronts identified in this study are accompanied by a spatially and temporally coherent temperature change of *at least* 3°C $(2\ h)^{-1}$ [for comparison, SS08 use 7°C $(2\text{-}3\ h)^{-1}$ criteria to identify a *strong cold front*)], whereas quasi-stationary fronts are accompanied by a temperature gradient of *at least* 8°C $(110\ km)^{-1}$ [following the definition of a *strong front* given by Sanders (1999)]. We use temperature tendency and gradient criteria to extract the maximum amount of information from the spatially and temporally heterogeneous MesoWest network. For example, in some regions observation density is low or there is a lack of stations at a similar elevation, making estimates of the horizontal temperature gradient near the front difficult (many MesoWest stations do not report pressure,

precluding the calculation of potential temperature). In these regions, a station reporting at a high temporal frequency may enable identification of the intensity of mobile fronts.

Objective surface analyses are based on a version of the Advanced Regional Prediction System Data Assimilation System (ADAS; Brewster 1996; Xue et al. 2000, 2001, 2003) that was modified at the University of Utah to produce improved surface analyses over complex terrain (Lazarus et al. 2002; Myrick et al. 2005). The ADAS analyses, generated on a 5-km grid, assimilate MesoWest surface observations, with the operational Rapid Update Cycle (RUC2; Benjamin et al. 2004), available on a 20-km grid, serving as a downscaled background analysis. The resulting ADAS analyses are interpolated to a 0.41° x 0.35° (~40-km) lat/lon grid to provide a smoother analysis for presentation and diagnostic calculations. Subjective analyses of fronts, troughs, and airstream boundaries are overlaid on these plots for ease of interpretation. Trajectories and their related thermodynamic budgets are calculated from the interpolated ADAS analyses using a modified version of the traj.gs script from the Grid Analysis and Display System (GrADS) Script Library (available online at http://www.iges.org/grads/gadoc/library.html). Although these trajectories are two-dimensional and confined to the surface, which limits accuracy compared to three-dimensional trajectories, they are still representative of the general airflow due to the high spatial and temporal resolution of the data, and the relatively short trajectory time (e.g., Haagenson et al. 1990). Comparison of trajectories and thermodynamic budgets computed using the interpolated analyses and the original 5-km analyses shows they are quantitatively and qualitatively similar.

Upper-air analyses from the RUC2 are interpolated to the same 0.41° x 0.35° lat/lon grid as the ADAS for presentation clarity. These RUC2 analyses are further

smoothed using a 19-point rectangular diffraction function (Blackman and Tukey 1958; Barnes et al. 1996) to filter out wavelengths below ~700 km before calculating the QG forcing for ascent from the **Q**-vector form of the omega equation (Hoskins et al. 1978, Hoskins and Pedder 1980):

$$\omega \propto 2\boldsymbol{\nabla} \cdot \boldsymbol{Q}, \tag{1}$$

where ω is the vertical velocity in isobaric coordinates, and

$$\boldsymbol{Q} = -\left(\frac{g}{\theta_0}\right)\left[\left(\frac{\partial \boldsymbol{V}_g}{\partial x} \cdot \boldsymbol{\nabla}\theta\right)\hat{\imath} + \left(\frac{\partial \boldsymbol{V}_g}{\partial y} \cdot \boldsymbol{\nabla}\theta\right)\hat{\jmath}\right] \tag{2}$$

is the **Q**-vector.

Composite radar/satellite imagery analyses are generated by overlaying NEXRAD Level-II lowest-elevation scan (0.5°) radar reflectivity analyses from all available western United States radars on 4-km GOES infrared satellite imagery. It is important to note that radar coverage in many portions of the western United States is deficient or incomplete (Westrick et al. 1999; Maddox et al. 2002). This is especially true over portions of central Nevada and central Utah.

Results

Synoptic and Mesoscale Overview

At 0000 UTC (times are for 15 Apr 2002 unless otherwise stated), west-southwesterly flow in advance of an upper-level cyclonic potential vorticity (PV) anomaly and trough extends over the Pacific Northwest and Idaho (Fig. 2.2a). At 700 hPa, QG forcing for ascent lies over a broad area of northern California and northeast Nevada (Fig. 2.2b), just north of two weak 1500-m low centers (Fig. 2.3a). A third 1500-m low center, a so-called thermal low, lies over the Mojave Desert, as is common during the warm season (Rowson and Colucci 1992; Whiteman 2000, p. 165).

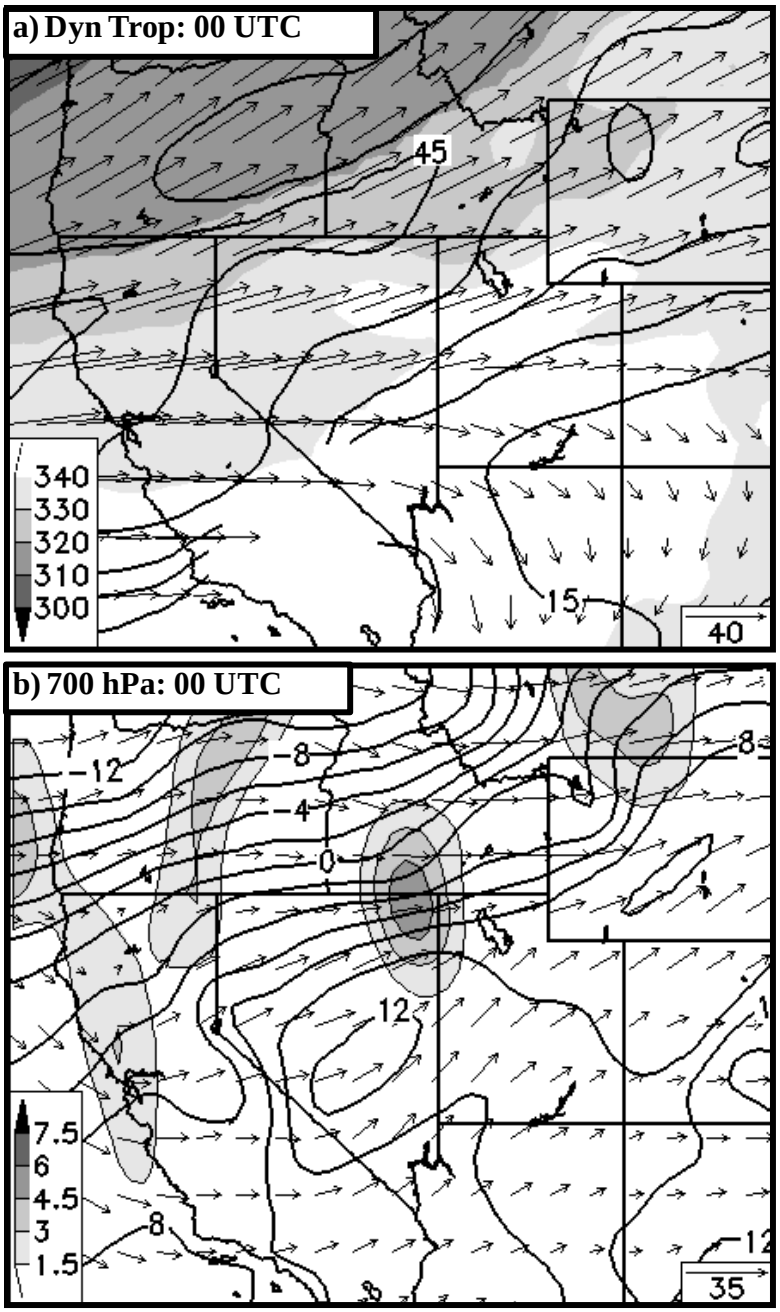

Figure 2.2. Synoptic analyses. (a) RUC2 dynamic tropopause (2 PVU) pressure (hPa, shaded following inset scale), wind vectors (m s^{-1}, following inset scale), and isotachs (contoured every 7.5 m s^{-1}). (b) RUC2 700-hPa temperature (contoured every 2°C), wind vectors (m s^{-1}, following inset scale), and 700-hPa QG forcing for ascent (x10^{-15} K m^{-2} s^{-1}, shaded following inset scale). (c) ADAS surface analysis with terrain height (m, shaded following inset scale), potential temperature (contoured every 2 K), wind vectors (m s^{-1}, following inset scale), and manual frontal analysis at 0000 UTC 15 Apr.

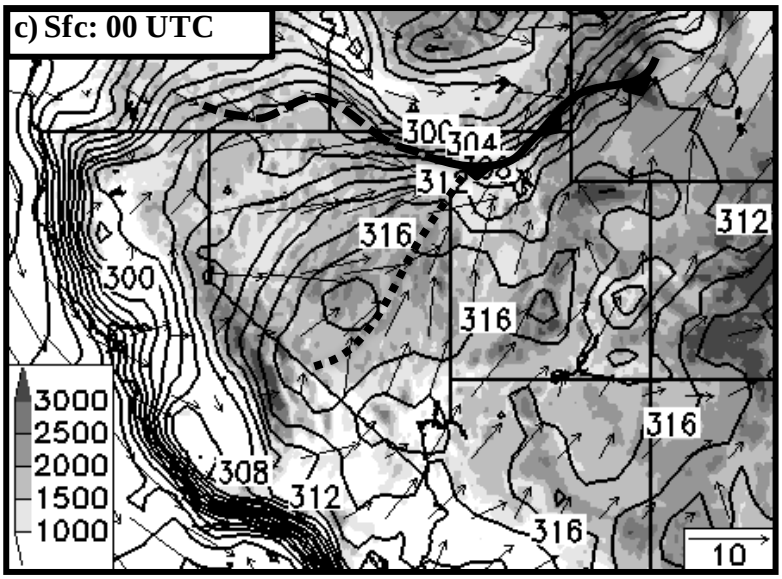

Figure 2.2. continued.

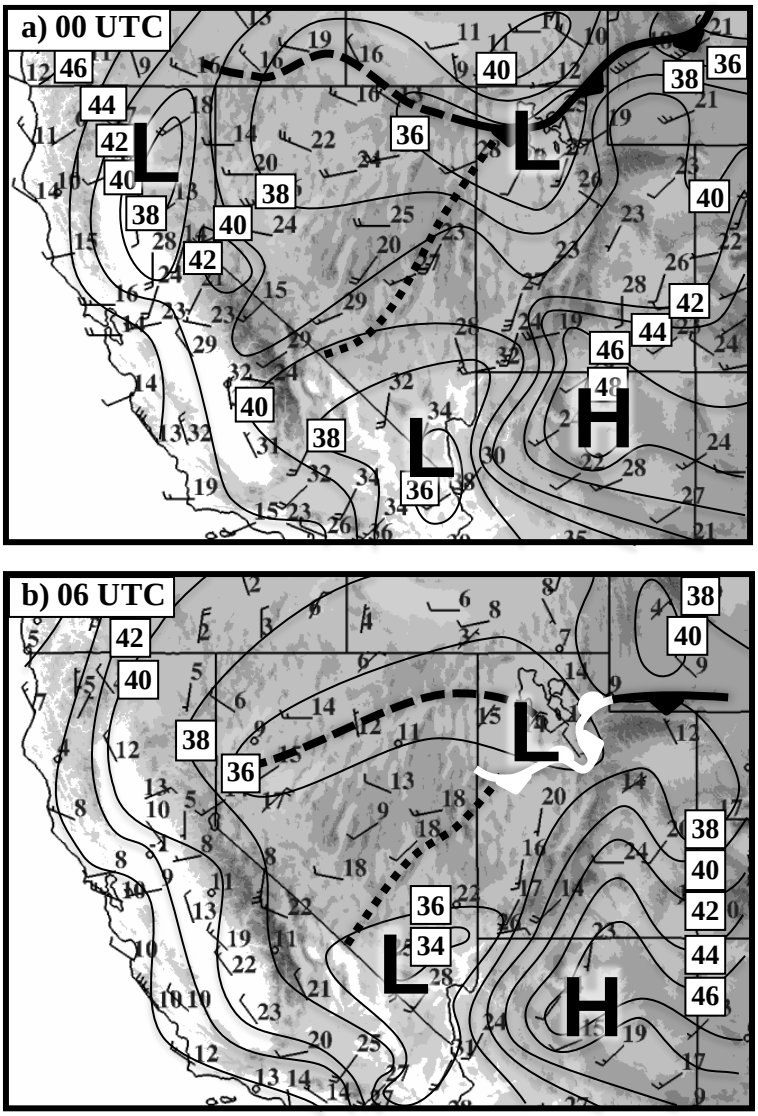

Figure 2.3. Regional surface analyses. Manual analysis of 1500-m pressure (every 2 hPa with leading 8 omitted) and surface frontal analyses at (a) 0000, (b) 0600, (c) 1200, (d) 1800, and (e) 2100 UTC 15 Apr. Cold, warm, and stationary fronts identified with traditional symbols (stationary fronts white). GBCZ and baroclinic trough denoted with dotted and dashed line, respectively. Surface station models include wind (pennant, full barb, and half barb denote 25, 5, and 2.5 m s^{-1}, respectively) and temperature (°C, at upper right).

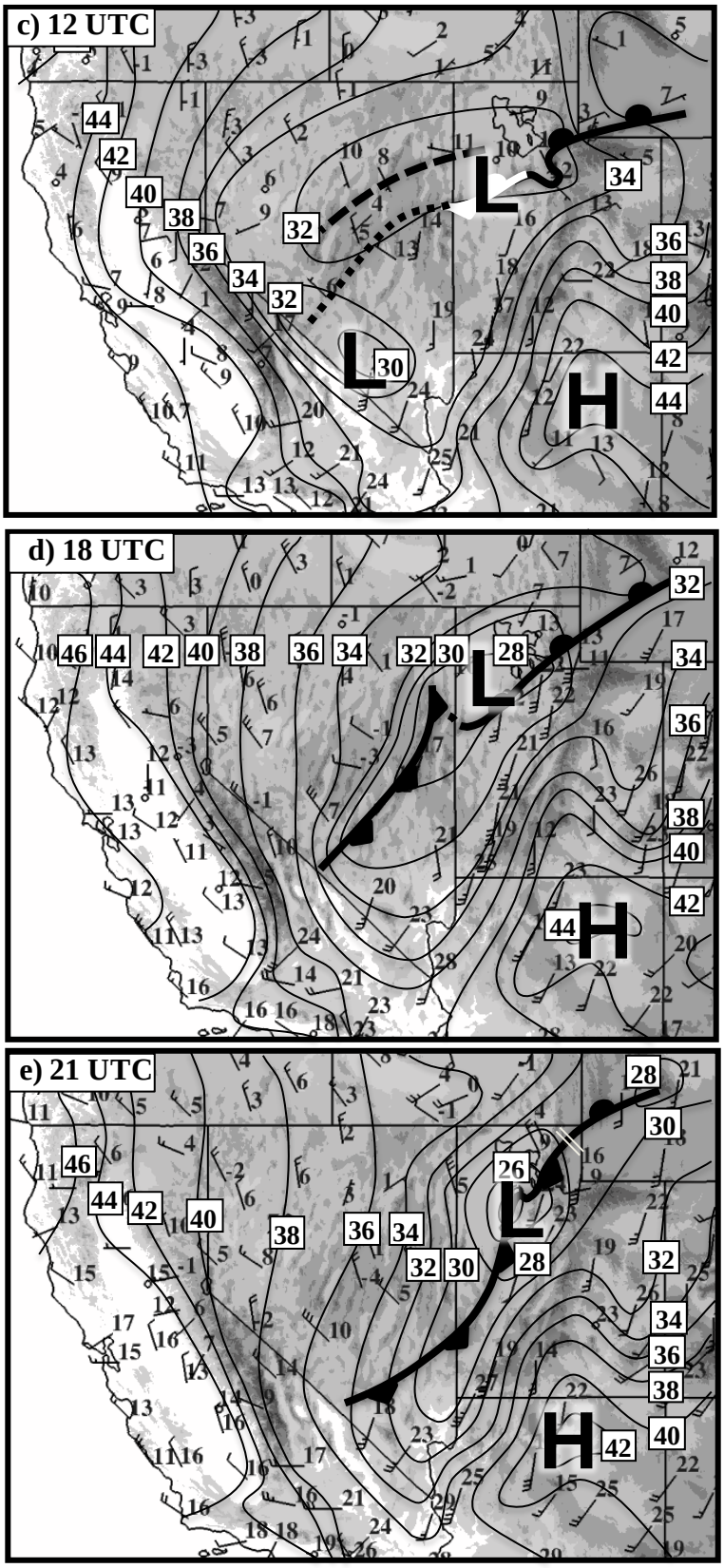

Figure 2.3 continued.

A surface-based cold front is advancing southward through southwest Wyoming and northern Utah (Fig. 2.3a), bringing temperature falls as large as ~10°C $(2\ h)^{-1}$ (e.g., DPG03, Fig. 2.4a; station locations in Fig. 2.1b). Differential surface sensible heating arising from inhomogeneous cloud cover may have contributed to frontal sharpening in this region, as described by Koch et al. (1995, 1997), Gallus and Segal (1999), and Segal et al. (2004). For example, the presence of a deep convective boundary layer at KSLC (32°C surface dew point depression, Fig. 2.5) indicates intense pre-frontal surface heating; whereas cloud cover (Fig. 2.6a) likely limited such heating in the post-frontal environment (no soundings are available in this region). Sublimational and evaporative cooling produced by post-frontal precipitation (Fig. 2.6a) may also have contributed to frontal sharpening, as often occurs with Intermountain cold fronts (e.g., Schultz and Trapp 2003; Steenburgh et al. 2009).

A more complex pattern exists farther to the west where the surface baroclinity is weaker but somewhat enhanced in two areas (Figs. 2.2c and 2.3a). The first is immediately north of a baroclinic trough near the northern Nevada border. A lack of post-frontal clouds and precipitation (Fig. 2.6a) may explain the less abrupt nature of the temperature transition in this region compared to further east. The second area of enhanced baroclinity extends across Nevada between the baroclinic trough and a pronounced confluence zone that extends downstream from the high Sierra into northwest Utah (Figs. 2.2c and 2.3a). This *Great Basin Confluence Zone* (GBCZ) represents an airstream boundary between southerly flow over southeastern Nevada and western Utah and westerly flow over central Nevada, and is embedded within a broad

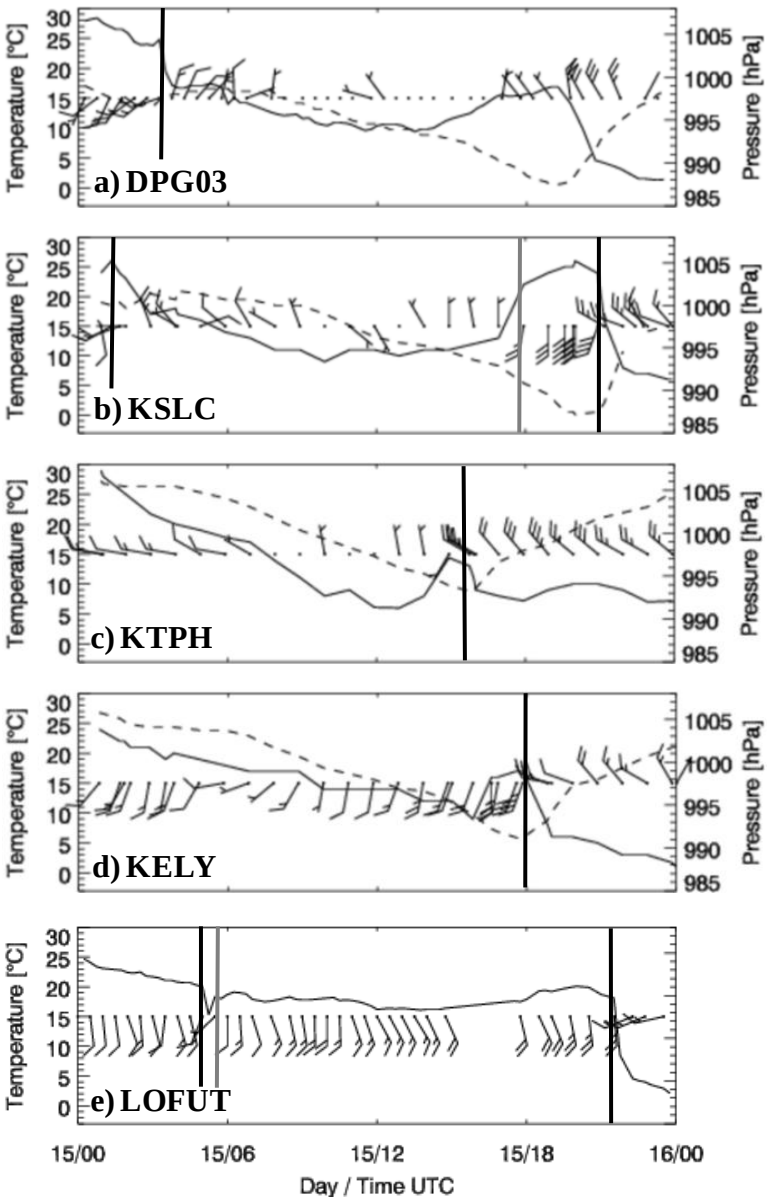

Figure 2.4. Surface station meteograms. Meteograms of temperature (solid), altimeter setting (dashed, where available), and wind (full and half barb denote 5 and 2.5 m s^{-1}, respectively) at (a) DPG03, (b) KSLC, (c) KTPH, (d) KELY, (e) LOFUT, (f) VENU1, (g) QLN, (h) KPVU, (i) LAK, and (j) MS6. Cold and warm frontal passages denoted by black and grey vertical lines, respectively. See Fig. 2.1 for station locations.

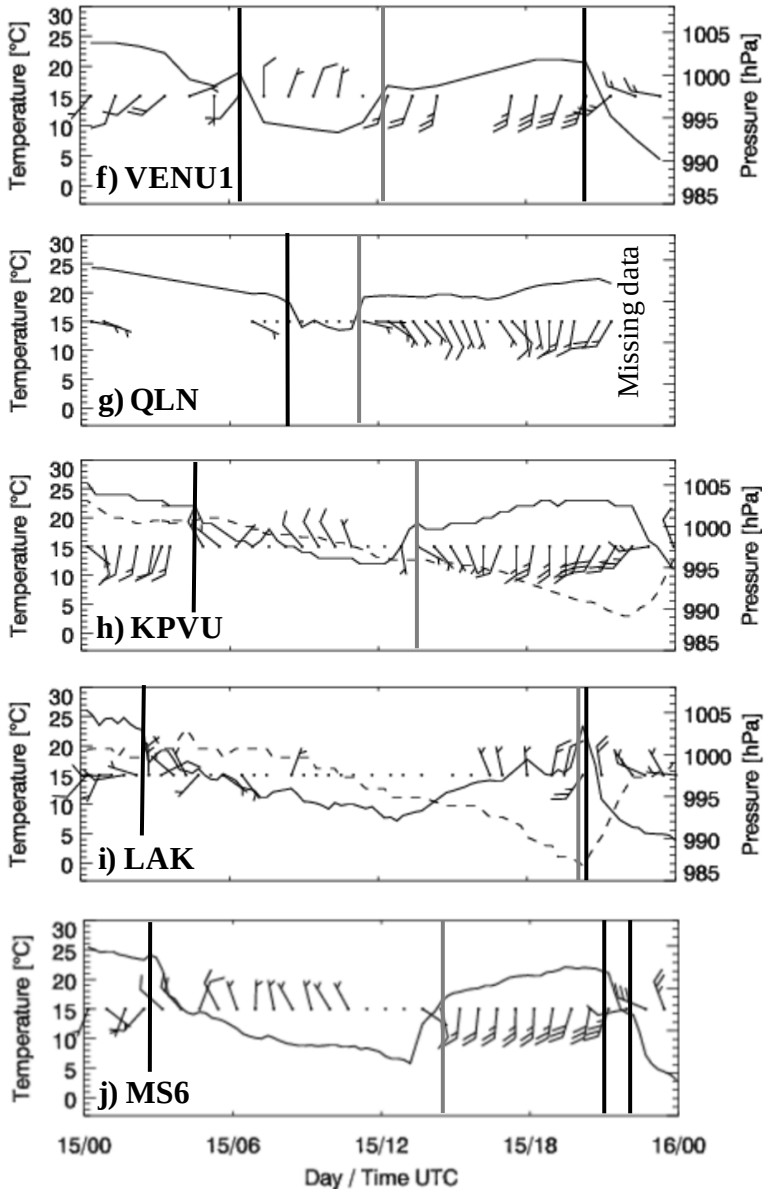

Figure 2.4 continued.

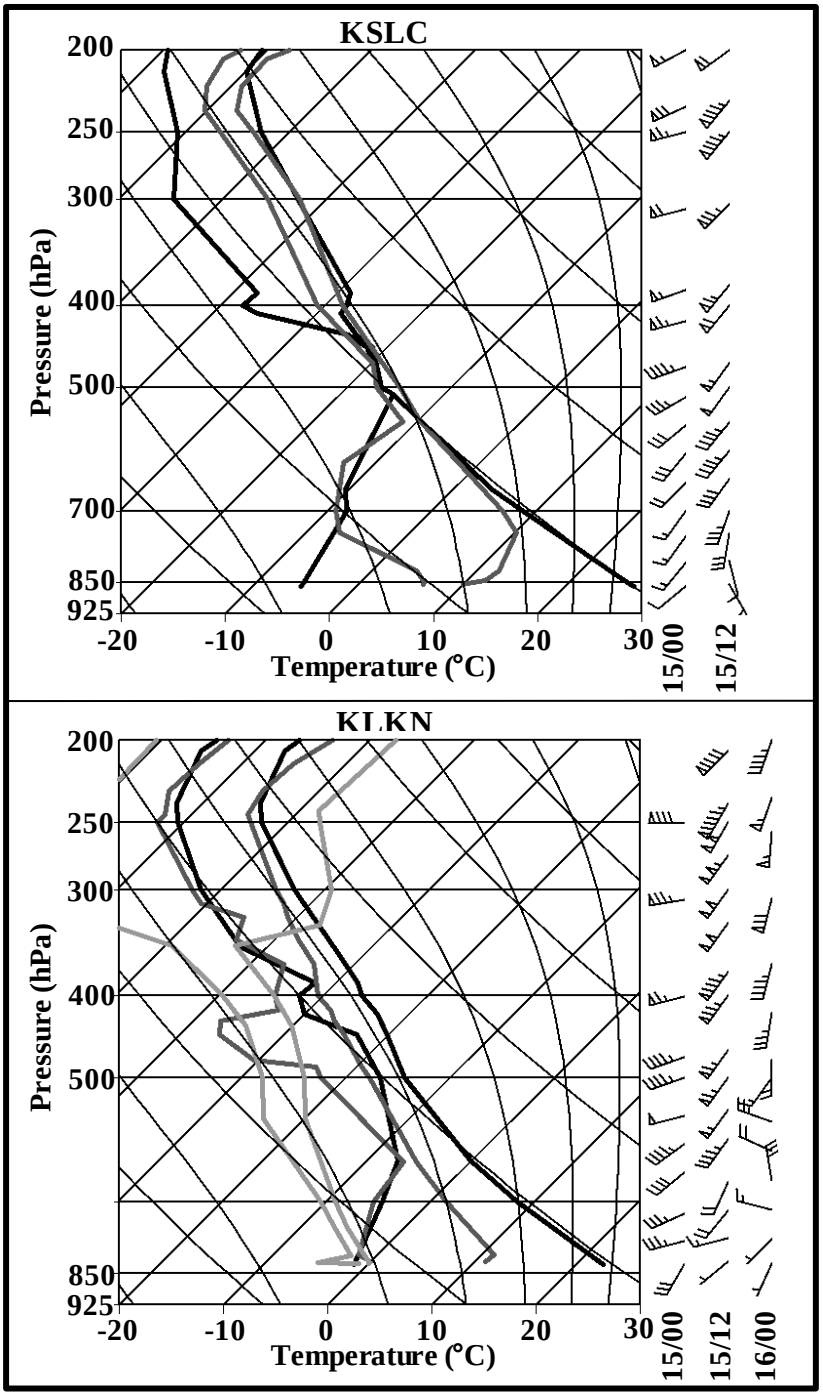

Figure 2.5. Soundings. Skew *T*–log *p* diagrams (temperature and dewpoint) for KSLC and KLKN at 0000 UTC 15 Apr (black), 1200 UTC 15 Apr (medium grey), and 0000 UTC 16 Apr (light grey, KSLC sounding not successfully launched). Vertical wind profiles (pennant, full barb, and half barb denote 25, 5, and 2.5 m s^{-1}, respectively) to right with day/hour (UTC) as indicated.

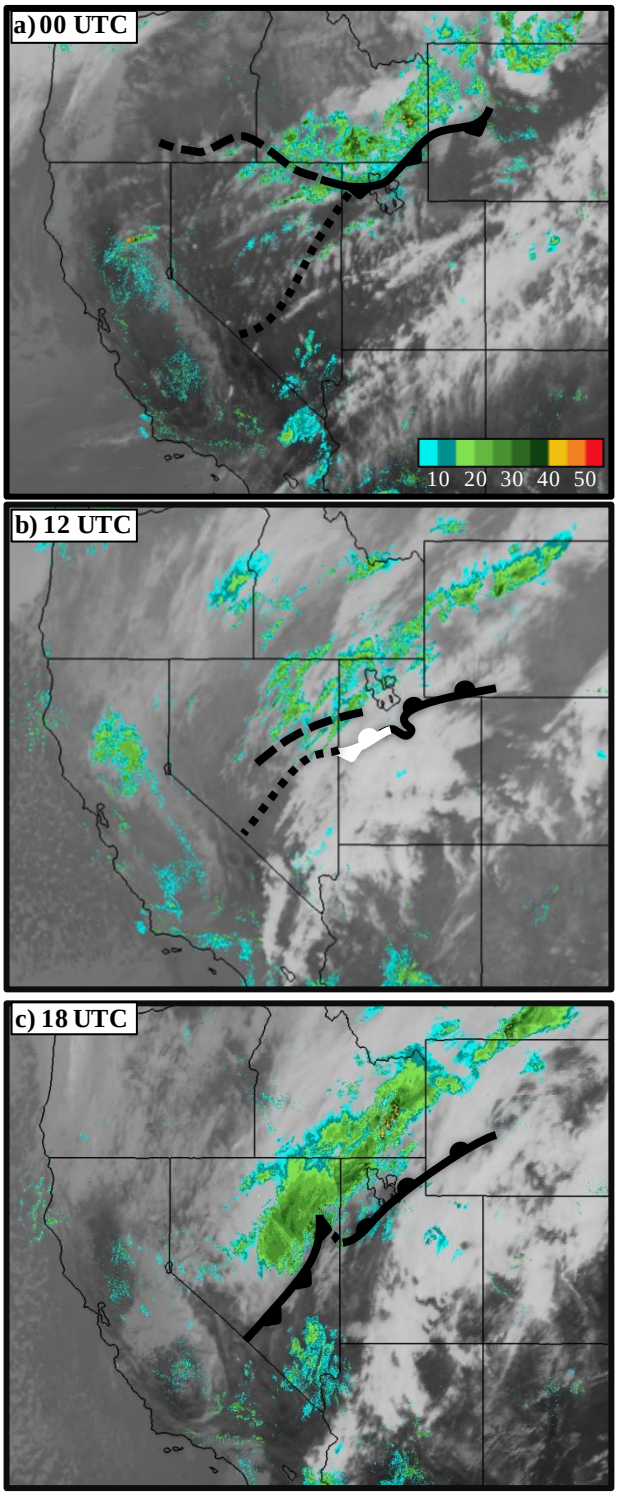

Figure 2.6. Satellite and radar imagery. Infrared satellite and lowest-elevation scan (0.5°) radar reflectivity composite at (a) 0000 UTC, (b) 1200 UTC, and (c) 1800 UTC 15 Apr. Reflectivity scale (dBZ) in lower right of (a). Radar imagery collected 0-10 min after top of hour except at 1153 UTC at KEYX in (b). Radar imagery missing from KMAX and KHDX in (b) and KRTX and KVBX in (c). Manual frontal analyses from Fig. 2.3.

lower tropospheric warm anomaly that extends from the surface to 700 hPa (Figs. 2.2b, c). Despite the wind shift and warm anomaly, there is little evidence of a coherent 1500-m surface trough, although observations are relatively sparse in this region (Fig. 2.3a).

The axes of the upper-level cyclonic PV anomaly and trough move over the Pacific coast by 0600 UTC (Fig. 2.7a).At 700 hPa, the two regions of QG forcing for ascent are now found over the northern California-Nevada border and southeastern Idaho. During this period, the 700-hPa baroclinic zone moves slowly southeastward over Nevada and strengthens as cooler air moves southward over Oregon, California, and northern Nevada (Fig. 2.7b). Concurrently, the 1500-m low center over northern California dissipates and pressures fall over northwest Nevada, but remain steady over northern Utah. A 1500-m low remains over the Mojave Desert, but shifts northwestward as the Mojave cools and crest-level (700 hPa) cross-barrier flow intensifies, leading to pressure falls in the lee of the high Sierra (Figs. 2.3b and 2.7b).

The surface cold front becomes stationary over northern Utah shortly after passing KSLC at ~0200 UTC (Figs. 2.3b and 2.4b), but continues to progress slowly southward over southwest Wyoming (Fig. 2.3b). Concurrently, post-frontal precipitation weakens and becomes more scattered (not shown). To the west, the baroclinic trough moves slowly southward towards the GBCZ, incorporating the intervening baroclinity (Figs. 2.3b and 2.7c). Surface confluence associated with the GBCZ persists over southern and central Nevada, but weakens (cf. Figs. 2.2c and 2.7c), perhaps due to the nocturnal decoupling of surface winds.

The upper-level cyclonic PV anomaly and trough compact and dig through 1200 UTC (Fig. 2.8a) while strong 700-hPa QG forcing for ascent develops over Nevada (Fig.

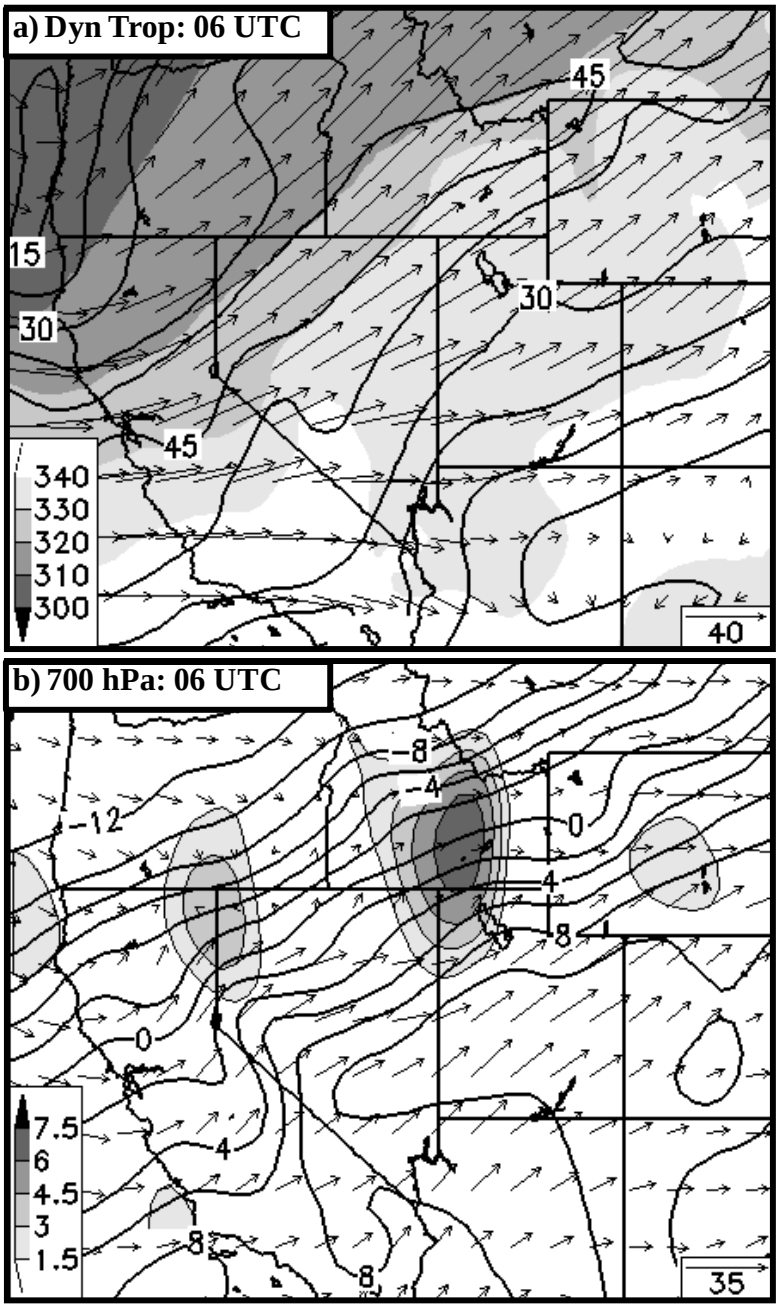

Figure 2.7. Synoptic analyses. (a) RUC2 dynamic tropopause (2 PVU) pressure (hPa, shaded following inset scale), wind vectors (m s^{-1}, following inset scale), and isotachs (contoured every 7.5 m s^{-1}). (b) RUC2 700-hPa temperature (contoured every 2°C), wind vectors (m s^{-1}, following inset scale), and 700-hPa QG forcing for ascent (x10^{-15} K m^{-2} s^{-1}, shaded following inset scale). (c) ADAS surface analysis with terrain height (m, shaded following inset scale), potential temperature (contoured every 2 K), wind vectors (m s^{-1}, following inset scale), and manual frontal analysis at 0600 UTC 15 Apr.

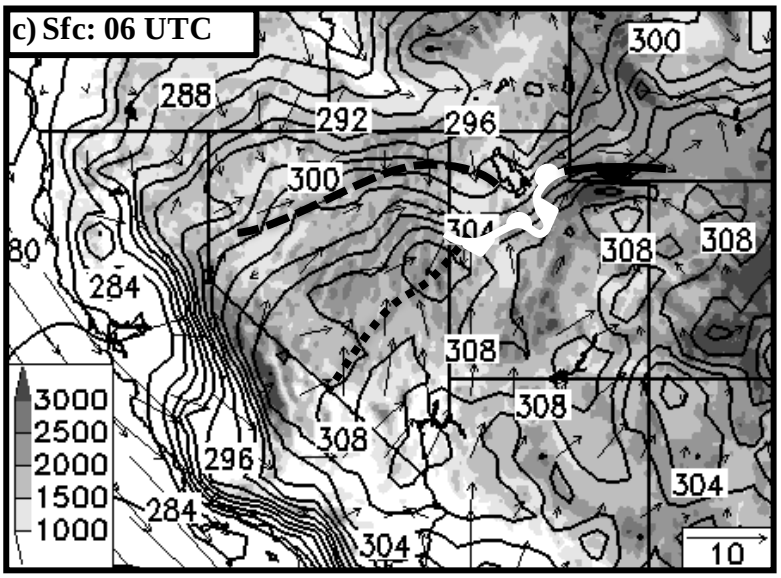

Figure 2.7 continued.

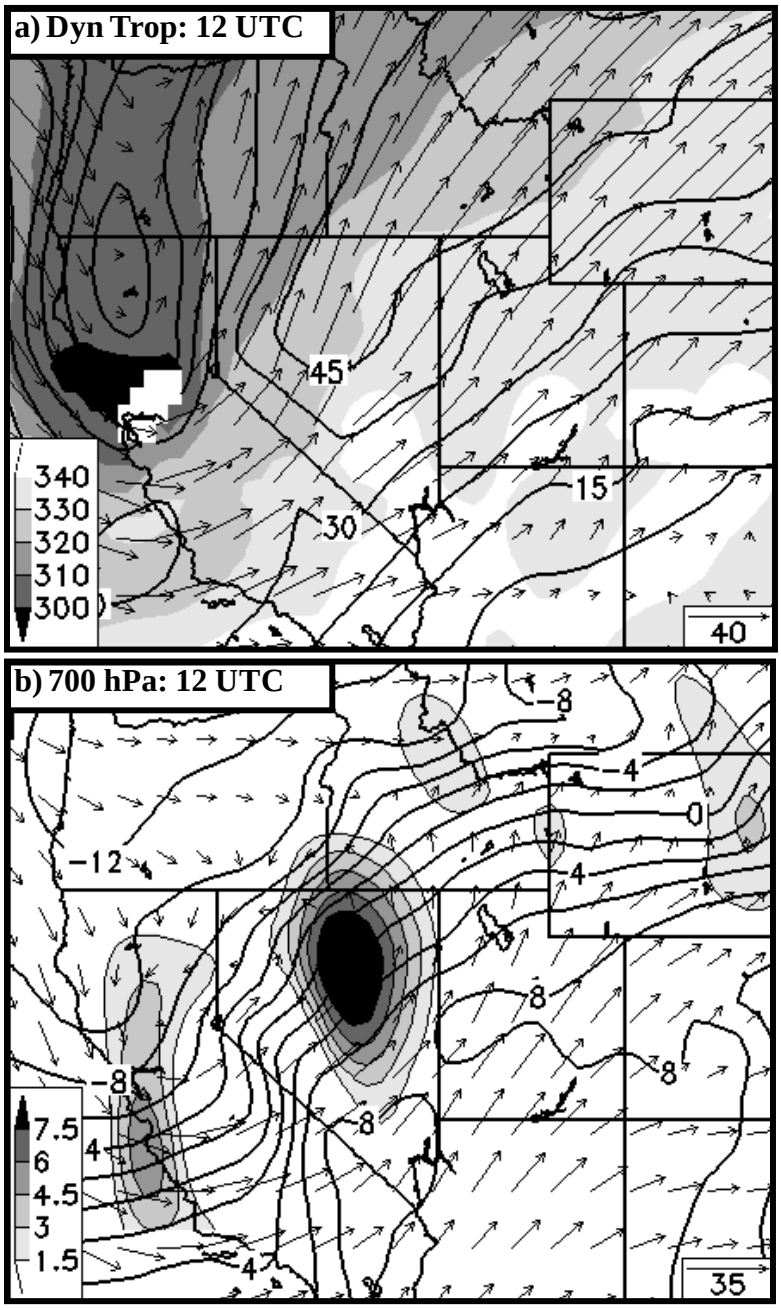

Figure 2.8. Synoptic analyses. (a) RUC2 dynamic tropopause (2 PVU) pressure (hPa, shaded following inset scale), wind vectors (m s^{-1}, following inset scale), and isotachs (contoured every 7.5 m s^{-1}). (b) RUC2 700-hPa temperature (contoured every 2°C), wind vectors (m s^{-1}, following inset scale), and 700-hPa QG forcing for ascent (x10^{-15} K m^{-2} s^{-1}, shaded following inset scale). (c) ADAS surface analysis with terrain height (m, shaded following inset scale), potential temperature (contoured every 2 K), wind vectors (m s^{-1}, following inset scale), and manual frontal analysis at 1200 UTC 15 Apr.

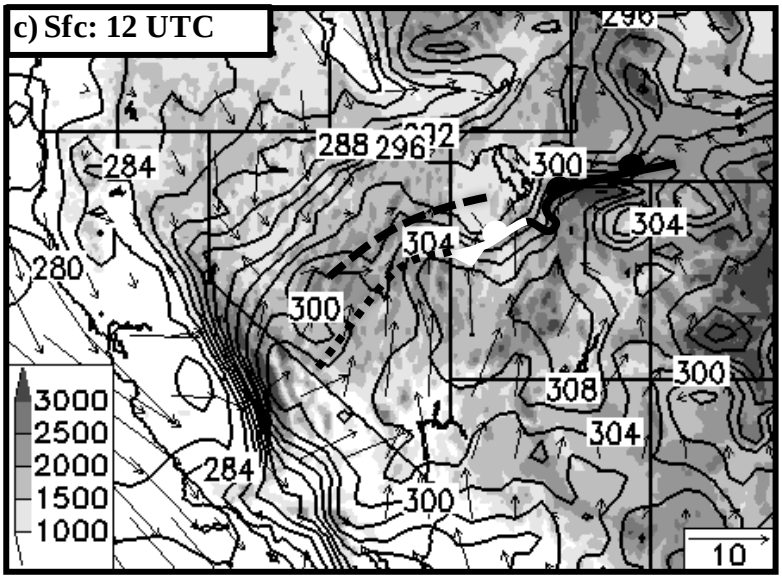

Figure 2.8 continued.

2.8b). As a result, 1500-m pressure falls become increasingly concentrated near and along the GBCZ, which is becoming the locus for cyclogenesis (Fig. 2.3c). As flow across the Sierra Nevada intensifies, the lee trough deepens, shifts northward, and develops a barrier-parallel orientation [similar to, e.g., Steenburgh and Mass (1994) for the Colorado Rockies].

During this period, the 700-hPa thermal wave amplifies (Fig. 2.8b), and, in response, the former surface cold front over northern Utah and southwest Wyoming retreats slowly northward as a warm front (Figs. 2.3c and 2.8c)[2]. Above the surface-based nocturnal inversion, veering winds and a pronounced stable layer are consistent with the development of warm advection within the frontal zone over KSLC (Fig. 2.5). This shallow frontal zone extends upward only to 742 hPa (below the mountain ridges surrounding the Salt Lake Valley). Over northern Nevada, comparison of the 0000 and 1200 UTC KLKN soundings reveals cooling throughout the troposphere, but especially below 600 hPa where temperatures have decreased 6-11°C (Fig. 2.5). At the surface, the baroclinic trough continues to progress southward toward the GBCZ (Figs. 2.3c and 2.8c). In addition, cold advection accompanying the baroclinic trough intensifies as surface winds veer to northerly and strengthen over northwest Nevada. With strong QG forcing for ascent over the region, radar echoes begin to develop above the relatively dry, well-mixed, low-level environment found over northeast Nevada, and a large cirrus shield moves eastward over Utah (Figs. 2.5, 2.6b, and 2.8b).

The upper-level cyclonic PV anomaly and trough take on a negative tilt as they move eastward through 1800 UTC (Fig. 2.9a). At 700 hPa, the area of QG forcing for

[2]The ADAS analysis (Fig. 2.8c) places the surface baroclinic zone too far south at this time compared to that inferred from MesoWest observations in our manual analysis.

ascent becomes more elongated, matching well the orientation of the 1500-m trough and developing cold front (Figs. 2.3d and 2.9b). The 1500-m low center is found along the warm front over the Great Salt Lake Basin (Fig. 2.3d), the lowest, broadest topographic basin along the trough axis. As the GBCZ collects and concentrates baroclinity from the north, including that accompanying the approaching baroclinic trough, a cold front forms over central Nevada and rapidly strengthens as it moves east (Figs. 2.3d and 2.9c). Low-level sublimational and evaporative cooling likely also contribute to frontogenesis and frontal scale collapse, as satellite and radar observations show the development of a solid band of post-frontal clouds and precipitation, in contrast to diurnal surface heating occurring in the cloud-free pre-frontal environment (cf. Figs. 2.6c and 2.9c). Passage of the now rapidly developing cold front is first observed at KTPH at 1545 UTC (Fig. 2.4c), with a substantially stronger passage at KELY at 1750 UTC (Figs. 2.3d, 2.4d, and 2.9c), the latter observing an 11°C $(2\ h)^{-1}$temperature fall. Over Utah and southwest Wyoming the entire frontal boundary progresses slowly northward as a warm front that is not yet structurally continuous with the cold front over Nevada (Fig. 2.3d).

As the upper-level cyclonic PV anomaly and trough advance eastward (not shown), the 1500-m low center reaches its minimum central pressure of 824 hPa at KSLC at 2100 UTC (Fig. 2.3e), and the corresponding 982-hPa reduced sea level pressure becomes the second lowest ever reported in Utah. By this time the entire frontal boundary, including the former warm front, reaches its maximum intensity and progresses southward and eastward as a cold front. The accompanying 17°C $(2h^{-1})$ temperature fall at KSLC (Fig. 2.4b) is the largest in the 25-y Salt Lake City cold front climatology developed by SS08. At the University of Utah, 12 km east of KSLC, a

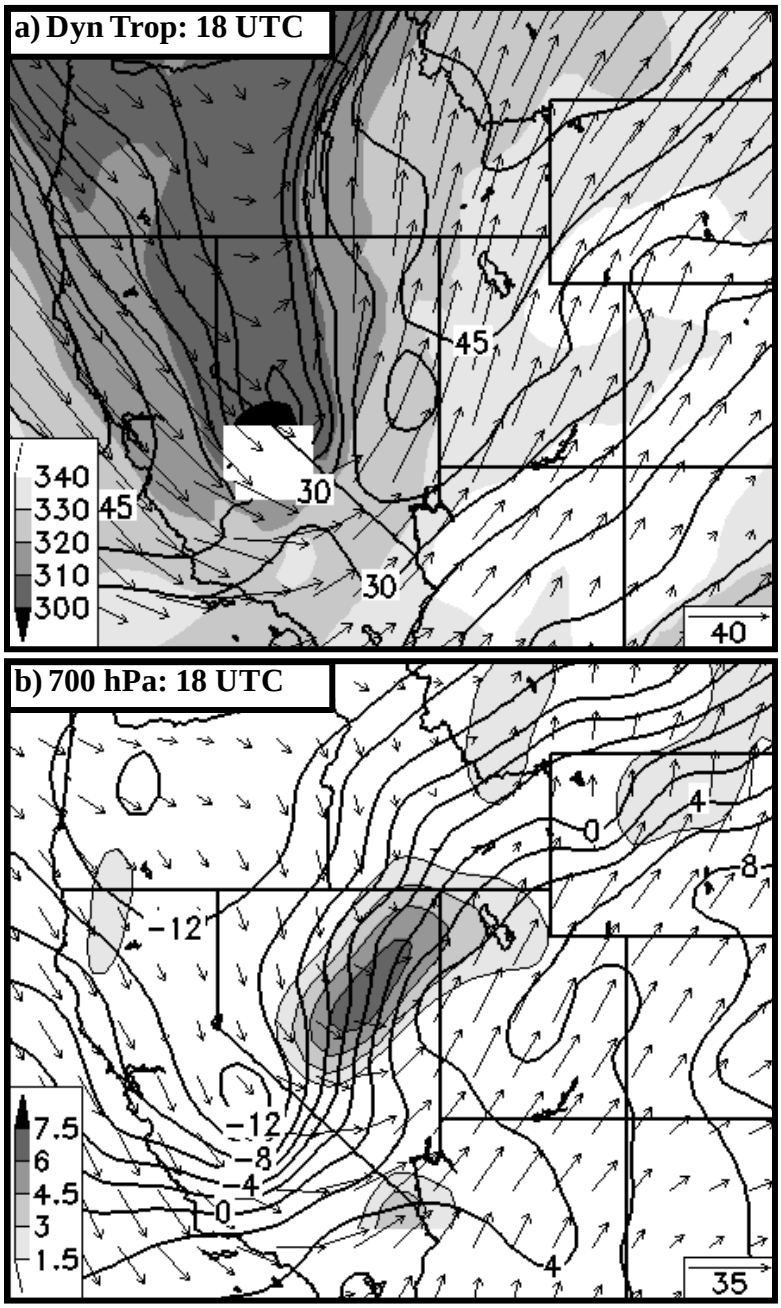

Figure 2.9. Synoptic analyses. (a) RUC2 dynamic tropopause (2 PVU) pressure (hPa, shaded following inset scale), wind vectors (m s^{-1}, following inset scale), and isotachs (contoured every 7.5 m s^{-1}). (b) RUC2 700-hPa temperature (contoured every 2°C), wind vectors (m s^{-1}, following inset scale), and 700-hPa QG forcing for ascent (x10^{-15} K m^{-2} s^{-1}, shaded following inset scale). (c) ADAS surface analysis with terrain height (m, shaded following inset scale), potential temperature (contoured every 2 K), wind vectors (m s^{-1}, following inset scale), and manual frontal analysis at 1800 UTC 15 Apr.

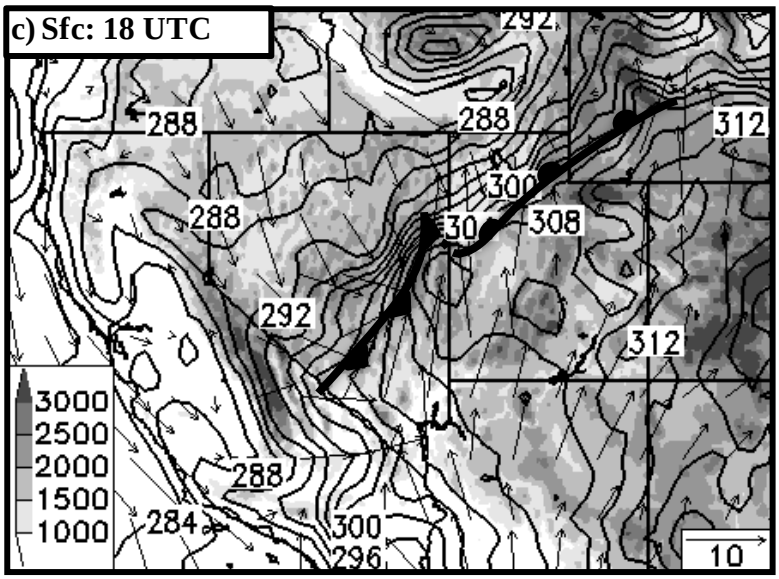

Figure 2.9 continued.

meteorology student observes a 7°C (10 s)$^{-1}$drop with frontal passage using a handheld instrument. Many lowland stations in northern Utah report peak gusts in excess of 25 m s^{-1} in the pre- and postfrontal environments, with substantially stronger gusts at some stations (e.g., KU24, 32 m s^{-1}; KU42, 35 m s^{-1}; PEM, 47 m s^{-1}). Satellite imagery derived from the Advanced Very High Resolution Radiometer aboard the NOAA-16 polar orbiting satellite at 2046 UTC reveals widespread blowing dust across much of the Mojave Desert and southern Nevada (Fig. 2.10). During this period, KLAS reports 20-25 m s^{-1} wind gusts and $\leq$ 400 m visibility under otherwise clear skies. Blowing dust over Utah, evident between the cloud streets within the dry slot, forces the closure of Interstate 15 and leaves a brown layer of dust on the snowpack of the Wasatch Mountains and other ranges. Therefore, we hypothesize that high winds associated with Intermountain cyclones contribute to episodic dust deposition onto the mountain snowpack of the region, decreasing albedo, and as discussed by Painter et al. (2007), leading to an earlier melt out of this important natural water resource.

Kinematic Frontogenesis Diagnostics

The analysis above suggests that the cold front accompanying the Tax Day Storm forms as confluent deformation and convergence along the GBCZ, which is initially non-frontal, collect and concentrate baroclinity from the northern Great Basin. It is along this incipient frontal zone that the 1500-m cyclone forms, implying that the GBCZ plays a central role in both frontogenesis and cyclogenesis. In this section we further investigate the GBCZ.

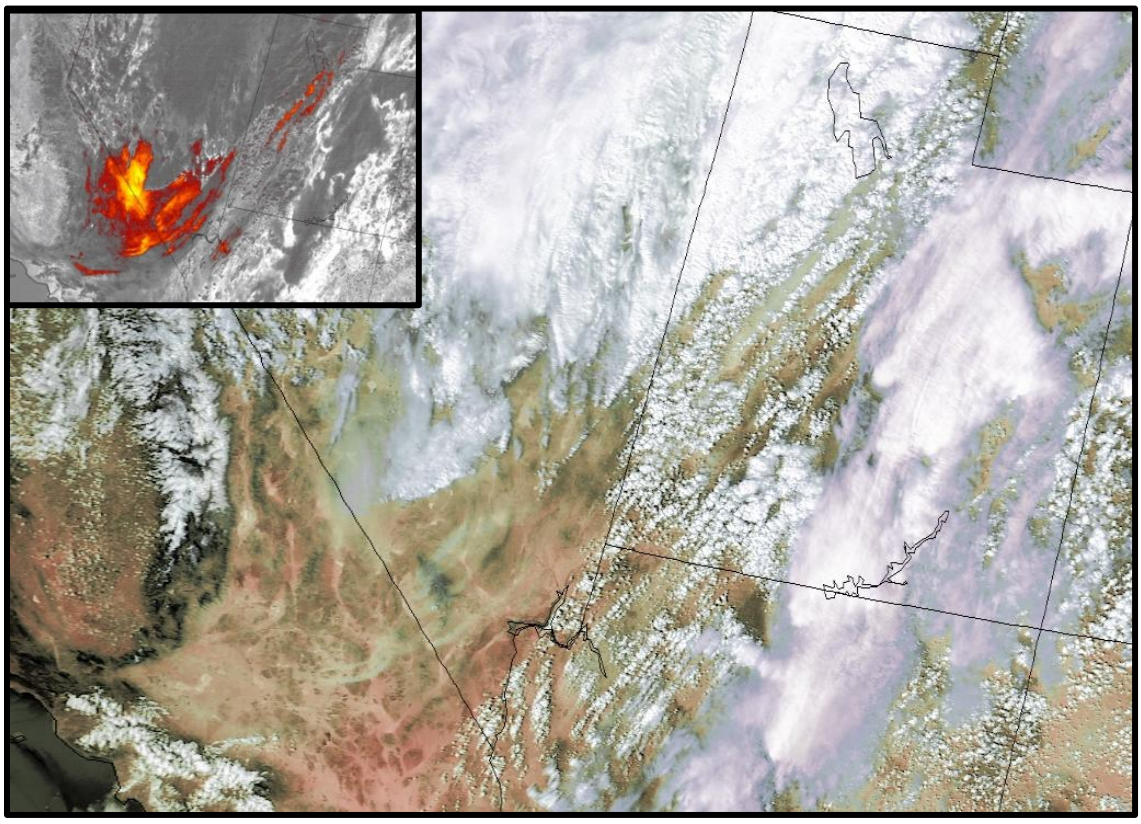

Figure 2.10. AVHRR imagery. False-color 0.63-μm reflectance from the Advanced Very High Resolution Radiometer aboard the NOAA-16 polar-orbiting satellite at 2046 UTC 15 Apr. Inset: Channel 4-5 (11-12 μm) brightness temperature difference, with large differences typically associated with volcanic or dust aerosols colored (see Iino et al. 2004 for methodology).

Cohen and Kreitzberg (1997) identify and quantify the strength of airstream boundaries using the *average contraction rate*, which represents the time-averaged rate of change of the relative distance between two air parcels. Since the calculation of the average contraction rate requires a large number of trajectories, Cohen and Schultz (2005) present a kinematic framework for identifying airstream boundaries based on the *instantaneous contraction rate, C* (hereafter *contraction*), defined as

$$C = \frac{E-D}{2}, \tag{3}$$

where

$$E = \left[\left(\frac{\partial u}{\partial x} - \frac{\partial v}{\partial y}\right)^2 + \left(\frac{\partial u}{\partial y} + \frac{\partial v}{\partial x}\right)^2\right]^{1/2} \tag{4}$$

is resultant deformation,

$$D = \frac{du}{dx} + \frac{dv}{dy} \tag{5}$$

is divergence, and derivatives are calculated from the two-dimensional ADAS surface analysis. For any point in the flow, contraction represents the maximum instantaneous rate at which two parcels are approaching each other, which occurs along the axis of contraction and normal to the axis of dilatation.

Kinematic frontogenesis can be evaluated using a form of the Petterssen (1936, 1956) frontogenesis function:

$$F = \frac{1}{2}|\nabla\theta|(Ecos2\beta - D)\,, \tag{6}$$

where θ is the potential temperature, the gradient operator is two dimensional and evaluated from the ADAS surface analysis, and β is the angle between the isentropes and the axis of dilatation. Kinematic frontogenesis is inclusive of the potential temperature

gradient, and the magnitude and sign of the deformation term ($Ecos2\beta$) depend on the orientation of the isentropes with respect to the axis of dilatation. Contraction only diagnoses the strength of an airstream boundary (Cohen and Schultz 2005). In the presence of a potential temperature gradient, frontogenesis produced by the deformation term is maximized when the isentropes are parallel to the axis of dilatation.

In the Tax Day Storm, the GBCZ is a persistent, quasi-stationary airstream boundary that develops by 1800 UTC 14 Apr (not shown). At 0000 UTC 15 Apr, contraction associated with the GBCZ extends downstream from the high Sierra into northern Utah (Fig. 2.11a). This pattern persists through 1200 UTC when surface winds are weaker (Figs. 2.3c and 2.8c) and contraction associated with the GBCZ is less coherent, but still visible (Fig. 2.11b). At this time, weak kinematic frontogenesis is found over west-central Utah where baroclinity associated with the cold front that sagged southward through northern Utah at 0000 UTC (Fig. 2.11a) merges with the GBCZ (Fig. 2.11b). By 1500 UTC, the GBCZ is drawing baroclinity over northern and central Nevada into an increasingly favorable frontogenetical environment (Fig. 2.11c). In particular, isentropes in this region are oriented nearly parallel to the axes of dilatation along the GBCZ.

The contraction maximum associated with the GBCZ becomes more meridionally oriented over Nevada between 1500 and 1700 UTC, but remains quasi-stationary over northern Utah (cf. Figs. 2.11c, d). Since the GBCZ appears tied to the high Sierra, its orientation appears to be a response to the backing of the ambient crest-level flow as the wave amplifies. By 1700 UTC, the baroclinic zone is collocated with the contraction

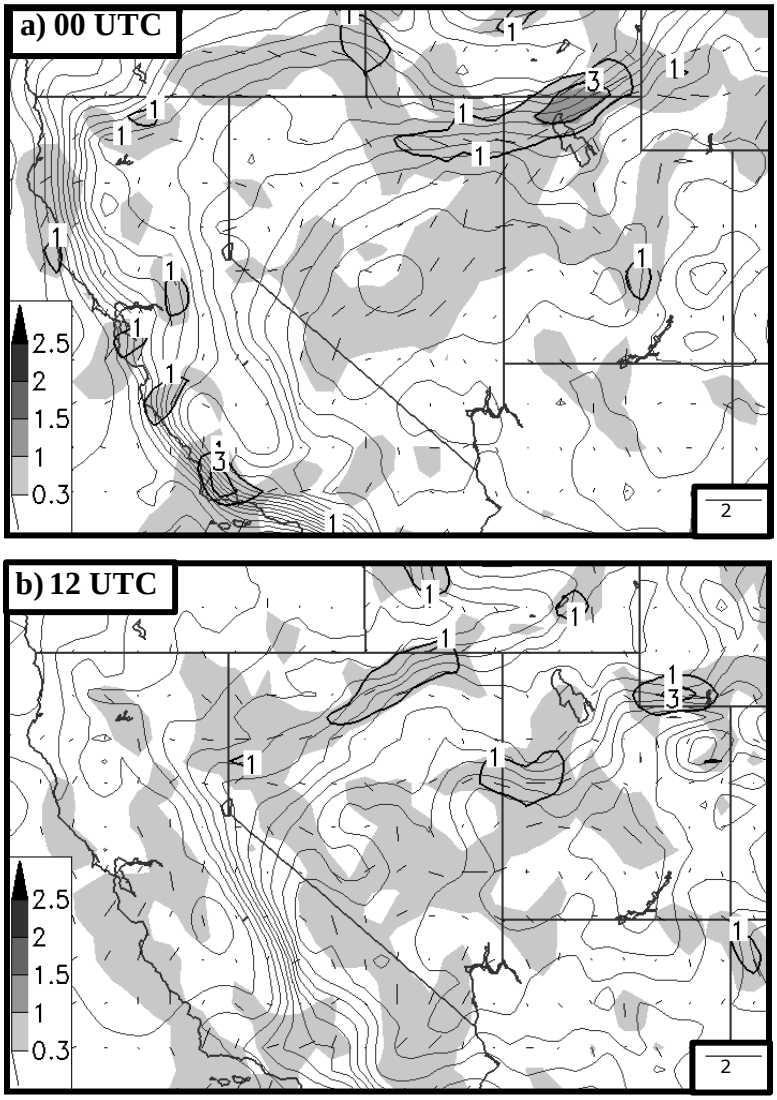

Figure 2.11. Frontogenesis diagnostics. ADAS contraction ($x10^{-4}$ s^{-1}, shaded according to inset scale), kinematic frontogenesis (black contours every 3 K $(100\ km)^{-1}$ h^{-1}), local orientation of axes of dilatation scaled by magnitude of contraction ($x10^{-4}$ s^{-1}, according to inset scale), and potential temperature (gray contours every 2 K) at (a) 0000 UTC, (b) 1200 UTC, (c) 1500 UTC, (d) 1700 UTC, (e) 1800 UTC, and (f) 2100 UTC 15 Apr.

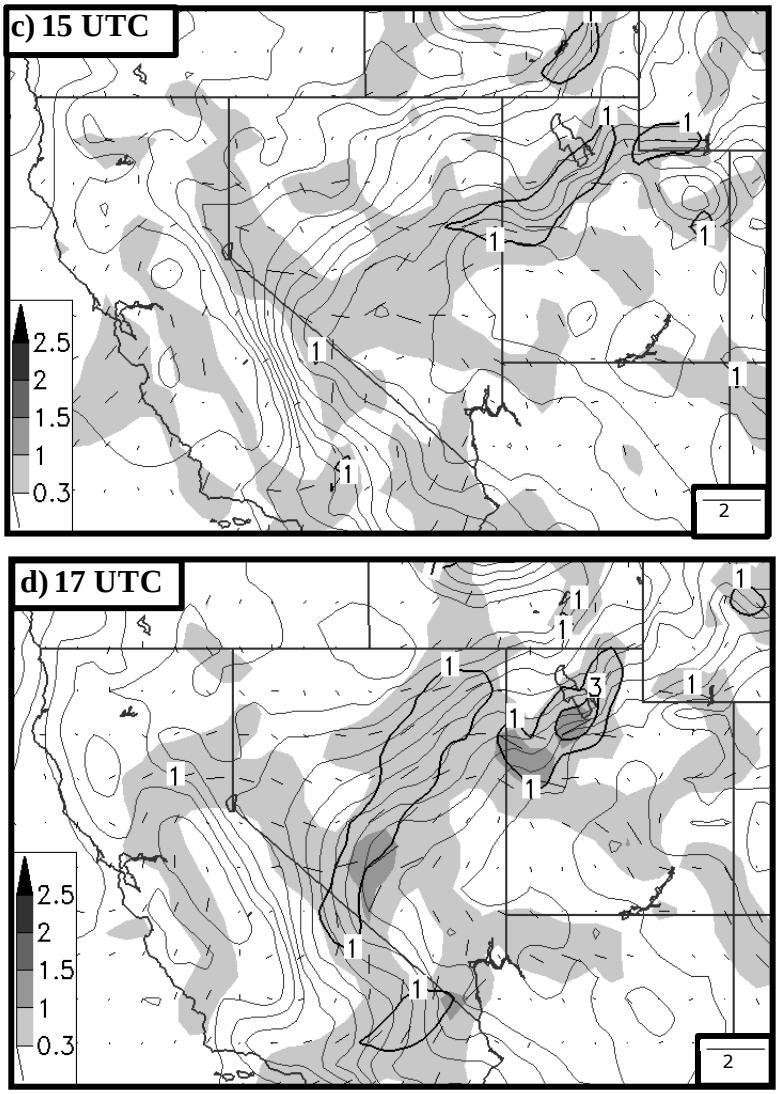

Figure 2.11 continued.

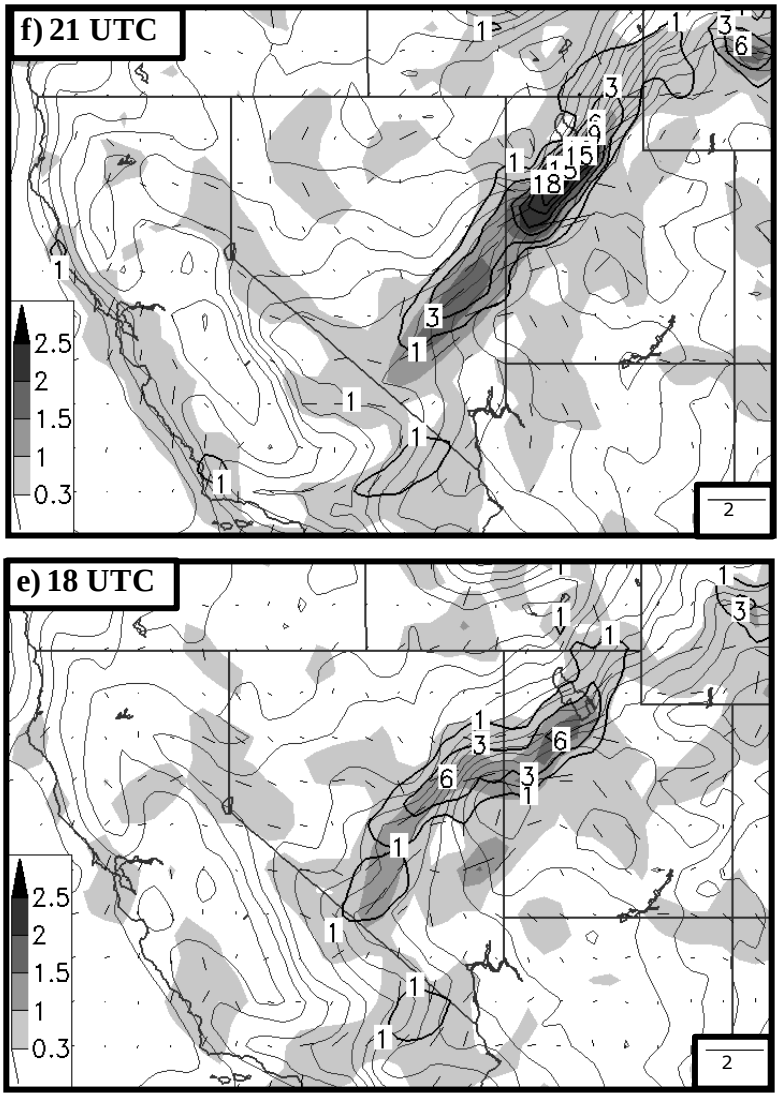

Figure 2.11 continued.

maxima, the isentropes are aligned along the axes of dilatation, and the resulting kinematic frontogenesis is maximized along the incipient cold front over Nevada and the existing front over northern Utah. These two kinematic frontogenesis maxima are distinct, which likely leads to the lack of structural continuity between the warm and cold fronts observed at 1800 UTC (Fig. 2.3d).

Kinematic frontogenesis along the GBCZ intensifies rapidly from 1700-1800 UTC (cf. Figs. 2.11d, e) as maximum baroclinity doubles from ~15 K (100 km)$^{-1}$ to ~30 K (100 km)$^{-1}$ (not explicitly shown) and kinematic frontogenesis more than triples. Several interrelated processes likely contribute to this apparent frontal scale collapse. The first is an increase in surface winds and associated kinematic frontogenesis as the stable nocturnal boundary layer erodes and the pressure trough deepens. The second is geostrophic adjustment, which, has been shown to enhance the cross-front secondary circulation in developing fronts (Hoskins and Bretherton (1972) and Eliassen (1990). Finally, cross-front diabatic heating and cooling contrasts may also contribute, as discussed in the next section and discussed by Koch et al. (1995, 1997), Gallus and Segal (1999), and Segal et al. (2004).

By 2100 UTC contraction, baroclinity, and kinematic frontogenesis reach their peak intensity (Fig. 2.11f). The 7°C (10 s)$^{-1}$ drop accompanying frontal passage at the University of Utah, combined with a frontal speed of 5.6 m s^{-1}, yields a localized temperature gradient of 12.5 K (100 m)$^{-1}$, somewhat stronger than the 6 K (100 m)$^{-1}$ reported for another Intermountain cold front by Schultz and Trapp (2003).

Averaging contraction and axes of dilatation from 2100 UTC 14 Apr – 2100 UTC 15 Apr illustrates the cumulative effect of the quasi-stationary GBCZ (Fig. 2.12a).

Contraction associated with the GBCZ initiates frontogenesis as it collects the baroclinity from the northern Great Basin. This is well illustrated by a time series of average baroclinity, contraction rate, and kinematic frontogenesis in the region surrounding the GBCZ (Fig. 2.12b). Kinematic frontogenesis first increases as the initial cold front pushes into northern Utah at ~0000 UTC, and contraction reaches a maximum with the stronger surface winds in the late afternoon. Overnight, contraction decreases, but mean baroclinity slowly increases in response to weak kinematic frontogenesis. From 1500–2100 UTC contraction and baroclinity increase nonlinearly as the GBCZ collects and concentrates baroclinity, kinematic frontogenesis intensifies, and frontal scale collapse occurs. Kinematic frontogenesis increases most dramatically, being proportional to the product of baroclinity and contraction. Differential diabatic processes likely also contribute to the frontal development, as discussed in the next section.

Trajectories and Diabatic Processes

As suggested previously, diabatic processes appear to contribute to frontogenesis directly through cross-front contrasts in sensible heating and post-frontal sublimational and evaporative cooling (see Fig. 2.6c). They may also contribute indirectly by inducing a thermally forced, cross-front circulation that can nonlinearly enhance frontal scale collapse (e.g., Koch et al. 1995, 1997; Gallus and Segal 1999; Segal et al. 2004). Although it is not possible to fully quantify the direct and indirect effects of differential diabatic heating due to the complex nonlinear feedbacks involved (e.g., Koch et al. 1995), changes in potential temperature along two-dimensional ADAS surface trajectories provide an estimate of direct diabatic contributions to frontogenesis and the potential for enhanced frontal scale collapse.

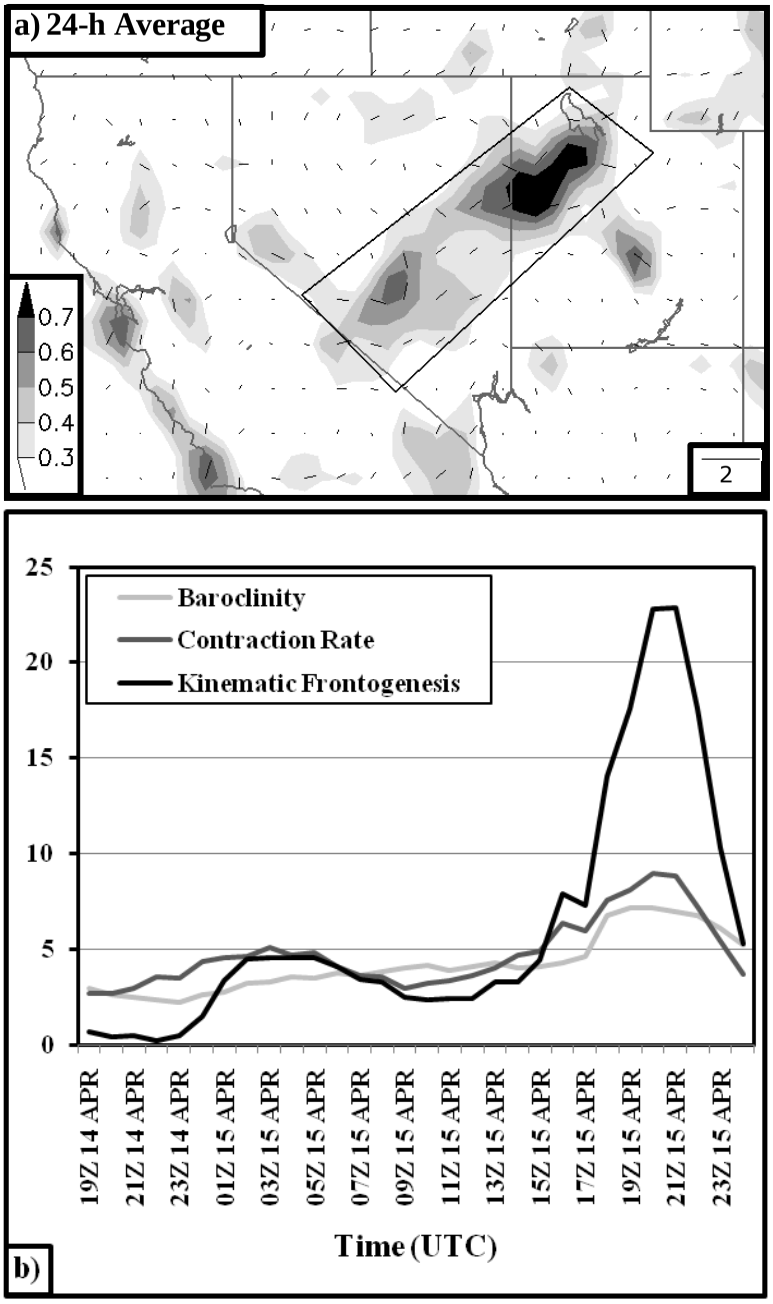

Figure 2.12. Averaged diagnostic fields. (a) Temporally-averaged contraction ($x10^{-4}$ s^{-1}, shaded according to inset scale,) and local orientation of axes of dilatation scaled by magnitude of contraction ($x10^{-4}$ s^{-1}, according to inset scale) from 2100 UTC 14 Apr – 2100 UTC 15 Apr. (b) Areally-averaged contraction ($x10^{-4}$ s^{-1}), baroclinity (K $(100\ km)^{-1}$), and kinematic frontogenesis ($x10^{-1}$ K $(100\ km)^{-1}$ h^{-1}) within the quadrilateral denoted in (a).

Backward 9-h trajectories that begin at 1200 UTC (just prior to sunrise) and terminate on the warm and cold sides of the frontal zone at 2100 UTC (mid afternoon, time of maximum frontal strength) are shown in Fig. 2.13, with beginning, ending, and net change in potential temperature for the trajectories presented in Table 2.1. Potential temperature increases along all prefrontal trajectories. Trajectories 4-11 and 13-14, which originate over the lower Colorado River Valley and south end of the high Sierra, respectively (Figs. 2.8c and 2.9c), experience the largest increases (3-8 K).

In contrast, there is a net decrease or little change in potential temperature along most of the postfrontal trajectories. Trajectories 15-17 begin over the Snake River Plain and experience limited sensible heating and a period of precipitation as they move into northern Utah (Fig. 2.13 and Table 2.1), yielding a net increase in potential temperature of <1 K. In contrast, trajectories 18-23 begin with a higher potential temperature, but are consistently beneath the cloud and precipitation shield that develops after 1200 UTC (Fig. 2.6c). As a result, the potential temperature along these trajectories decreases 3-7 K. Further west, trajectories 24-28 are located near or west of the post-frontal precipitation band (Fig. 2.6c). Trajectories 24 and 25 experience little change, whereas trajectories 26-28 increase 1-4 K.

Collectively, these trajectories illustrate that differential diabatic heating/cooling makes a substantial direct contribution to frontogenesis along much of the front. Most trajectories in the prefrontal airmass undergo several Kelvin of diabatic warming from 1200–2100 UTC, whereas postfrontal trajectories beneath the postfrontal precipitation band experience diabatic cooling or little potential temperature change, particularly those terminating over eastern Nevada and western Utah where they remain under the cloud

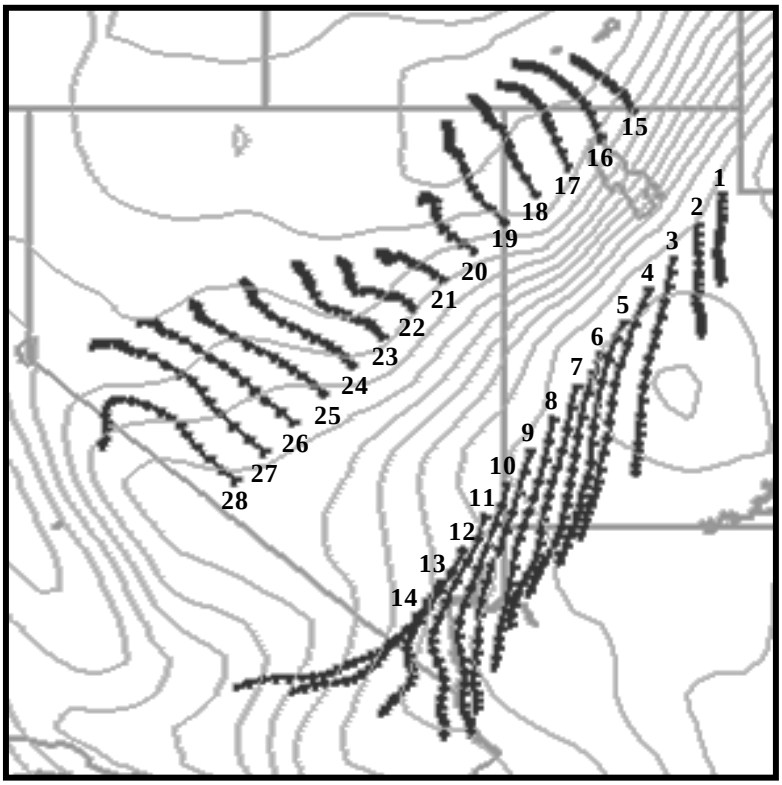

Figure 2.13. Trajectory plot. Nine-hour backward trajectories (1200-2100 UTC 15 Apr, number indicates position at 2100 UTC) terminating on the warm and cold side of the baroclinic zone. Potential temperature at 2100 UTC contoured every 2 K.

Table 2.1. The 1200 UTC, 2100 UTC, and net change in potential temperature (K) along trajectories displayed in Fig. 13.

Trajectory #	1200 UTC	2100 UTC	Change
1	306.1	308.6	2.5
2	308.6	308.9	0.3
3	306.0	308.9	2.9
4	306.1	309.6	3.5
5	305.9	309.9	4.0
6	304.9	310.3	5.5
7	304.6	309.3	4.7
8	304.6	308.3	3.7
9	302.9	308.9	6.0
10	300.4	308.6	8.2
11	302.1	306.0	4.0
12	302.6	304.8	2.1
13	300.7	304.1	3.4
14	295.0	302.6	7.6
15	290.8	291.6	0.8
16	289.2	289.9	0.7
17	288.9	289.3	0.4
18	291.2	288.1	-3.1
19	295.7	288.4	-7.2
20	297.4	292.3	-5.1
21	299.0	293.2	-5.8
22	298.7	293.3	-5.4
23	298.4	293.5	-5.0
24	296.0	295.6	-0.4
25	296.0	296.2	0.2
26	294.1	297.6	3.5
27	294.5	297.6	3.0
28	297.5	298.7	1.2

band experience diabatic cooling or little potential temperature change, particularly those terminating over eastern Nevada and western Utah where they remain under the cloud and precipitation shield for a sustained period of time. The estimated direct differential diabatic contribution to frontogenesis during this 9-h period ranges from ~1 K $(100\ km)^{-1}$ along the southwest end of the front, to ~5 K $(100\ km)^{-1}$(~40% of cross-front baroclinity) along the central part, to ~0 K $(100\ km)^{-1}$ at the northeast end.

Front-Mountain Interactions Over Northern Utah

We now focus on the smaller-scale front-mountain interactions observed over the basin-and-range topography of northern Utah during this event. The surface cold front moves southward into northern Utah at approximately 0000 UTC (Fig. 2.3a) and by 0400 UTC extends across the basins and valleys south and west of the Great Salt Lake (Fig. 2.14a)[3]. The front briefly passes south of LOFUT in the southern Rush Valley at 0515 UTC (Fig. 2.4e) before retreating just north of LOFUT at 0545 UTC, where it remains stationary through ~1200 UTC.

As the thermal wave begins to amplify at ~1200 UTC, the frontal zone begins a complex northward progression as a warm front. Starting with VENU1 at 1225 UTC (Fig. 2.4f), the warm front moves continuously northward through the Rush Valley (Figs. 2.14b, c). In contrast, frontal movement over Utah Valley to the east is not continuous. Stations along the valley floor observe abrupt warming at irregular times over a 2.5-h period as the shallow cold airmass is turbulently eroded by increasing southerly and southwesterly flow aloft (1200 UTC KSLC sounding, Fig. 2.5). For example, QLN (Fig.

[3]Given the shallowness of the post-frontal airmass, and for ease of presentation, surface fronts are only analyzed over basin and valley regions.

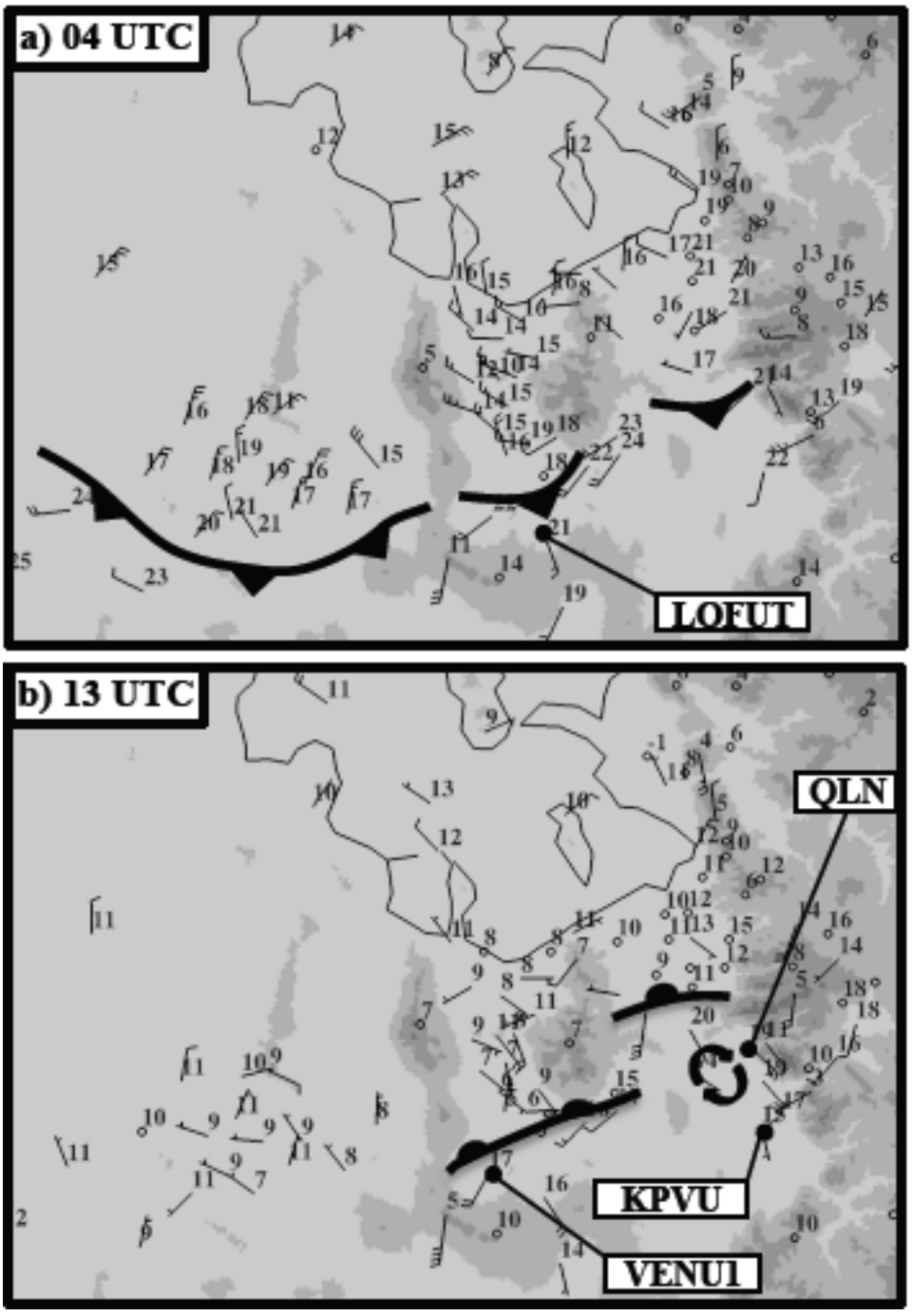

Figure 2.14. Manual analyses for northern Utah. Surface frontal analyses at (a) 0400, (b) 1300, (c) 1500, (d) 1800, (e) 2100, and (f) 2200 UTC 15 Apr. Station models as in Fig. 2.3.

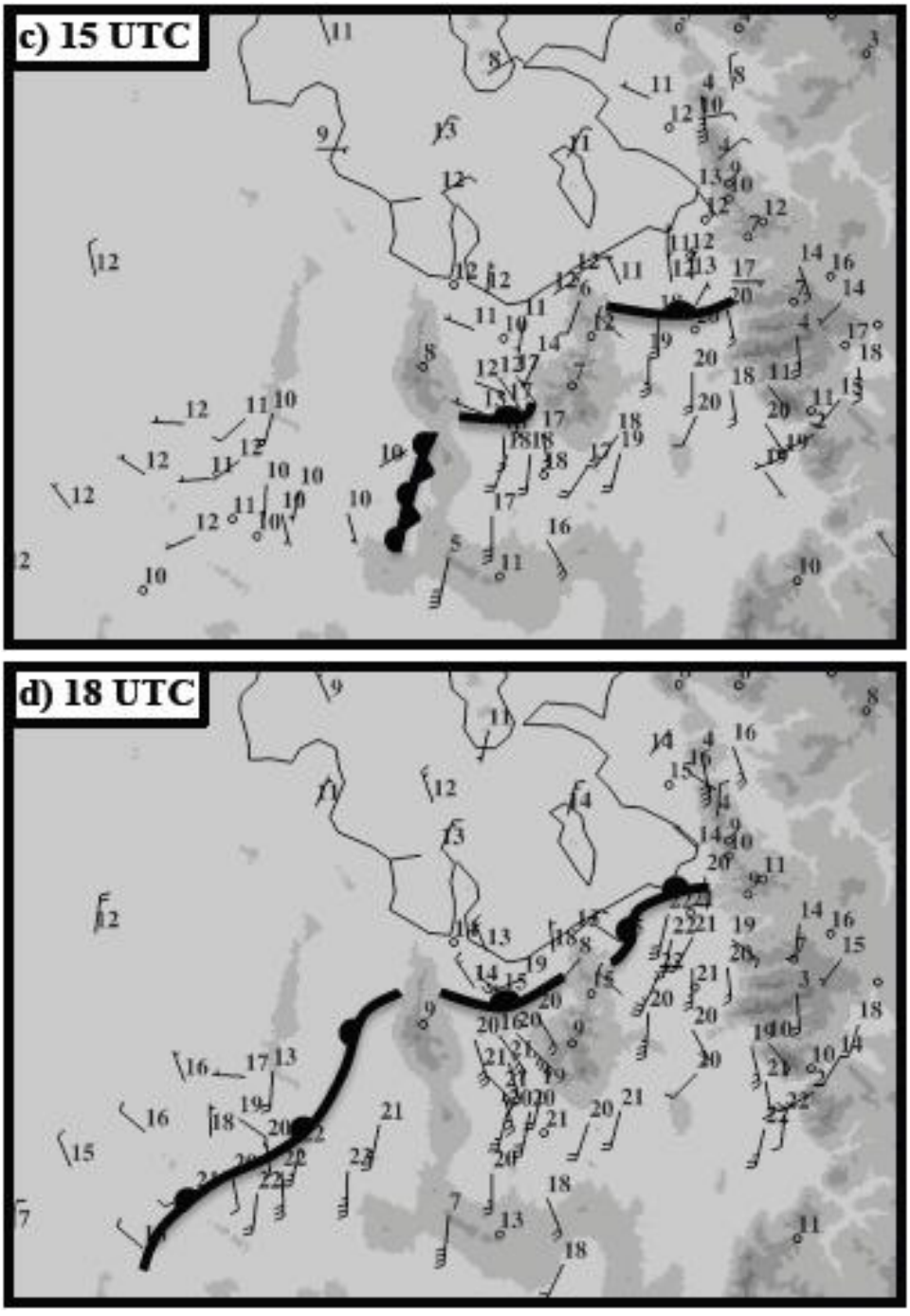

Figure 2.14 continued.

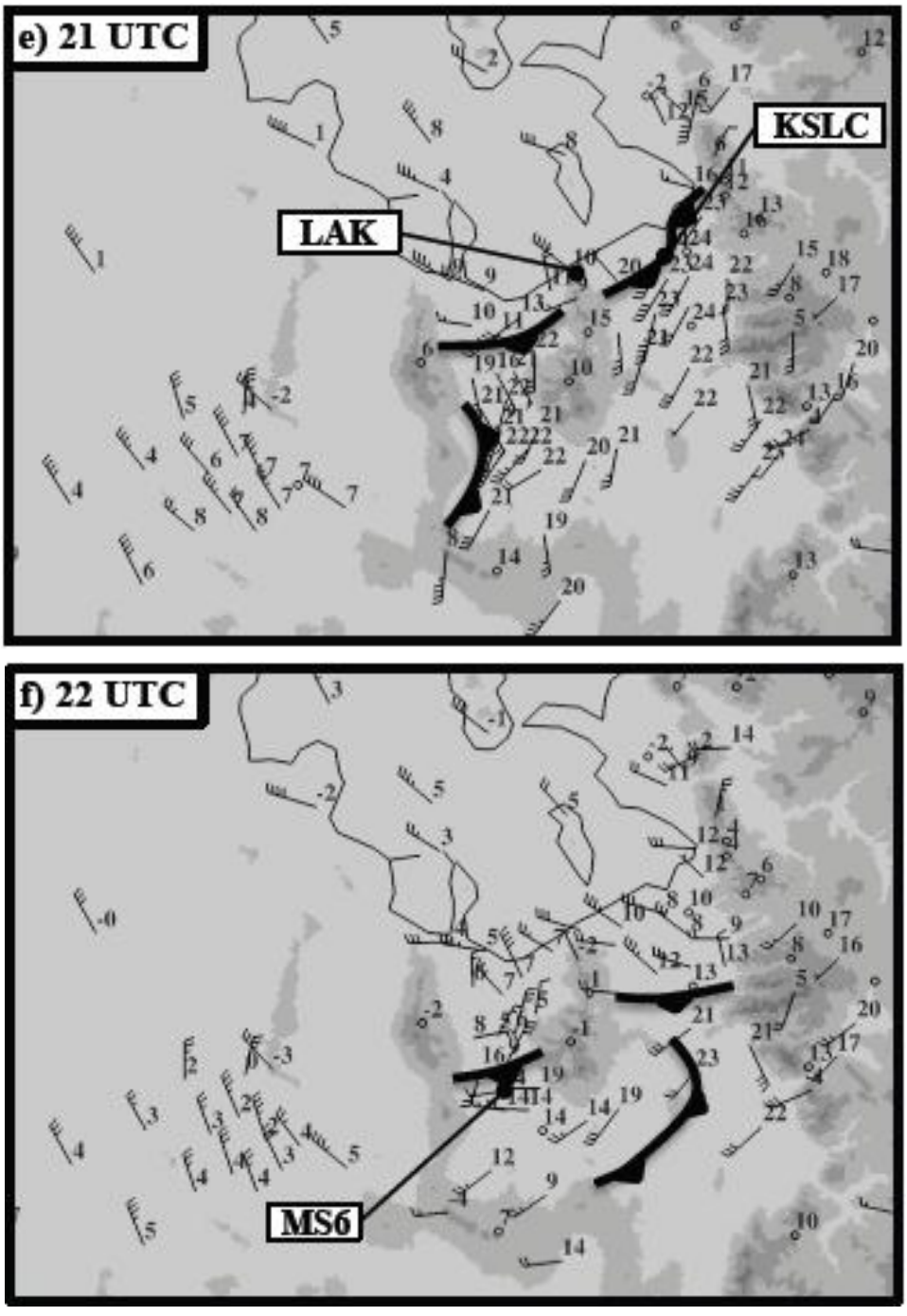

Figure 2.14 continued.

2.4g, 1451 m) warms at 1125 UTC, whereas KPVU (Fig. 2.4h, 1371 m), 13 km to the south, does not warm until 1335 UTC.

The warm front moves continuously northward through the Salt Lake and Tooele Valleys, but further west remains stationary through 1500 UTC near the Onaqui Mountains (Fig. 2.14c). By 1800 UTC the entire frontal boundary is progressing northward and westward as a warm front that stretches from the Great Salt Lake Desert eastward across the northern ends of the Tooele and Salt Lake Valleys (Fig. 2.14d). This progression continues until ~2015 UTC when the 1500-m low center moves through the region, and by 2100 UTC the entire front moves southward and eastward as a cold front (Fig. 2.3e). Along the south shore of the Great Salt Lake, abrupt warming occurs as the warm front approaches LAK from the south, followed immediately by abrupt cooling as the front reverses direction (Fig. 2.4i). At KSLC the passages of both a warm (1755 UTC) and cold front (2055 UTC) are apparent (Fig. 2.4b).

As the cold front moves south and east, the movement of the low center along the frontal boundary and the influence of the local basin-and-range terrain results in the western segment of the cold front moving rapidly eastward while the middle and eastern segments move slowly southward (cf. Figs. 2.14d, e). As a result, over the Rush Valley and portions of Utah Valley, a cold-frontal segment passes first from the west, followed by a second cold-frontal segment from the north (cf. Figs. 2.14e, f).

The meteogram from MS6 in the Rush Valley summarizes the entire event well, including the passage of the two frontal segments (Fig. 2.4j). The antecedent cold front moves southward through northern Utah, passing MS6 at 0310 UTC, after which it becomes stationary just to the south. It begins to move northward at ~1200 UTC, passing

MS6 as a warm front at 1440 UTC. Over the Rush Valley where MS6 is located, the frontal movement is continuous, but over Utah Valley the movement is discontinuous as the shallow cold airmass is removed by turbulent erosion. The warm front moves northward to near the southern shore of the Great Salt Lake, where, at ~2015 UTC, it reverses directions and becomes a cold front. Due to the interaction of the frontal boundary and low center with the local basin and range topography, MS6 observes the passage of two cold-frontal segments, one from the west at 2110 UTC and one from the north at 2210 UTC.

Conclusions

This paper utilizes high-density surface observations and high-resolution surface analyses to examine the life cycle of an Intermountain cyclone and its attendant fronts. The cyclone, known locally as the "Tax Day Storm" produced the second lowest sea level pressure ever reported in Utah and the strongest cold front passage observed at KSLC in the past 25 y.

As an upper-level PV anomaly and trough approaches the Pacific coast, an airstream boundary, which we have dubbed the *Great Basin Confluence Zone* (GBCZ), forms downstream from the Sierra Nevada. Contemporaneously, a baroclinic trough, which was initially draped along northern Nevada border, moves southward. Ultimately the GBCZ collects and concentrates the baroclinity from the northern Great Basin, including that associated with the approaching baroclinic trough. As the upper-level PV anomaly and trough crest the Sierra-Cascade ranges, QG forcing for ascent becomes focused over Nevada and rapid cyclogenesis and frontogenesis occur along the GBCZ. As the system rapidly amplifies, a cloud and precipitation shield develops over the

postfrontal airmass, contributing to diabatic frontogenesis and apparently aiding the dramatic frontal scale collapse that occurs from 1700-1800 UTC over Nevada. Over northern Utah, front-mountain interactions lead to a complex frontal evolution including dramatic frontal distortions, apparent discontinuous movement of a warm front due to the turbulent erosion of a shallow, persistent cold pool within Utah Valley, and the passage of multiple cold-frontal segments over the Rush Valley.

The GBCZ is a distinctive and important mesoscale feature in this event. Plots of contraction, baroclinity, and frontogenesis illustrate that confluent deformation and convergence associated with the GBCZ collect and organize baroclinity in the region over an extended period of time. Surface cyclogenesis occurs along the resulting frontal zone as opposed to within the barrier-parallel lee trough as might be inferred from other lee cyclone studies. The quasi-stationary nature of the GBCZ suggests that it is tied to topography, namely the high Sierra. Although other mountain-induced confluence/ convergence zones have been identified elsewhere (e.g., Mass 1981; Doyle 1997; Andretta and Hazen 1998; Antonescu and Burcea 2009), the role the GBCZ plays in the genesis of cyclones and fronts over the Great Basin seems to be unique.

Diabatic processes such as differential sensible heating due to cross-front contrasts in cloud cover, and sub-cloud diabatic cooling from precipitation also contribute significantly to the frontal development in this case. Potential temperature changes along trajectories indicate that direct diabatic contributions, although varying along the front, explain up to 40% of the cross-front baroclinity. The dramatic scale collapse of the front from 1700-1800 UTC likely results from the combined effects of the GBCZ and geostrophic adjustment, which may be nonlinearly enhanced by thermally induced

circulations from diabatic processes (as in Koch et al. 1995). This is one of several Intermountain front cases where diabatic processes are implicated or shown to be important to frontogenesis (e.g., Schultz and Trapp 2003; SS08; Steenburgh et al. 2009).

Finally, the frontal analyses over northern Utah illustrate just some of the complications of analysis and forecasting over the Intermountain West, including the effects of mesoscale topography on frontal movement and structure. The Tax Day Storm provides an example of a significant deviation from the classical Norwegian and Shapiro and Keyser (1990) cyclone models, and illustrates the complex interactions of large-scale forcing with the terrain of the Intermountain West at various scales. This research furthers our understanding and prediction of these events, and, in particular, provides the first detailed examination of the GBCZ. Uncertainties regarding the underlying mechanisms responsible for the GBCZ, given its role in the formation of cyclones and strong cold fronts that bring threats to life and property in the most rapidly growing region in the United States, warrant further research.

References

Aebischer, U., and C. Schär, 1998: Low-level potential vorticity and cyclogenesis to the lee of the Alps. *J. Atmos. Sci*., **55**, 186–207.

Andretta, T. A., and D. S. Hazen, 1998: Doppler analysis of a Snake River Plain convergence event. *Wea. Forecasting,* **13,** 482–491.

Antonescu, B., and S. Burcea, 2010: The cloud-to-ground lightning climatology for Romania. *Mon. Wea. Rev.*, **138,** 579–591.

Bannon, P. R., 1992: A model of Rocky Mountain lee cyclogenesis. *J. Atmos. Sci.,* **49**, 1510-1522.

Barnes, S. L., F. Caracena, and A. Marroquin, 1996: Extracting synoptic-scale diagnostic information from mesoscale models: The Eta model, gravity waves, and quasigeostrophic diagnostics. *Bull. Amer. Meteor. Soc.,* **77**, 519-528.

Benjamin, S. G., and Coauthors, 2004: An hourly assimilation–forecast cycle: The RUC. *Mon. Wea. Rev*., **132**, 495–518.

Bergeron, T., 1937: On the physics of fronts. *Bull. Amer. Meteor. Soc.,* **18**, 265–275.

Bergeron, T., 1959: Methods in scientific weather analysis and forecasting: An outline in the history of ideas and hints at a program. *The Atmosphere and the Sea in Motion: Scientific Contributions to the Rossby Memorial Volume*. B. Bolin, Ed., Rockefeller Institute Press, 440-474.

Bjerknes, J., 1919: On the structure of moving cyclones. *Geofys. Publ.,* **1**(2), 1–8.

Bjerknes, J., and H. Solberg, 1922: Life cycle of cyclones and the polar front theory of atmospheric circulation. *Geofys. Publ.*, **3**(1), 3–18.

Blackman, R. B., and J. W. Tukey, 1958: The measurement of power spectra from the point of view of communications engineering. Dover Publications, 190pp.

Bleck, R., and C. Mattocks, 1984: A preliminary analysis of the role of potential vorticity in Alpine lee cyclogenesis. *Contrib. Atmos. Phys.,* **57**, 357–368.

Brewster, K. A., 1996: Application of a Bratseth analysis scheme including Doppler radar data. Preprints, *15th Conf. on Weather Analysis and Forecasting*, Norfolk, VA, Amer. Meteor. Soc., 92–95.

Buzzi, A., and S. Tibaldi, 1978: A case study of Alpine lee cyclogenesis. *Quart. J. Roy. Meteor. Soc.*, **104**, 271-287.

Chien, F.-C., and Y.-H. Kuo, 2006: Topographic effects on a wintertime cold front in Taiwan. *Mon. Wea. Rev.,* **134**, 3297-3316.

Cohen, R. A., and C. W. Kreitzberg, 1997: Airstream boundaries in numerical weather simulations. *Mon. Wea. Rev*., **125**, 168-183.

Cohen, R. A., and D. M. Schultz, 2005: Contraction rate and its relationship to frontogenesis, the Lyapunov exponent, fluid trapping, and airstream boundaries. *Mon. Wea. Rev*., **133**, 1353-1369.

Davis, C. A., 1997: The modification of baroclinic waves by the Rocky Mountains. *J. Atmos. Sci.,* **54**, 848-868.

Davis, C. A., and M. T. Stoelinga, 1999: The transition to topographic normal modes. *J. Atmos. Sci.,* **56**, 3321-3330.

Doyle, J. D., 1997: The influence of mesoscale orography on a coastal jet and rainband.

Mon. Wea. Rev., **125**, 1465-1488.

Eliassen, A., 1990: Transverse circulations in frontal zones. *Extratropical Cyclones: The Erik Palmén Memorial Volume*, C. W. Newton and E. O. Holopainen, Eds., Amer. Meteor. Soc., 155-165.

Gallus, W. A., Jr., and M. Segal, 1999: Diabatic effects on late-winter cold front evolution: Conceptual and numerical model evaluations. *Mon. Wea. Rev.,* **127**, 1518-1537.

Haagenson, P. L., K. Gao, and Y.-H. Kuo, 1990: Evaluation of meteorological analyses, simulations, and long-range transport calculations using ANATEX surface tracer data. *J. Appl. Meteor.*, **29**, 1268–1283.

Hill, C. D., 1993: Forecast problems in the western region of the National Weather Service: An overview. *Wea. Forecasting*, **8**, 158-165.

Hobbs, P. V., J. D. Locatelli, and J. E. Martin, 1996: A new conceptual model for cyclones generated in the lee of the Rocky Mountains. *Bull. Amer. Meteor. Soc.*, **77**, 1169-1178.

Horel, J. D., and C. V. Gibson, 1994: Analysis and simulation of a winter storm over Utah. *Wea. Forecasting*, **9**, 479-494.

Horel, J. D., M. Splitt, L. Dunn, J. Pechmann, B. White, C. Ciliberti, S. Lazarus, D. Zaff, and J. Burks, 2002: Mesowest: Cooperative mesonets in the western United States. *Bull. Amer. Meteor. Soc*., **83**, 211-225.

Hoskins, B. J., and F. P. Bretherton, 1972: Atmospheric frontogenesis models: Mathematical formulation and solution. *J. Atmos. Sci*., **29**, 11–37.

Hoskins, B. J., and M. A. Pedder, 1980: The diagnosis of middle latitude synoptic development. *Quart. J. Roy. Meteor. Soc.*, **106**, 707-719.

Hoskins, B. J., I. Draghici, and H. C. Davies, 1978: A new look at the ω-equation. *Quart. J. Roy. Meteor. Soc.*, **104**, 31-38.

Hoskins, B. J., M. McIntyre, and A. Robertson, 1985: On the use and significance of isentropic potential vorticity maps. *Quart. J. Roy. Meteor. Soc.*, **111**, 877–946.

Iino, N., K. Kinoshita, A. C. Tupper, and T. Yano, 2004: Detection of Asian dust aerosols using meteorological satellite data and suspended particulate matter concentrations. *Atmos. Env*., **38**, 6999-7008.

Jeglum, M. E., 2010: Multi-Scale Reanalysis Climatology of Intermountain Cyclones. M. S. thesis, Department of Atmospheric Sciences, University of Utah, 59 pp.

Junker, N. W., J. E. Hoke, and R. H. Grumm, 1989: Performance of NMC's regional models. *Wea. Forecasting*, **4**, 368-390.

Junker, N. W., J. E. Hoke, B. E. Sullivan, K. F. Brill, and F. J. Hughes, 1992: Seasonal and geographic variations in quantitative precipitation prediction by NMC's nested-grid model and medium-range forecast model. *Wea. Forecasting*, **7**, 410-429.

Koch, S. E, J. T. McQueen, and V. M. Karyampudi, 1995: A numerical study of the effects of differential cloud cover on cold frontal structure and dynamics. *J. Atmos. Sci.*, **52**, 937-964.

Koch, S. E., A. Aksakal, and J. T. McQueen, 1997: The influence of mesoscale humidity and evapotranspiration fields on a model forecast of a cold-frontal squall line. *Mon. Wea. Rev.*, **125**, 384-409.

Lazarus, S. M., C. M. Ciliberti, J. D. Horel, and K. A. Brewster, 2002: Near-real-time applications of a mesoscale analysis system to complex terrain. *Wea. Forecasting*, **17**, 971–1000.

Lee, T. P., 1995: Intermountain cyclogenesis: A climatology and multiscale case studies. Ph.D. Dissertation, Department of Atmospheric Sciences, State University of New York at Albany, 399 pp.

Locatelli, J. D., R. D. Schwartz, M. T. Stoelinga, and P. V. Hobbs, 2002: Norwegian-type and cold front aloft-type cyclones east of the Rocky Mountains. *Wea. Forecasting*, **17**, 66-82.

Maddox, R. A., J. Zhang, J. J. Gourley, and K. W. Howard, 2002: Weather radar coverage over the contiguous United States. *Wea. Forecasting*, **17,** 927–934.

Market, P. S., and J. T. Moore, 1998: Mesoscale evolution of a continental occluded cyclone. *Mon. Wea. Rev.*, **126**, 1793-1811.

Martin, J. E., 1998: The structure and evolution of a continental winter cyclone. Part I: Frontal structure and the occlusion process. *Mon. Wea. Rev.*, **126**, 303-328.

Mass, C., 1981: Topographically forced convergence in western Washington State. *Mon. Wea. Rev.*, **109**, 1335-1347.

Mattocks, C., and R. Bleck, 1986: Jet streak dynamics and geostrophic adjustment processes during the initial stages of lee cyclogenesis. *Mon. Wea. Rev.*, **114**, 2033–2055.

McDonald, B. E., 1998: Sensitivity of precipitation forecast skill to horizontal resolution.

Ph.D. Dissertation, Dept. of Meteorology, University of Utah, 135 pp.

McGinley, J., 1982: A diagnosis of Alpine lee cyclogenesis. *Mon. Wea. Rev*., **110**, 1271-1287.

Myrick, D. T., J. D. Horel, and S. M. Lazarus, 2005: Local adjustment of the background error correlation for surface analyses over complex terrain. *Wea. Forecasting*, **20**, 149–160.

O'Handley, C., and L. F. Bosart, 1996: The impact of the Appalachian Mountains on cyclonic weather systems. Part I: A climatology. *Mon. Wea. Rev.,* **124**, 1353-1373.

Painter, T. H., A. P. Barrett, C. Landry, J. Neff, M. P. Cassidy, C. Lawrence, K. E. McBride, and G. L. Farmer, 2007: Impact of disturbed desert soils on duration of mountain snowcover. *Geophys. Res., Lett*., **34**, L12502, doi:10.1029/2007GL030284R.

Petterssen S., 1936: Contribution to the theory of frontogenesis. *Geofys. Publ*., **11**(6), 1–27.

Petterssen, S., 1956: *Weather Analysis and Forecasting.* Vol. 1, *Motion and Motion Systems*, 2d ed., McGraw-Hill, 428 pp.

Rossby, C.-G., 1934: Comments on meteorological research. *J. Aeronaut. Sci,* **1**, 32-34.

Rowson, D. R., and S. J. Colucci, 1992: Synoptic climatology of thermal low-pressure systems over south-western North America. *Int. J. Climatol.,* **12**, 529-545.

Sanders, F., 1999: A proposed method of surface map analysis. *Mon. Wea. Rev.,* **127**, 945-955.

Schultz, D. M., and C. F. Mass, 1993: The occlusion process in a midlatitude cyclone over land. *Mon. Wea. Rev.,* **121,** 918–940.

Schultz, D. M., and C. A. Doswell III, 2000: Analyzing and forecasting Rocky Mountain lee cyclogenesis often associated with strong winds. *Wea. Forecasting*, **15**, 152-173.

Schultz, D. M., and R. J. Trapp, 2003: Nonclassical cold-frontal structure caused by dry subcloud air in northern Utah during the Intermountain Precipitation Experiment (IPEX). *Mon. Wea. Rev*., **131**, 2222–2246.

Schultz, D. M., D. Keyser, and L. F. Bosart, 1998: The effect of large-scale flow on low-level frontal structure and evolution in midlatitude cyclones. *Mon. Wea. Rev.*, **126**, 1767-1791.

Schultz, D. M., and Coauthors, 2002: Understanding Utah winter storms: The Intermountain Precipitation Experiment. *Bull. Amer. Meteor. Soc.,* **83,** 189–210.

Segal, M., E. A. Aligo, and W. A. Gallus Jr., 2004: A conceptual and scaling evaluation of the surface wetness effect on daytime moisture convergence along a surface cold front with differential cloud cover. *J. Hydromet.*, **5**, 365-371.

Shafer, J. C., and W. J. Steenburgh, 2008: Climatology of strong Intermountain cold fronts. *Mon. Wea. Rev*., **136**, 784-807.

Shafer, J. C., W. J. Steenburgh, J. A. W. Cox, and J. P. Monteverdi, 2006: Terrain influences on synoptic storm structure and mesoscale precipitation distribution during IPEX IOP3. *Mon. Wea. Rev*., **134**, 478-497.

Shapiro, M. A., and D. Keyser, 1990: Fronts, jet streams and the tropopause. *Extratropical Cyclones: The Erik Palmén Memorial Volume,* C. W. Newton and E. O. Holopainen, Eds., Amer. Meteor. Soc., 167–191.

Smith, R. B., 1984: A theory of lee cyclogenesis. *J. Atmos. Sci.*, **41**, 1159-1168.

Splitt, M. E., and J. D. Horel, 1998: Use of multivariate linear regression for meteorological data analysis and quality assessment in complex terrain. Preprints, *10th Symp. on Meteorological Observations and Instrumentation*, Phoenix, AZ, Amer. Meteor. Soc., 359–362.

Steenburgh, W. J., and C. F. Mass, 1994: The structure and evolution of a simulated Rocky Mountain lee trough. *Mon. Wea. Rev.*, **122**, 2740-2761.

Steenburgh, W. J., and T. R. Blazek, 2001: Topographic distortion of a cold front over the Snake River Plain and central Idaho Mountains. *Wea. Forecasting*, **16**, 301–314.

Steenburgh, W. J., C. R. Neuman, G. L. West, and L. F. Bosart, 2009: Discrete frontal propagation over the Sierra-Cascade Mountains and Intermountain West. *Mon. Wea. Rev*., **137**, 2000-2020.

Steinacker, R., 1982: The first ALPEX-SOP cold-front on March 2, 1982. *ALPEX Preliminary Scientific Results,* J. P. Kuettner, Ed., GARP-ALPEX7, WMO, 87–96.

Tibaldi, S., A. Buzzi, and A. Speranza, 1990: Orographic cyclogenesis. *Extratropical Cyclones: The Eric Palmen Memorial Volume,* C.W. Newton and E.O. Holopainen, Eds., Amer. Meteor. Soc., 107-127.

United States Geological Survey National Wetlands Research Center, cited 2010: Great Basin Hydrographic Region. [Retrieved online 8 Apr 2010 at http://www.nwrc.usgs.gov/techrpt/85-7-24map.jpg.]

West, G. L., and W. J. Steenburgh, 2010: Life cycle and mesoscale frontal structure of an Intermountain cyclone. *Mon. Wea. Rev.,* in press.

Westrick, K. J., C. F. Mass, and B. A. Colle, 1999: The limitations of the WSR-88D radar network for quantitative precipitation measurement over the coastal western United States. *Bull. Amer. Meteor. Soc*., **80**, 2289-2298.

Whiteman, C. D., 2000: *Mountain Meteorology: Fundamentals and Applications.* Oxford University Press, 355 pp.

Whittaker, L. M., and L. H. Horn, 1981: Geographical and seasonal distribution of North American cyclogenesis, 1958-1977. *Mon. Wea. Rev.,* **109**, 2312-2322.

Xue, M., K. K. Droegemeier, and V. Wong, 2000: The Advanced Regional Prediction System (ARPS)—A multiscale nonhydrostatic atmospheric simulation and prediction model. Part I: Model dynamics and verification. *Meteor. Atmos. Phys*., **75**, 161–193.

Xue, M., and Coauthors, 2001: The Advanced Regional Prediction System (ARPS)—A multiscale nonhydrostatic atmospheric simulation and prediction tool. Part II: Model physics and applications. *Meteor. Atmos. Phys*., **76**, 143–165.

Xue, M., D. Wang, J. Gao, K. Brewster, and K. K. Droegemeier, 2003: The Advanced Regional Prediction System (ARPS), storm-scale numerical weather prediction and data assimilation. *Meteor. Atmos. Phys*., **82**, 139–170.

Yuan, H., S. L. Mullen, X. Gao, S. Sorooshian, J. Du, and H.-M. H Juang, 2007: Short-range probabilistic quantitative forecasts over the southwest United States by the RSM ensemble system. *Mon. Wea. Rev*., **135**, 1685-1698.

Zishka, K. M., and P. J. Smith, 1980: The climatology of cyclones and anticyclones over North America and surrounding ocean environs for January and July, 1950–77. *Mon. Wea. Rev.*, **108**, 387-401.

CHAPTER 3

SYNOPTIC-OROGRAPHIC INFLUENCES ON INTERMOUNTAIN FRONTAL EVOLUTION

Abstract

Orography has a dramatic influence on cold-front evolution over the western United States. This study investigates this influence using real-data and idealized model simulations. First, simulations with and without the Sierra Nevada are used to examine the influence of the mountain range on an intense Intermountain cold front event on 25 Mar 2006. Inclusion of the Sierra Nevada has little influence on temperatures on the cold side of the baroclinic zone to the north, where terrain height differences are relatively small, but produces a 2-8 K warm anomaly to the south, downstream of the high Sierra, predominantly in the prefrontal airmass, resulting in a larger cross-front potential temperature contrast. Blocking and deflection of cold air by the high Sierra, latent heating within the orographic cloud on the windward slope, leeward warming and drying from subsidence, and reduced cloud cover and precipitation all contribute to this warm anomaly. Other downstream effects of the range, which are most pronounced closer the barrier, include frontal retardation and enhanced contraction (deformation and divergence).

We further explore synoptic-orographic influences on Intermountain cold front evolution using three idealized baroclinic cyclone simulations with the cyclone center initialized off the Pacific Coast at three positions 5° latitude apart. In all simulations frontogenesis is locally enhanced as onshore flow decelerates along the Pacific Coast and along the lower windward slopes of the Coast Range. Cold air penetrates across the Cascades and northern Sierra Nevada into the Intermountain West, but is blocked to the south by the high Sierra, which have a dramatic influence on frontal movement and orientation. In the two simulations with the southernmost low-center initializations, the high Sierra also enhance kinematic frontogenesis over Nevada, whereas in the northernmost simulation, no such enhancement is apparent and the front remains weak. These results imply that certain front orientations and more southerly track storms may be more favorable for the development of the Great Basin Confluence Zone and subsequent frontogenesis over the Intermountain West. Lastly, in the southernmost simulation, cold air is able to penetrate around the southern periphery of the high Sierra, producing a nonclassical type of orographic occlusion.

Introduction

Frontal interactions with orography have been documented ever since Bjerknes and Solberg (1922) described the first frontal cyclone model. Over the topographically complex western United States, mountains play a major role in frontal evolution (e.g., Braun et al. 1997; Colle et al. 1999; Steenburgh and Blazek 2001; Colle et al. 2002; Shafer et al. 2006; Shafer and Steenburgh 2008; Steenburgh et al. 2009). The COAST, CALJET, and IMPROVE-2 field campaigns greatly improved our understanding of the interaction of land-falling fronts with the topography of the Pacific Coast (e.g., Braun et

al. 1997; Doyle 1997; Colle et al. 1999; Yu and Smull 2000). Using intensive observational periods, model simulations of real cases, and model sensitivity studies they found that apparent low-level upstream blocking and frictional effects along the coast retard fronts, and enhance prefrontal southerly flow, enhancing confluent deformation, and ultimately frontogenesis. Colle et al. (2002) confirm this apparent topographical effect by conducting a model sensitivity study in which coastal topography is removed, which produces a weaker front.

Over the Intermountain West, several observational studies (Steenburgh and Blazek 2001; Shafer et al. 2006; Shafer and Steenburgh 2008; Steenburgh et al. 2009; Chapter 2 of this dissertation) and a limited number of modeling studies (Horel and Gibson 1994; Steenburgh et al. 2009) document various apparent manifestations of frontal interaction with the complex topography of the region. Specifically, retardation and blocking of cold air on the windward slope of the Sierra Nevada (Shafer et al. 2006; Steenburgh and Blazek 2001), discrete frontal propagation over the Sierra-Cascade ranges (Steenburgh et al. 2009), dramatic frontal distortions (Steenburgh and Blazek 2001; Chapter 2 of this dissertation), and perhaps most importantly, the Great Basin Confluence Zone (GBCZ, an area of confluent deformation and convergence extending downstream from the Sierra Nevada; Chapter 2 of this dissertation). None of these apparent front-mountain interactions, however, have been definitively proven via sensitivity studies.

Idealized, theoretical modeling studies are another method for investigating basic front-mountain interactions. Such studies in the 1980s and early 1990s examined these interactions through the use of simplified shallow water and stably stratified atmospheric

models over smooth terrain (e.g., Bannon 1983; Davies 1984; Blumen and Gross 1987; Schumann 1987; Zehnder and Bannon 1988; Williams et al. 1992). These studies generally find deceleration upstream of the barrier, windward slope acceleration, followed by deceleration in the lee. There are, however, some disagreements depending on the simplifications and assumptions invoked. For example, Davies (1984), using a shallow water model, finds frontal retardation over the windward slope, while Blumen and Gross (1987) and Zehnder and Bannon (1988), using stably stratified semigeostrophic models, find frontal acceleration over the windward slope. Further, some findings are rarely observed in the real world; Blumen and Gross (1987) find frontal acceleration over the windward slope, compared to blocking found in many observational studies (e.g., Kurz 1990; O'Handley and Bosart 1996; Schumacher et al. 1996; Chien and Kuo 2006).

While the studies mentioned above undoubtedly lend insight into possible processes behind front-mountain interactions, more realistic and comprehensive models, by their very nature, will likely produce more realistic results. Braun et al. (1999a) obtain results in good agreement with the observed cases along the Pacific Coast by incorporating simplified terrain representative of the region, while Braun et al. (1999b) and Peng et al. (2001) find the addition of a boundary layer parameterization produces a more realistic frontal structure in frontal simulations over orography, including enhanced windward retardation and frontogenesis. Olson and Colle (2007) add far more realism, developing a technique for initializing a three-dimensional idealized cyclone with realistic fronts in the fifth-generation Pennsylvania State University-National Center for Atmospheric Research Mesoscale Model (MM5) and Weather Research and Forecasting

(WRF) model. Their paper briefly presents a terrain/no terrain comparison confirming similar aforementioned findings of frontal retardation along the Pacific Coast in the presence of terrain, but perhaps more importantly, they provide a valuable tool for further investigation of synoptic-orographic influences on frontal evolution.

Our approach to this problem will be two-fold. First, we revisit the 25 Mar 2006 case considered by Steenburgh et al. (2009), performing a sensitivity study in which the Sierra Nevada are removed. Second, we utilize the idealized cyclone initialization technique of Olson and Colle (2007) to examine the effects of altering the position and angle of incidence of a land-falling cold front over the western United States.

Data and Methods

For the first section of this study, we use the Advanced Research Weather Research and Forecasting (WRF ARW) model version 2 (Skamarock et al. 2005). Two simulations are performed. The first, FULLTERR, is identical to the control run described by Steenburgh et al. (2009), features unaltered model topography (Fig. 3.1), and an inner domain (the only domain presented here) covering the Intermountain West at 12-km grid spacing. In the second simulation, NOSIERRA, we restrict the height of the Sierra Nevada and extreme southern Cascades of California to an elevation of no more than 1500 m, the approximate mean elevation of the valleys and basins of the Intermountain West (Fig. 3.1). The resulting terrain height differences are relatively small over the northern Sierra and southern Cascades, but much larger south of Lake Tahoe along the high Sierra (Fig. 3.1).

For the idealized cyclone simulations presented in the second section of this study, the WRF ARW model is configured with an outer (inner) domain with 481x286

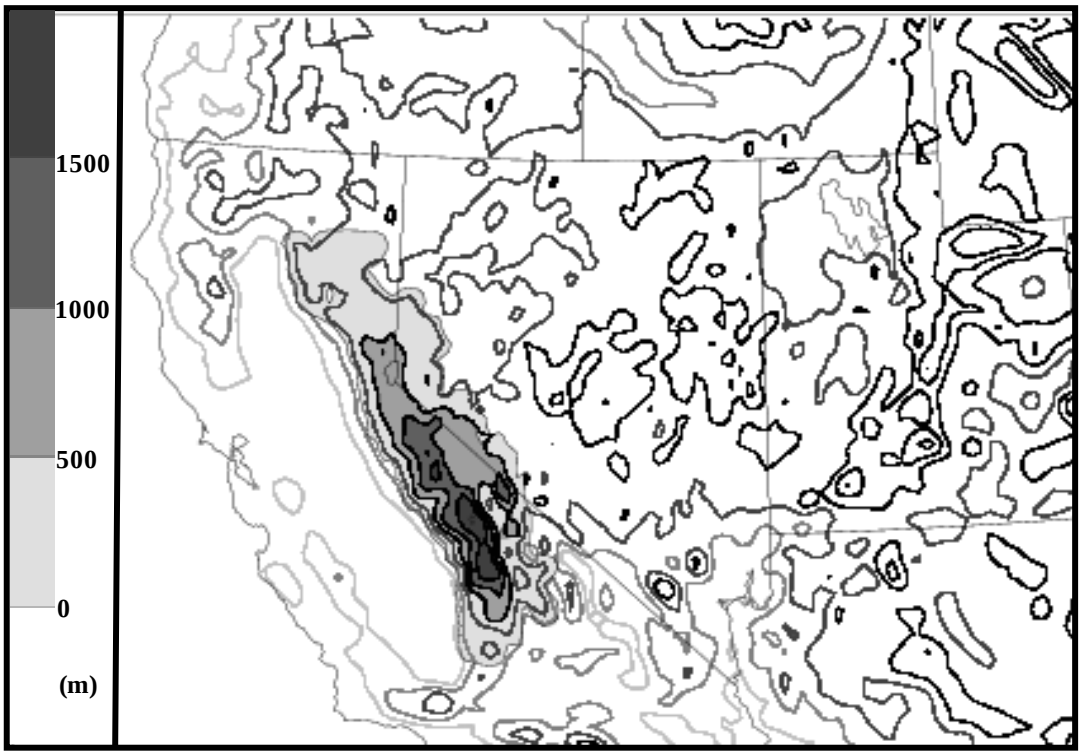

Figure 3.1. Model terrain overview. Model terrain height for FULLTERR (contoured every 500 m), and FULLTERR–NOSIERRA terrain height difference (m, shaded according to scale).

(301x256) grid points and 36-km (12-km) grid spacing (Fig. 3.2). The large outer domain enables the area of study to be far from the model boundaries, and the inner domain is initialized using initial and boundary conditions from the outer domain, 12 hours into the outer domain simulation. The cyclone is initialized at a fixed position with respect to the outer domain; therefore by repositioning the outer domain, the cyclone is repositioned (cf. Figs. 3.2a-c). In the SOUTH simulation (Fig. 3.2c), the domain is centered at 36° N, 102° W, yielding a cyclone position nearly identical to that in the 25 Mar 2006 case at landfall. In CENTRAL (Fig. 3.2b) and NORTH (Fig. 3.2a) the longitudinal position remains the same, but the latitudes of the domain centers are shifted to 41° N and 46° N, respectively. The ideal cyclone (Fig. 3.2) is based on the moderate basic baroclinic state from Olson and Colle (2007). No radiation or moisture is included, and the Yonsei University (YSU; Hong et al. 2006) boundary layer parameterization is used.

WRF data are plotted using Read Interpolate Plot (RIP) version 4 (Stoelinga 2009), and for figure clarity all fields are smoothed using a 7-point cowbell spectral filter (Barnes et al. 1996). Where the 850-hPa surface is below the model terrain, geopotential height is based on hydrostatic extrapolation.

Following Steenburgh et al. (2009), surface frontogenesis is defined following Petterssen (1936) and Miller (1948) as

$$F = \frac{d}{dt}\left|\nabla_\eta \theta\right|, \tag{1}$$

where

$$\frac{d}{dt} = \frac{\partial}{\partial t} + u\frac{\partial}{\partial x_\eta} + v\frac{\partial}{\partial y_\eta} + \dot{\eta}\frac{\partial}{\partial \eta}, \tag{2}$$

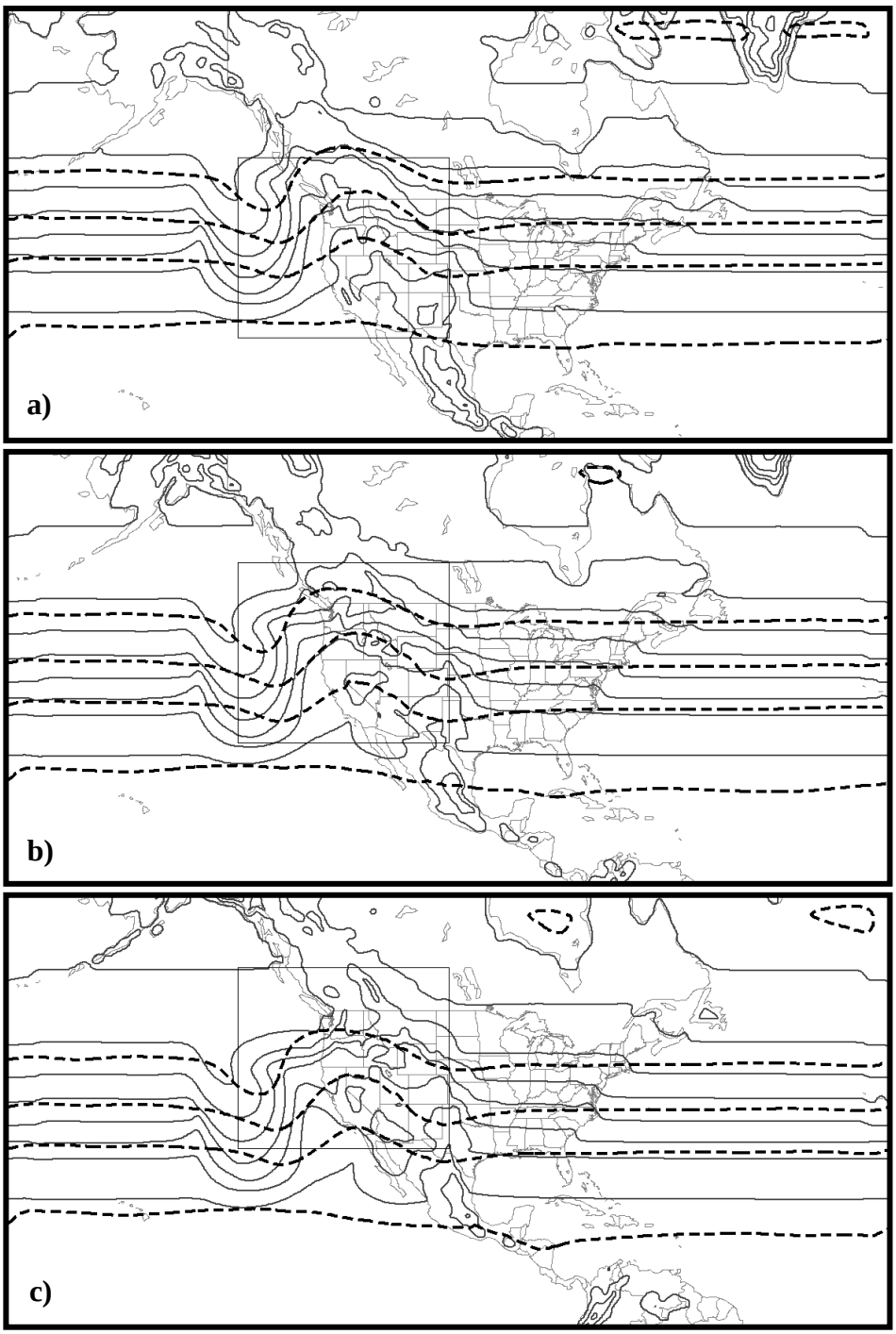

Figure 3.2. Idealized initialization overview. 500-hPa geopotential height (black dashed contours, every 120 m) and lowest sigma-level potential temperature (gray contours every 3 K) at time of inner domain initialization. Outer domain area plotted, inner domain area indicated by inset box.

$$\nabla_\eta = \mathbf{i}\frac{\partial}{\partial x_\eta} + \mathbf{j}\frac{\partial}{\partial y_\eta}, \tag{3}$$

the subscript η denotes differentiation along the lowest η level, and $\dot{\eta}$ is n the η-coordinate vertical velocity. Following Miller (1948), Eq. (1) may be written as

$$F = F_W + F_T + F_D, \tag{4}$$

where

$$F_W = -\frac{1}{\left|\nabla_\eta \theta\right|}\left[\frac{\partial\theta}{\partial x}\left(\frac{\partial u}{\partial x}\frac{\partial\theta}{\partial x} + \frac{\partial u}{\partial y}\frac{\partial\theta}{\partial y}\right) + \frac{\partial\theta}{\partial y}\left(\frac{\partial v}{\partial x}\frac{\partial\theta}{\partial x} + \frac{\partial v}{\partial y}\frac{\partial\theta}{\partial y}\right)\right], \tag{5}$$

$$F_T = -\frac{1}{\left|\nabla_\eta \theta\right|}\left[\frac{\partial\theta}{\partial\eta}\left(\frac{\partial\dot{\eta}}{\partial x}\frac{\partial\theta}{\partial x} + \frac{\partial\dot{\eta}}{\partial y}\frac{\partial\theta}{\partial y}\right)\right], \tag{6}$$

$$F_D = -\frac{1}{\left|\nabla_\eta \theta\right|}\left[-\frac{\partial\theta}{\partial x}\frac{\partial}{\partial x}\frac{d\theta}{dt} - \frac{\partial\theta}{\partial y}\frac{\partial}{\partial y}\frac{d\theta}{dt}\right], \tag{7}$$

and the subscript η has been dropped for convenience. F_W, F_T, and F_D are the frontogenesis components produced by horizontal deformation and divergence (hereafter *kinematic frontogenesis*), tilting, and horizontal gradients in diabatic heating and cooling, respectively. Although F_T is nonzero due to the presence of a stable layer in the morning and a super-adiabatic layer in the afternoon, it does not appear to contribute significantly to frontal development and is not presented. F_D contains two components

$$F_D = F_M + F_{BL}, \tag{8}$$

where F_M is the *diabatic frontogenesis* produced by the WRF model cloud microphysics and cumulus parameterizations (including subcloud diabatic cooling from evaporation/

melting/sublimation; hereafter *moist frontogenesis*) and F_{BL} is the diabatic frontogenesis produced by the boundary layer and radiation parameterizations (hereafter *boundary layer frontogenesis*). We calculate F_M and F_{BL} from heating rates obtained directly from the WRF model parameterizations.

This study makes use of the kinematic quantity *instantaneous contraction rate* (Cohen and Schultz 2005), the summation of resultant deformation and divergence, which can be used to locate and quantify airstream boundaries. *Instantaneous contraction rate*, *C* (hereafter contraction), is defined as

$$C = \frac{E-D}{2}, \tag{3}$$

where

$$E = \left[\left(\frac{\partial u}{\partial x} - \frac{\partial v}{\partial y}\right)^2 + \left(\frac{\partial u}{\partial y} + \frac{\partial v}{\partial x}\right)^2\right]^{1/2} \tag{4}$$

is resultant deformation,

$$D = \frac{\partial u}{\partial x} + \frac{\partial v}{\partial y} \tag{5}$$

is divergence, differentiated along the lowest η level. For any point in the flow, contraction represents the maximum instantaneous rate at which two parcels are approaching each other, which occurs along the axis of contraction and normal to the axis of dilatation. Kinematic frontogenesis differs from contraction in that it is inclusive of the potential temperature gradient and depends on the orientation of the isentropes relative to the axis of dilatation (Cohen and Schultz 2005). In the presence of a potential temperature gradient, frontogenesis is maximized when the isentropes are aligned along the axis of dilatation and normal to the axis of contraction.

Influence of the Sierra Nevada on the 25 Mar 2006 Cold Front

Steenburgh et al. (2009) provide a thorough analysis of the 25 Mar 2006 case, including validation of FULLTERR (their control run). Here we concentrate on the influence of the Sierra Nevada (see Fig. 2.1 for geographic name places) on frontal evolution by comparing the FULLTERR and NOSIERRA simulations.

Mesoscale Analysis

At 1500 UTC a weakening occluded front moves inland across northern California, its position virtually identical in FULLTERR and NOSIERRA (cf. Figs. 3.3a, b). Ahead of the occluded front, confluent south-southwesterly flow extends across northeast California and northern Nevada (Figs. 3.4a and b). In FULLTERR, the Sierra Nevada alter this flow, forming two troughs and an airstream boundary over northwest Nevada [Fig. 3.4a; as analyzed in Steenburgh et al. (2009)], whereas a single continuous trough forms in NOSIERRA (Fig. 3.4b). Farther south, windward ridging and leeward troughing across the Sierra Nevada are markedly stronger in FULLTERR (cf. Figs. 3.3a, b). Potential temperatures are similar in both simulations immediately downstream of the northern Sierra Nevada and southern Cascades (within 2 K; cf. Figs. 3.4c, d), where terrain height differences between the two simulations are relatively small (Fig. 3.1). Farther south, potential temperatures are ~2-5 K higher in FULLTERR (cf. Figs. 3.4c, d), downstream of the high Sierra where terrain height difference are large (Fig. 3.1). Large differences in precipitation also exist between the simulations, most notably increased precipitation over the windward slopes of the high Sierra and no precipitation downstream over west-central Nevada in FULLTERR (cf. Figs. 3.3a, b). Diabatic frontogenesis is weak and disorganized at this time (Figs. 3.4c and d).

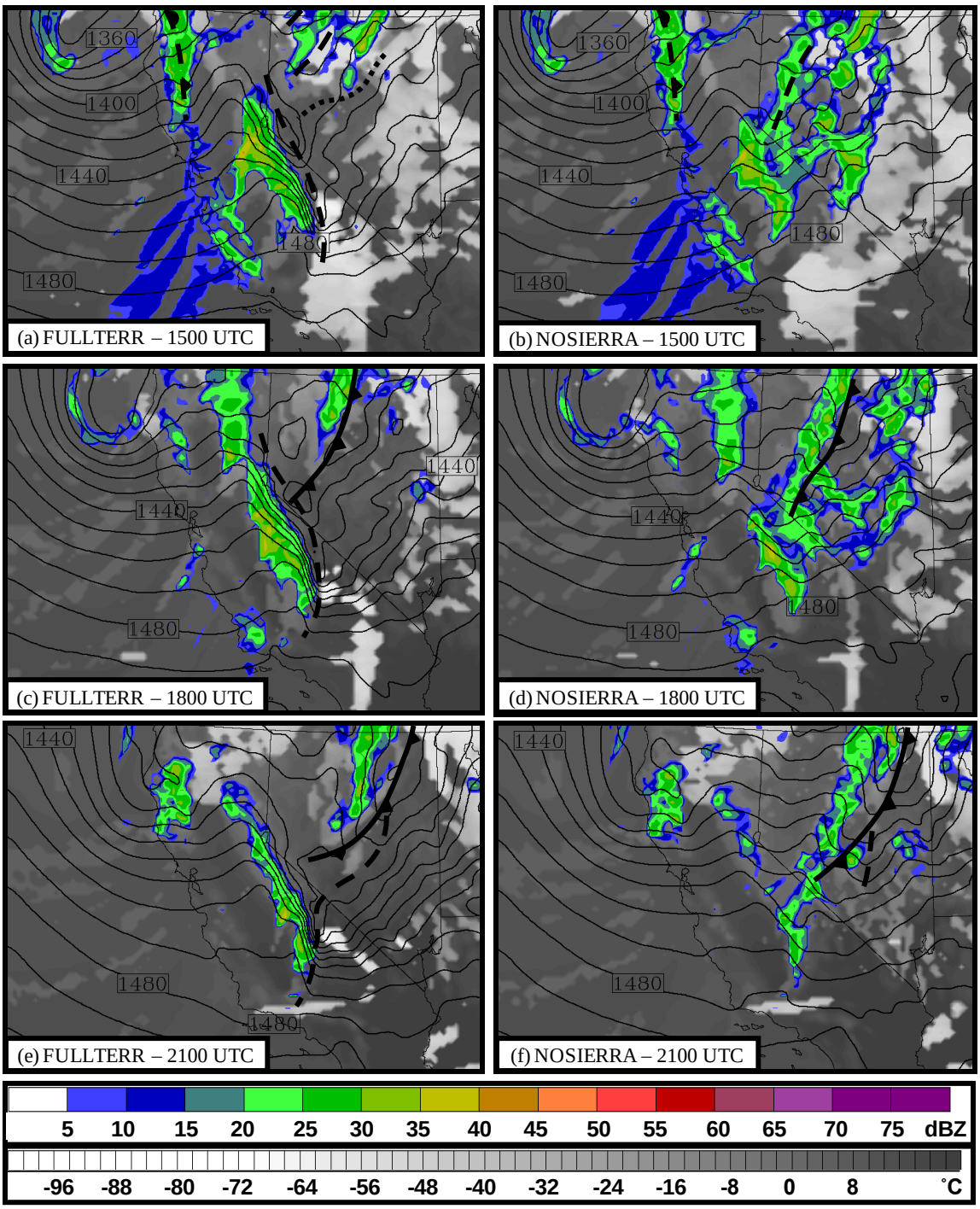

Figure 3.3. WRF 850-hPa geopotential height, clouds, and precipitation. 850-hPa geopotential height (contoured every 10m), WRF simulated equivalent radar reflectivity (color shading, shaded according to scale), and WRF cloud top temperatures (grey shading, according to scale) for a) FULLTERR at 1500 UTC, b) NOSIERRA at 1500 UTC, c) FULLTERR at 1800 UTC, d) NOSIERRA at 1800 UTC, e) FULLTERR at 2100 UTC, and f) NOSIERRA at 2100 UTC.

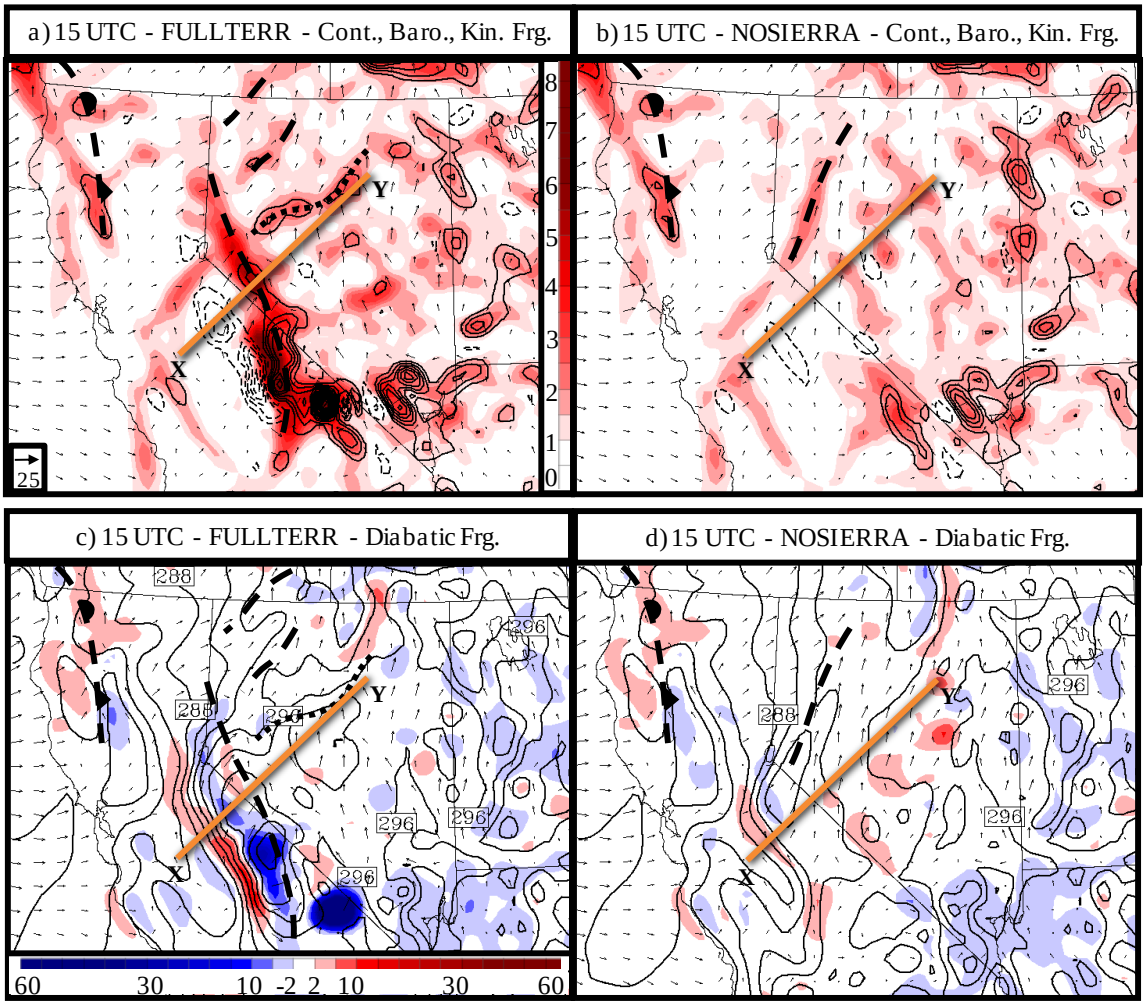

Figure 3.4. Mesoscale frontogenesis diagnostics. Lowest η-level contraction [shaded according to scale in (a), x10^{-4} s^{-1}], kinematic frontogenesis [solid contours, dashed negative, every 5 K (100 km)$^{-1}$ hr^{-1}], and wind vectors [according to scale in (a), m s^{-1}] for (a) FULLTERR and (b) NOSIERRA at 1500 UTC. Lowest η-level diabatic frontogenesis [shaded according to scale in (c), K (100 km)$^{-1}$ hr^{-1}], potential temperature (solid contours every 2 K), and wind vectors [as in (a)] for (c) FULLTERR and (d) NOSIERRA at 1500 UTC. Surface fronts are annotated using conventional frontal symbols, 850-hPa troughs using dashed lines, and lowest η-level airstream boundaries using dotted lines.

By 1800 UTC the airstream boundary and two troughs in FULLTERR merge, whereas in NOSIERRA the trough intensifies, forming a new cold front in both simulations (Figs. 3.5a and b). The initial frontal structure appears less organized in FULLTERR, although the magnitudes of contraction and kinematic frontogenesis are similar in both (cf. Figs. 3.5a, b). Blocking of cold air along the windward slope of the high Sierra in FULLTERR (cf. Figs. 3.5c, d) and deflection of flow around the high Sierra, contribute to an increased cross-front flow component along the southernmost portion of the front (cf. Figs. 3.5a, b). Potential temperatures along the cold side of the baroclinic zone are comparable in the two simulations, but are ~2-6 K higher in the prefrontal airmass. This results in a more substantial baroclinic zone with a larger total temperature contrast in FULLTERR (cf. Figs. 3.5c, d), despite a less organized kinematic field. In the northern postfrontal airmass, weak diabatic frontogenesis is present in both simulations, due to precipitation just behind the fronts associated with diabatic cooling (i.e., evaporation, sublimation, and melting; Figs. 3.5c and d). In the prefrontal airmass, large differences in precipitation and low-level cloud cover still exist downstream of the high Sierra where FULLTERR is much drier (cf. Figs. 3.3c, d).

At 2100 UTC both simulations have similar maximum contraction values, although the wind field in FULLTERR maintains a greater cross-front component along the central and southern portions of the front nearer to the high Sierra, where it also lags compared to the front in NOSIERRA (cf. Figs. 3.6a, b). Maximum baroclinity and kinematic frontogenesis values are also similar in both, but the baroclinic zone in FULLTERR remains more substantial, with a larger cross-front potential temperature contrast (cf. Figs. 3.6a, b and c, d). Again, this is primarily due to potential temperature

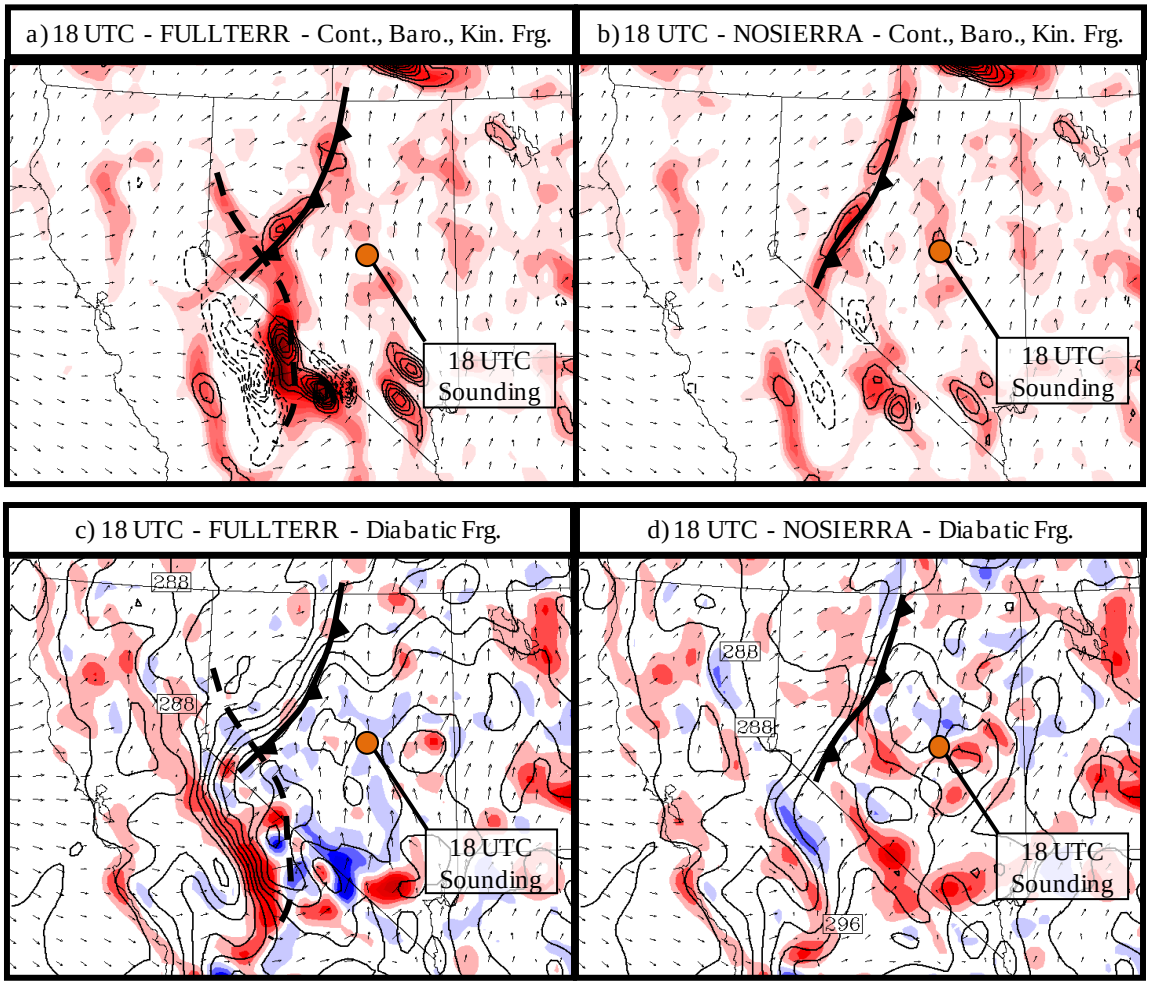

Figure 3.5. Mesoscale frontogenesis diagnostics. Lowest η-level contraction [shaded according to scale in Fig. 3.4a, x10^{-4} s^{-1}], kinematic frontogenesis [solid contours, dashed negative, every 5 K (100 km)$^{-1}$ hr^{-1}], and wind vectors [according to scale in Fig. 3.4a, m s^{-1}] for (a) FULLTERR and (b) NOSIERRA at 1800 UTC. Lowest η-level diabatic frontogenesis [shaded according to scale in (c), K (100 km)$^{-1}$ hr^{-1}], potential temperature (solid contours every 2 K), and wind vectors [as in (a)] for (c) FULLTERR and (d) NOSIERRA at 1800 UTC. Surface fronts are annotated using conventional frontal symbols, 850-hPa troughs using dashed lines, and lowest η-level airstream boundaries using dotted lines.

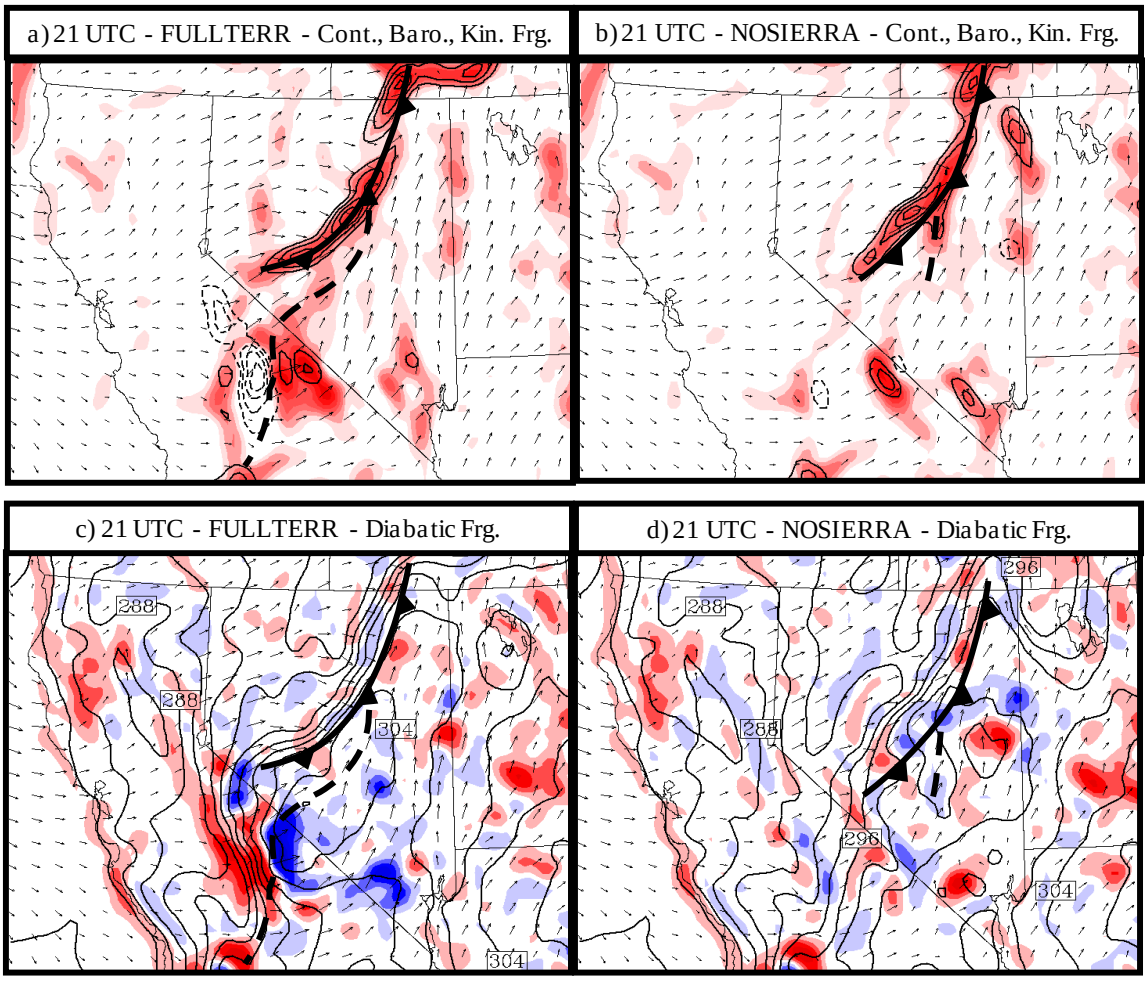

Figure 3.6. Mesoscale frontogenesis diagnostics. Lowest η-level contraction [shaded according to scale in Fig. 3.4a, x10^{-4} s^{-1}], kinematic frontogenesis [solid contours, dashed negative, every 5 K (100 km)$^{-1}$ hr^{-1}], and wind vectors [according to scale in Fig. 3.4a, m s^{-1}] for (a) FULLTERR and (b) NOSIERRA at 2100 UTC. Lowest η-level diabatic frontogenesis [shaded according to scale in (c), K (100 km)$^{-1}$ hr^{-1}], potential temperature (solid contours every 2 K), and wind vectors [as in (a)] for (c) FULLTERR and (d) NOSIERRA at 2100 UTC. Surface fronts are annotated using conventional frontal symbols, 850-hPa troughs using dashed lines, and lowest η-level airstream boundaries using dotted lines.

differences in the prefrontal airmass over Nevada that are now ~2-8K (cf. Figs. 3.6c, d). Postfrontal precipitation in both simulations (Figs. 3.3e and f) leads to diabatic frontogenesis (Figs. 3.6c and d), but it is locally stronger in FULLTERR (cf. Figs. 3.6c, d). The boundary layer component of diabatic frontogenesis partially cancels out the moist component [as described in Steenburgh et al. (2009), not explicitly shown here], weakening the diabatic frontogenesis contribution in both simulations.

Both cold fronts effectively reach maximum intensity at 0000 UTC 26 Mar (Fig. 3.7). In FULLTERR contraction is much stronger along the southern portion of the front, particularly the cross-front component of the winds (cf. Figs. 3.7a, b). The baroclinic zone is substantially larger, and maximum baroclinity values are ~25% stronger in FULLTERR [1.9K (100 km) $^{-1}$ versus 2.4K (100 km)$^{-1}$] over the central part of the front (cf. Figs. 3.9a, b). Similar baroclinity values persist over the next 3 h as the front progresses through northern Utah (not shown). Postfrontal precipitation is now stronger along the central portion of the front in FULLTERR (not shown), perhaps a consequence of stronger low-level convergence, resulting in stronger diabatic frontogenesis (cf. Figs. 3.7c, d).

Analysis of Warm Anomaly

As shown in the previous subsection, the primary factor contributing to the more substantial front in FULLTERR is a warm anomaly in the prefrontal airmass. In this subsection we investigate this anomaly, hashing out the major contributors.

The potential temperature anomaly begins to develop in the overnight hours, strengthening and growing outward from the immediate lee of the high Sierra. These initial differences appear to arise from several mechanisms, evident at 1500 UTC. First,

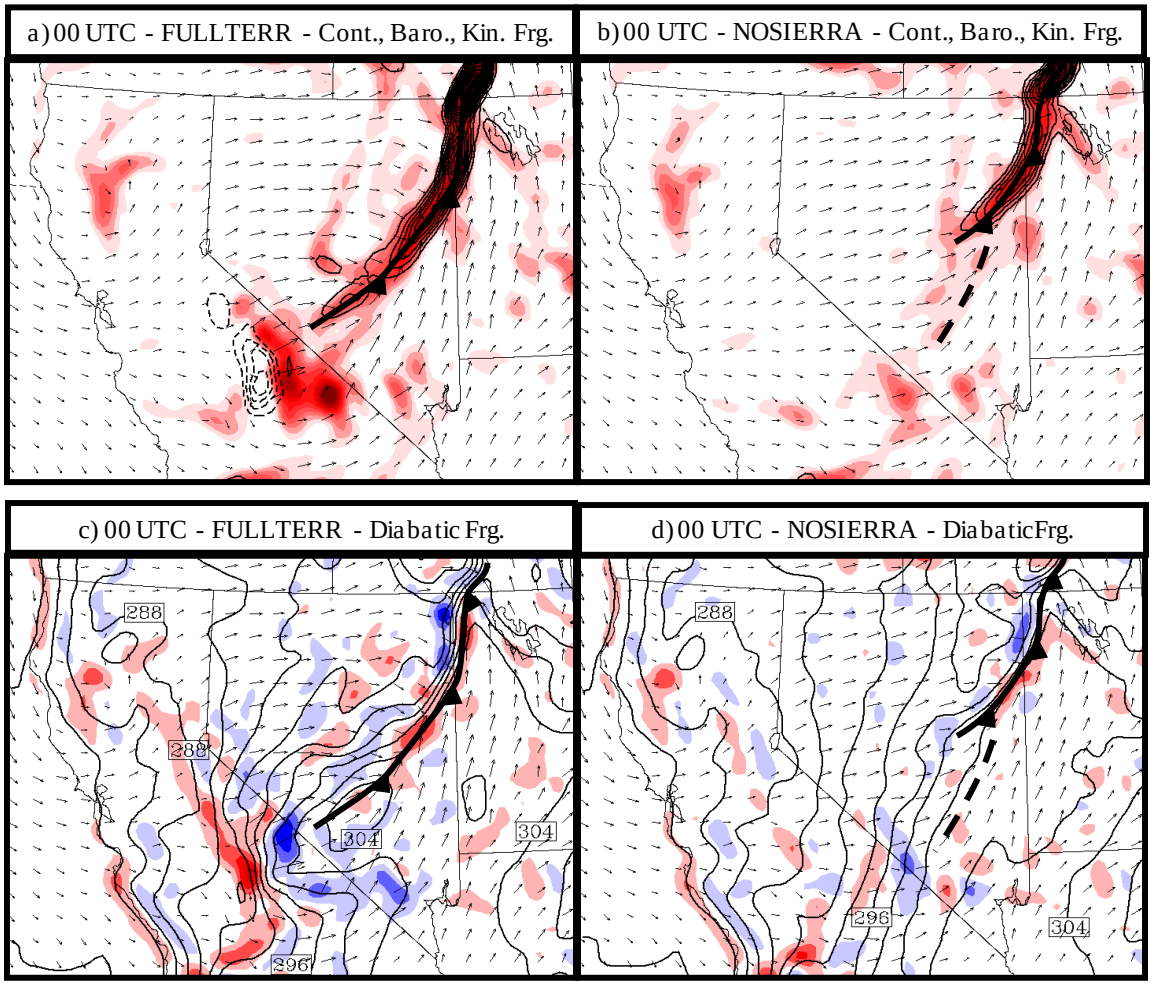

Figure 3.7. Mesoscale frontogenesis diagnostics. Lowest η-level contraction [shaded according to scale in Fig. 3.4a, x10^{-4} s^{-1}], kinematic frontogenesis [solid contours, dashed negative, every 5 K (100 km)$^{-1}$ hr^{-1}], and wind vectors [according to scale in Fig. 3.4a, m s^{-1}] for (a) FULLTERR and (b) NOSIERRA at 0000 UTC 26 Mar. Lowest η-level diabatic frontogenesis [shaded according to scale in (c), K (100 km)$^{-1}$ hr^{-1}], potential temperature (solid contours every 2 K), and wind vectors [as in (a)] for (c) FULLTERR and (d) NOSIERRA at 0000 UTC 26 Mar. Surface fronts are annotated using conventional frontal symbols, 850-hPa troughs using dashed lines, and lowest η-level airstream boundaries using dotted lines.

blocking of cool pacific air by the high Sierra is evident in FULLTERR in both plan view (cf. Figs. 3.4c, d) and cross section (e.g., compare the fates of the 292-296 K air in Figs. 3.8a, b) plots[4]. Second, greater latent heating within the windward orographic cloud is present in FULLTERR (shown implicitly at this time by greater windward precipitation/cloud cover; cf. Figs. 3.3a, b). Third, a stronger and deeper area of subsidence exists immediately in the lee of the high Sierra in FULLTERR (cf. Figs. 3.8a, b, c), vertically advecting down potentially warmer air from aloft. The latter two mechanisms are part of a process known as *airmass transformation* (e.g., Varney 1920; Giorgi and Bates 1989; Sinclair 1994; Smith et al. 2003; Smith et al. 2005), whereby the air warms and dries as it crosses a barrier. This drying also substantially reduces precipitation over Nevada (cf. Figs. 3.3a, b), reducing subcloud diabatic cooling (i.e., evaporation, sublimation, melting).

During the daytime this potential temperature anomaly grows and intensifies, reaching ~2-6 K in the prefrontal airmass by 1800 UTC (cf. Figs. 3.5c, d). In addition to the aforementioned mechanisms, differences in postfrontal cloud cover and precipitation between the two simulations now also contribute (e.g., cf. Figs. 3.3c, d). Decreased cloud cover downstream of the high Sierra allows for increased sensible heating, while the lack of precipitation eliminates subcloud cooling from evaporation, sublimation, and melting. A prefrontal sounding at 1800 UTC (Fig. 3.9) shows relatively dry air below 600 hPa and a growing dry adiabatic boundary layer below 740 hPa in FULLTERR, in contrast to NOSIERRA which is nearly saturated below 600 hPa, exhibiting features characteristic of an airmass experiencing precipitation and outflows.

[4]Potential temperature anomalies are calculated on WRF-model η levels. Differences in the height of these levels in FULLTER and NOSIERRA introduces a warm bias over the High Sierra. This region is identified with shading in Fig. 3.8c.

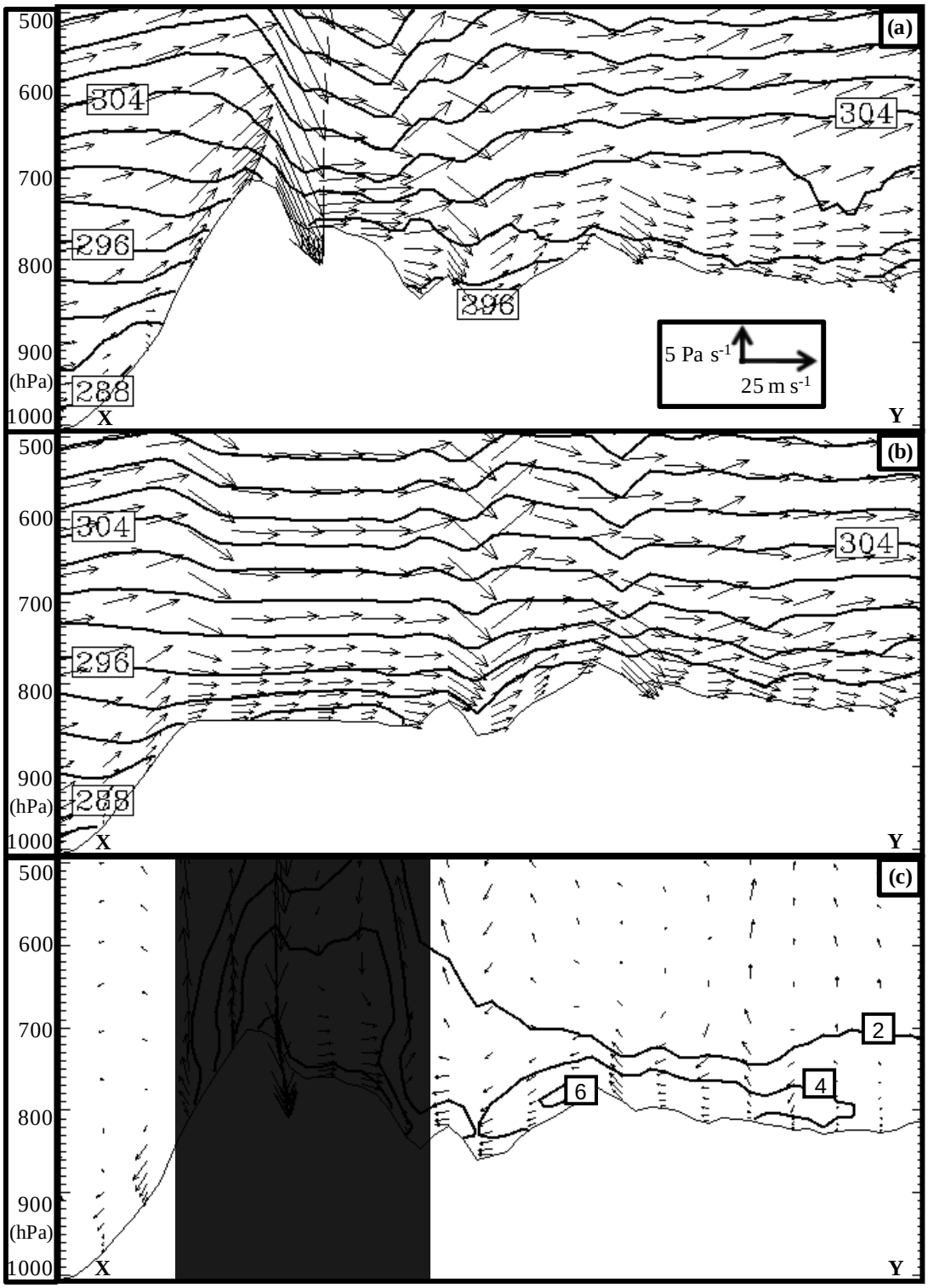

Figure 3.8. Cross sections. Potential temperature (contoured every 2 K), and circulation vectors [according to scale in (a)] at 1500 UTC for (a) FULLTERR, (b) NOSIERRA, and (c) FULLTERR-NOSIERRA difference. Shading described in text. Location XY shown in Fig. 3.4.

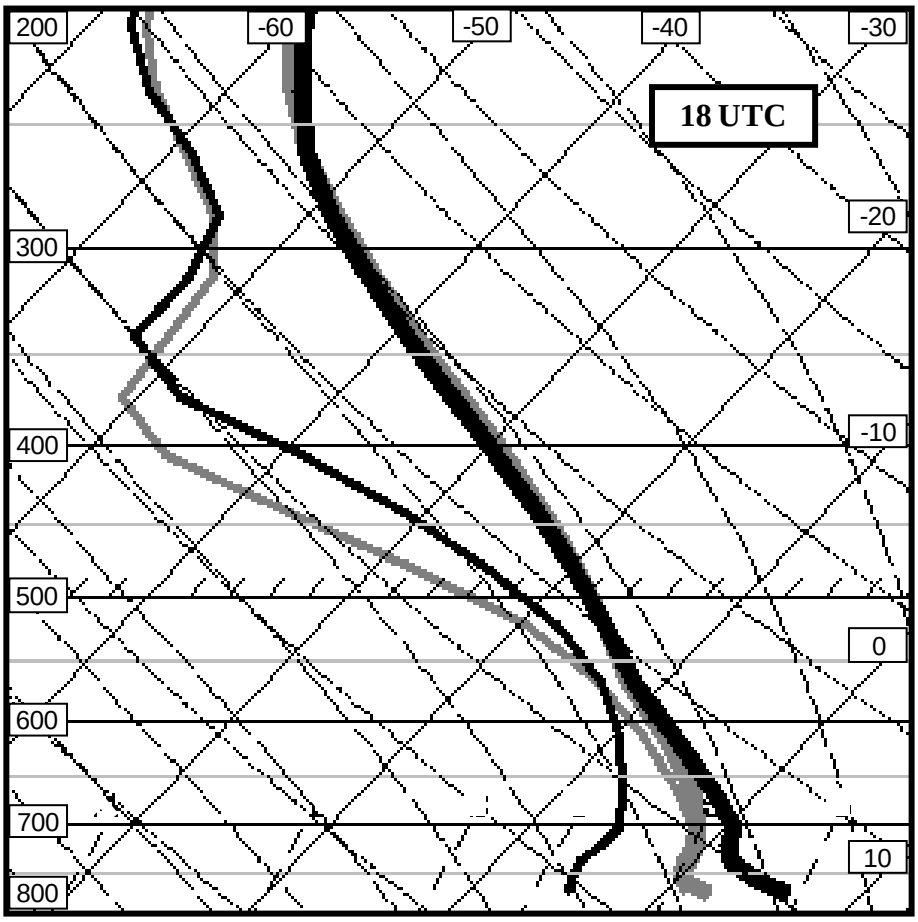

Figure 3.9. Skew-*T*/log *p* diagram. Prefrontal skew-*T*/log *p* diagram for FULLTERR (black) and NOSIERRA (gray) at 1800 UTC at locations shown in Fig. 3.5.

By 2100 UTC the prefrontal warm anomaly reaches ~2-8 K. We examine the cumulative effects of the aforementioned mechanisms with three-dimensional backward trajectories terminating at 2100 UTC. Trajectory calculations follow Petterssen (1956, p. 27) and Seaman (1987), using three-dimensional grid-scale wind fields obtained from 15-min model output, and constrained to remain on the lowest η level if they approach the model surface. Although parameterized heating rates were used qualitatively in the analysis, they lack sufficient coherency for presentation. A dense grid of trajectories for FULLTERR and NOSIERRA was used in the analysis, but for clarity we present a grid that is one fourth as dense as the initial grid (Fig. 3.10).

The trajectories in group A (dark blue, Fig. 3.10) in both simulations largely originate over north-central California and cross the northern Sierra Nevada, terminating in the postfrontal airmass. FULLTERR trajectories experience greater deflection and approach the front from a more northerly direction (cf. Figs. 3.10a, b). The most northwestern trajectories in group A (e.g., trajectories 1, 2, 7, 8) in both simulations have very similar beginning potential temperatures and net changes (Table 3.1), and accordingly terminate in a region where there is little potential temperature difference between the two simulations. Trajectories terminating in the northeastern postfrontal airmass (e.g., trajectories 3, 4) travel under more extensive cloud cover in FULLTERR (c.f. Figs. 3.3b, c), resulting in an area that is 0-3 K cooler (Fig. 3.10). Trajectories that terminate within the frontal zone (e.g., trajectories 4, 9, 10, 14) are more erratic in nature due to large changes in wind speed and direction over small temporal and spatial scales, and thus are likely less trustworthy and excluded from the analysis. Nonetheless, much of

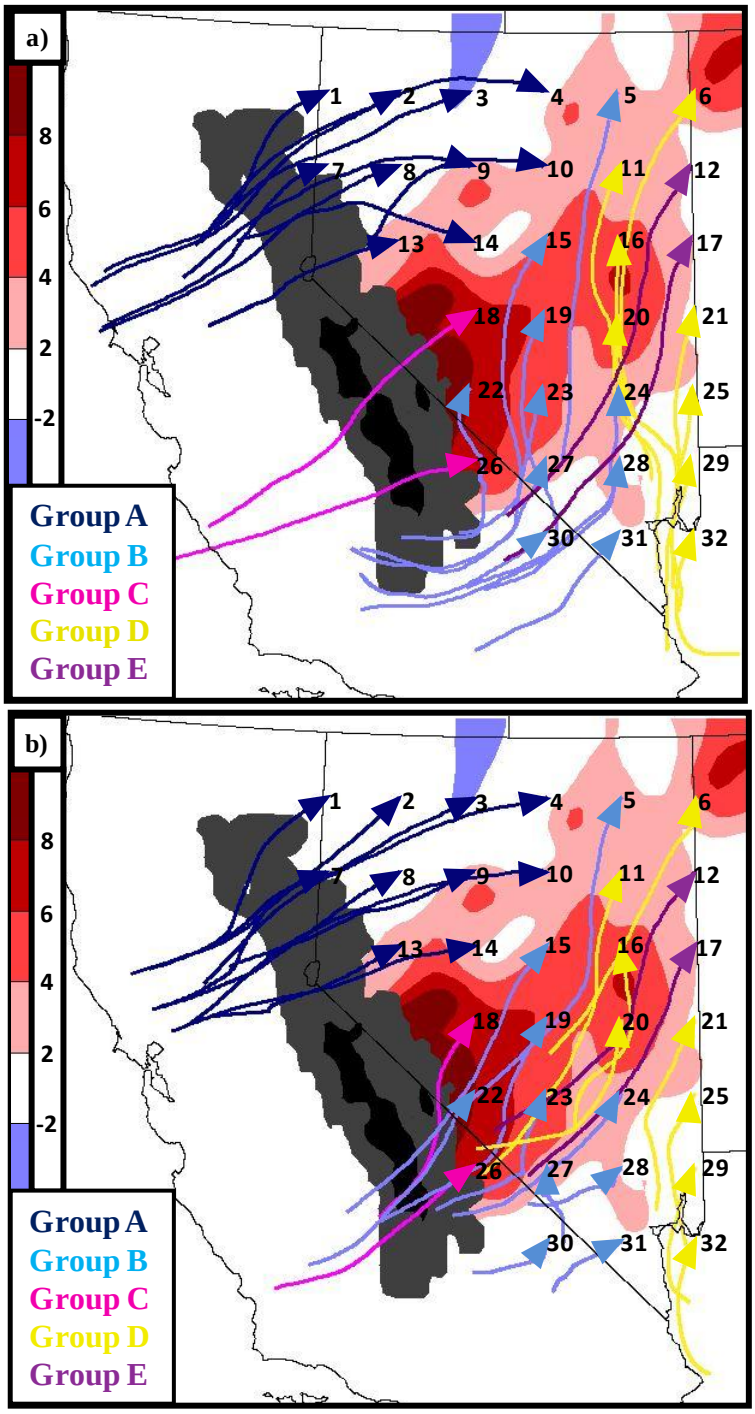

Figure 3.10. Backward trajectories ending at 2100 UTC. Trajectory numbers are labeled and grouped by color (group A = dark blue, group B = light blue, group C = pink, group D = yellow, group E = purple). Potential temperature differences at 2100 UTC (FULLTERR–NOSIERRA; shaded according to scale) for (a) FULLTERR and (b) NOSIERRA. FULLTERR-NOSIERRA terrain difference shaded (0-1000 m gray, > 1000 m black).

Table 3.1. Trajectory table. Beginning, ending, and change in potential temperatures for trajectories plotted in Fig. 3.10.

	FULLTERR	NOSIERRA	FULLTERR	NOSIERRA	FULLTERR	NOSIERRA
Trajectory Group / #	1200 UTC	1200 UTC	2100 UTC	2100 UTC	Change	Change
A / 1	286.4	286.1	291.3	289.8	4.9	3.7
A / 2	286.4	286.4	293.2	292.7	6.8	6.3
A / 3	289.3	287.6	291.4	293.9	2.1	6.3
A / 4	291.1	289.9	292.6	292.4	1.5	2.5
A / 7	286	285.2	290.5	289.7	4.5	4.5
A / 8	286.6	286.2	293.6	292.6	7	6.4
A / 9	289.1	288.3	294.4	291.2	5.3	2.9
A / 10	296.3	289.4	298	295	1.7	5.6
A / 13	284.5	286.8	295	292.8	10.5	6
A / 14	286.9	287.9	294.7	292.9	7.8	5
B / 5	299.6	297.8	302.9	300.3	3.3	2.5
B / 15	300	294.5	304.9	301.2	4.9	6.7
B / 19	298	297	305.5	300.2	7.5	3.2
B / 22	299	293.2	305.8	297.9	6.8	4.7
B / 23	294.9	299.4	304.7	298.8	9.8	-0.6
B / 24	299.3	299.4	304.7	298.8	4	0.3
B / 27	293.8	293.5	302.9	299.5	9.1	6
B / 28	298.9	297.8	302.7	300.8	3.8	3
B / 30	292.2	296.1	301.2	300.4	9	4.3
B / 31	295.6	296.5	302.2	301.7	6.6	5.2
C / 18	290.9	294.4	303.6	296.5	12.7	2.1
C / 26	294.7	293.2	305	298.1	10.3	4.9
D / 6	300	298.5	302.8	298.9	2.8	0.4
D / 11	298.1	299.3	304	301	5.9	1.7
D / 16	296.6	297.1	303.6	298.4	7	1.3
D / 20	296	296.8	303.6	298.1	7.6	1.3
D / 21	298.3	297.4	300.7	299.6	2.4	2.2
D / 25	298.8	297.4	301.4	299.7	2.6	2.3
D / 29	297.6	297	300.5	300.7	2.9	3.7
D / 32	298.4	298	302.1	302.1	3.7	4.1
E / 12	302.1	298.9	303.9	301.8	1.8	2.9
E / 17	300.9	299.6	302.1	299.7	1.2	0.1

the warm anomaly within the frontal zone can be explained by small differences in its position between the two simulations, which are larger along its southern extent.

Trajectories in group B (light blue, Fig. 3.10) in both simulations originate near the southern periphery of the Sierra Nevada and terminate in the western portion of the prefrontal airmass. Those in FULLTERR experience much greater deflection, and are more elongated due to higher wind speeds as they're forced around range (cf. Figs. 3.10a, b). FULLTERR trajectories generally experience more boundary layer heating (not explicitly shown), especially over southwest Nevada where contrasts in cloud and precipitation coverage between simulations are great (cf. Figs. 3.3a, b, and 3.3b, c). Among the southern portion of the group, some FULLTERR trajectories have lower starting potential temperatures (e.g., trajectories 23, 24, 30, 31in Table 3.1), and some NOSIERRA trajectories initially undergo diabatic cooling (perhaps due to lower wind speeds and associated radiational cooling), which results in a smaller warm anomaly over this area.

Group C (pink, Fig. 3.10) represent the small percentage of trajectories that originate near the Pacific Coast and are forced up the windward slopes of the high Sierra in FULLTERR, undergoing diabatic heating within the orographic cloud (Figs. 3.3a and c). They subsequently experience rapid leeward descent from aloft into the cloud-free airmass, where they undergo boundary layer heating (Figs. 3.3c and e, 3.10a). In NOSIERRA, although the Sierra Nevada are largely eliminated, the low, broad plateau does produce limited flow diversion (Fig. 3.10b). These parcels travel beneath the cloud cover over the plateau (rather than within it), experiencing reduced boundary layer heating in the cloudy leeward airmass (Figs. 3.3d and f). The dramatic difference in

trajectory characteristics between the simulations for this group leads to a large difference in potential temperature change (Table 3.1), resulting in large discrepancies in ending potential temperatures immediately in the lee of the high Sierra (Fig. 3.10).

Group D (yellow, Fig. 3.10) FULLTERR trajectories originate over the Colorado River Valley and terminate over eastern Nevada in the prefrontal airmass (Fig. 3.10a). Sensible heating for these trajectories is limited only by some high clouds over a portion of their path (Figs, 3.3a, c, and e). In NOSIERRA the southern half of the group (e.g., trajectories 21, 25, 29, 32 in Fig. 3.10b) is very similar to the FULLTERR trajectories (Table 3.1, cf. Figs. 3.10a, b). Due to flow differences, however, the northern half of the group (e.g., trajectories 6, 11, 16, 20 in Fig. 3.10b) originates within potentially warmer air over central and southeast Nevada (Table 3.1, Fig. 3.10b). Despite this, extensive cloud cover in NOSIERRA (Figs. 3.3b, d, and f) limits boundary layer heating, resulting in comparatively higher ending potential temperatures in FULLTERR (Table 3.1).

Group E (purple, Fig. 3.10) FULLTERR trajectories originate near the southern periphery of the Sierra Nevada in FULLTERR, having been deflected around the barrier (Fig. 3.10a), traversing beneath high clouds for a portion of their path (Figs. 3.3a and c). Reduced flow deflection in NOSIERRA causes the same parcels to instead originate in cooler air to the north (Fig. 3.10b). While some of the NOSIERRA parcels avoid diabatic cooling by staying just ahead of the precipitation (cf. Figs. 3.3b, d, 3.10b), the higher beginning potential temperatures for FULLTERR trajectories ultimately produces higher ending potential temperatures (Table 3.1).

Summary

This terrain sensitivity study demonstrates the dramatic influence that the Sierra Nevada, in particular the high Sierra, can have on Intermountain frontogenesis. Specifically, the range fundamentally alters the kinematic flow field, resulting in:

1) leeward subsidence, and associated warming and drying (i.e., airmass transformation), leading to:
   a) reduced downstream prefrontal cloud cover, increasing boundary layer heating, and
   b) near-elimination of prefrontal precipitation and associated cooling from moist diabatic processes,
2) significant blocking and deflection of cold air, and
3) enhanced contraction and kinematic frontogenesis along, and retardation of, the southern portion of the front.

These effects are most pronounced closer to the high Sierra (along the southern and central portions of the front), while over portions of the front more removed from the range (near the Nevada-Utah-Idaho border), there is little difference in frontal strength by 2100 UTC. The first two effects listed produce a significant leeward prefrontal warm anomaly, resulting in more substantial front and greater cross-front potential temperature contrast. This study confirms that the Sierra Nevada can increase downstream contraction (as was posited by Shafer and Steenburgh 2008; Steenburgh et al. 2009, and Chapter 2 of this dissertation), influence the position of the incipient front, and increase frontal strength primarily via the creation of a warm anomaly downstream of the range, the latter

being an effect that has likely not received enough attention in previous studies of Intermountain frontogenesis.

Idealized Cyclone Synoptic Variability Study

In this section we further investigate synoptic-orographic influences on Intermountain cold front evolution using simulations of idealized cyclones initialized at three different latitudes as described in Data and Methods. The resulting simulations provide insight into how fronts associated with disparate cyclone tracks interact with the orography of the western Unites States, especially the Sierra Nevada. As described in the Data and Methods section, Figure 3.2 provides an overview of the idealized baroclinic cyclone initialization. The cyclone in each simulation is located off the Pacific Coast with a cold front extending south-southwest from its center, the evolution of which will be the focus of this section.

NORTH Simulation

In NORTH the cold front makes landfall shortly before hour 23, and begins to move inland (Fig. 3.11). Baroclinity is locally enhanced along the coast (Fig. 3.11a) as deceleration of onshore flow leads to contraction and kinematic frontogenesis (Fig. 3.11b), likely due to both orographic and frictional effects. A second, weaker kinematic frontogenesis maximum exists where flow decelerates at the base of the leeward slope of the Coast Range (Fig. 3.11b; for locations of geographic name places, see Fig. 2.1). Inland, the thermal and kinematic signatures of numerous basin cold pools are evident, but with time, prefrontal southwesterly flow partially eradicates some cold pools,

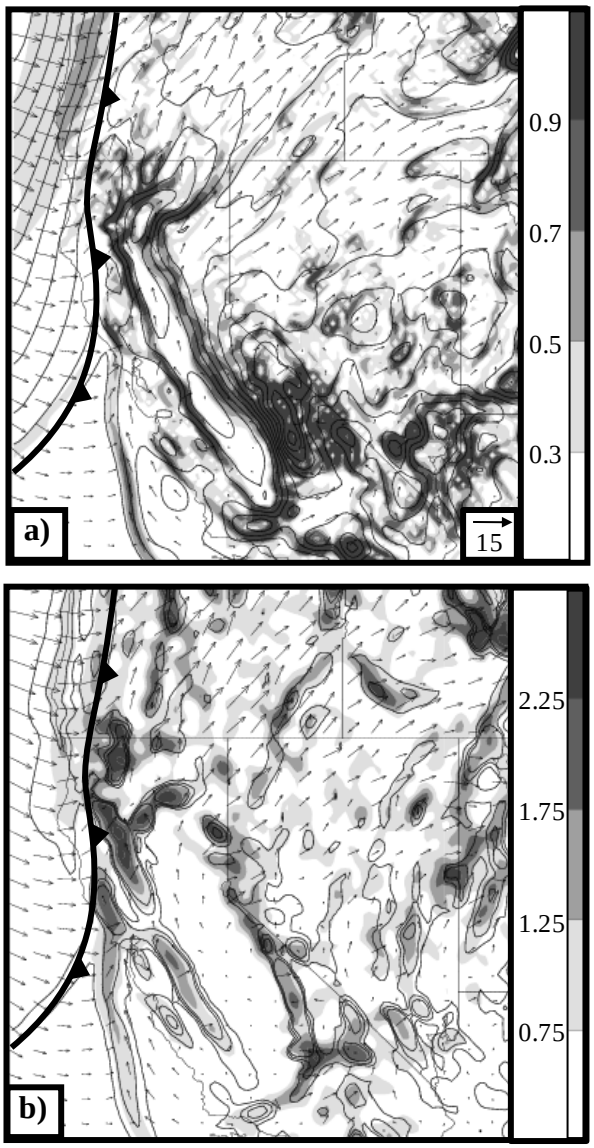

Figure 3.11. Analyses for NORTH at 23 h. (a) Lowest η-level baroclinity [shaded according to scale, K (100 km)$^{-1}$], potential temperature (contoured every 1 K), and wind vectors (m s^{-1}, according to scale). (b) lowest η-level contraction (shaded according to scale, x10^{-4} s^{-1}), kinematic frontogenesis [every 1 K (100 km)$^{-1}$ hr^{-1} starting at 0.25], and wind vectors [as in (a)]. Fronts denoted using conventional frontal symbols, and airstream boundaries denoted by dotted lines.

especially over the northern half of the plotted domain, where wind speeds are greater (cf. Figs. 3.11, 3.12).

The front pushes across the northern portion of the Intermountain West by hour 44, as the cold air is able to penetrate across the Coast and Cascade ranges of Oregon, but is largely blocked by the Coast Range of California to the south, and deflected southward along the coast where an orographic occlusion occurs (Huschke 1959; Fig. 3.12a). It should be noted that the frontal position over the Intermountain West is analyzed along the leading edge of the Pacific airmass, which is coincident with a weak wind shift. Over the Snake River Plain of Idaho, distortion of the isentropes is evident as cold air is channeled along its axis (Fig. 3.12a), similar to the observed behavior of a cold front in Steenburgh and Blazek (2001). This creates contraction along the windward slopes of the plain's southern boundary, locally enhancing kinematic frontogenesis (Fig. 3.12b). No Great Basin Confluence Zone (GBCZ) is evident over Nevada, where contraction and kinematic frontogenesis are very weak along the front (Fig. 3.12b), perhaps because blocked flow is deflected south along the high Sierra and is unable to penetrate inland around the barrier's southern periphery.

The front continues to push southward over Nevada and Utah at hour 50 (Fig. 3.13). An area of contraction associated with flow decelerating into the Great Salt Lake Basin further enhances kinematic frontogenesis along the eastern portion of the front (not shown). These terrain-induced areas of contraction appear to initially enhance kinematic frontogenesis, which continues to intensify as it moves south (Fig. 3. 13), perhaps a result of positive feedbacks associated with the geostrophic adjustment process (Hoskins and Bretherton 1972; Eliassen 1990).

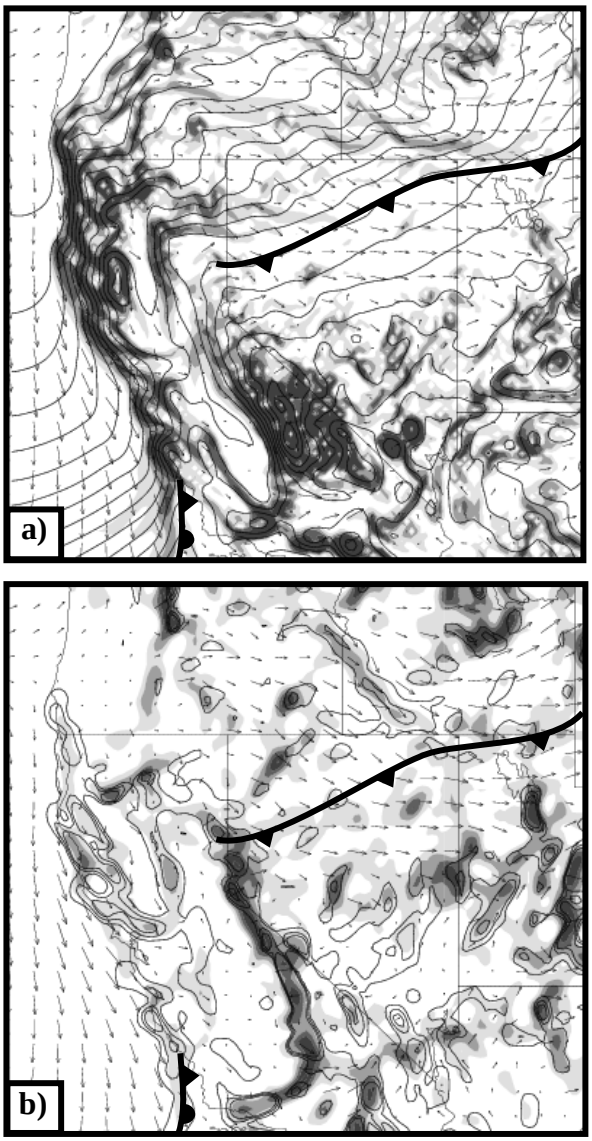

Figure 3.12. Analyses for NORTH at 44 h. (a) Lowest η-level baroclinity [shaded according to scale in Fig. 3.11a, K (100 km)$^{-1}$], potential temperature (contoured every 1 K), and wind vectors (m s^{-1}, according to scale in Fig. 3.11a). (b) lowest η-level contraction (shaded according to scale in Fig. 3.11b, x10^{-4} s^{-1}), kinematic frontogenesis [every 1 K (100 km)$^{-1}$ hr^{-1} starting at 0.25], and wind vectors (as in Fig. 3.11a). Fronts denoted using conventional frontal symbols, and airstream boundaries denoted by dotted lines.

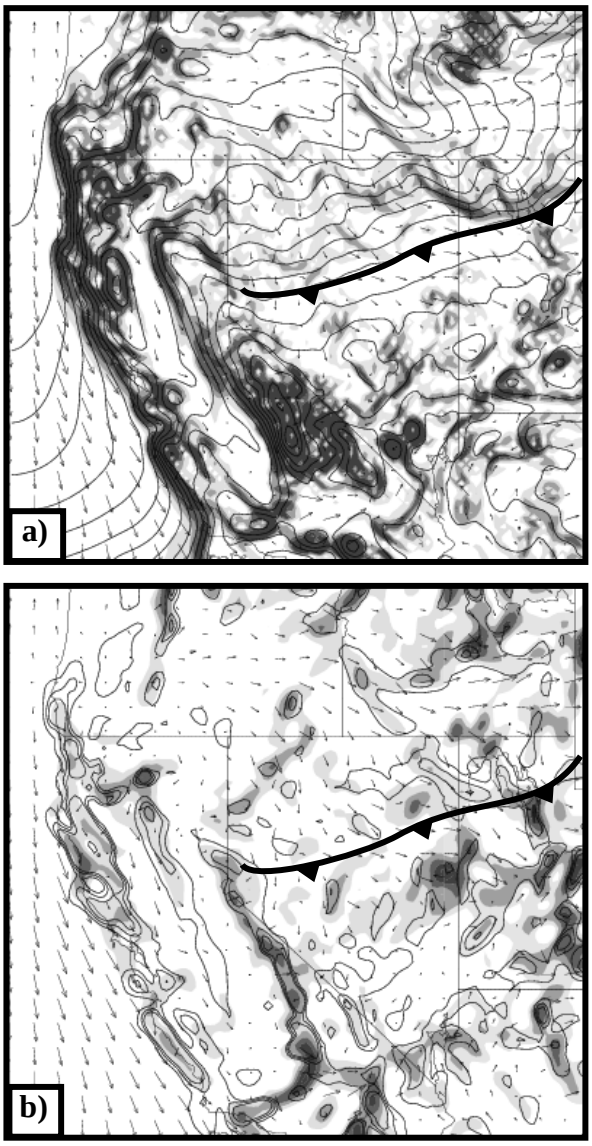

Figure 3.13. Analyses for NORTH at 50 h. (a) Lowest η-level baroclinity [shaded according to scale in Fig. 3.11a, K (100 km)$^{-1}$], potential temperature (contoured every 1 K), and wind vectors (m s^{-1}, according to scale in Fig. 3.11a). (b) lowest η-level contraction (shaded according to scale in Fig. 3.11b, x10^{-4} s^{-1}), kinematic frontogenesis [every 1 K (100 km)$^{-1}$ hr^{-1} starting at 0.25], and wind vectors (as in Fig. 3.11a). Fronts denoted using conventional frontal symbols, and airstream boundaries denoted by dotted lines.

CENTRAL Simulation

The cold front in CENTRAL makes landfall at hour 18 (not shown), moving into central Oregon and northern California by hour 23 (Fig. 3.14a). As in NORTH, flow retardation and deflection along the coastline and lower windward slopes of the Coast Range result in contraction and frontogenesis (Fig. 3.14b). Also as in NORTH, a secondary area of contraction and kinematic frontogenesis exists in the lee of the Coast Range produced by flow deceleration along the leeward slope of the Coast Range (Fig. 3.14b).

The cold air pushes across the Cascade and northern Sierra Nevada ranges into the Intermountain West at hour 36, but is largely blocked by the high Sierra, and deflected southward along the Central Valley of California (Fig. 3.15a). At this time the leading edge of the Pacific cold airmass moves through central Nevada (Fig. 3.15a), while two weakly organized airstream boundaries within broad, confluent flow extending downstream from the Sierra Nevada, locally collect and concentrate pre-existing prefrontal baroclinity (Fig. 3.15b). The northern airstream boundary appears to originate near a gradient in flow blocking near Lake Tahoe (as evidenced by a contrast in advancement of cold air; Fig. 3.15a), while the main airstream boundary to the south is characteristic of a GBCZ.

The front progresses southeastward accumulating pre-existing prefrontal baroclinity, and kinematic frontogenesis is locally enhanced as the front merges with and overtakes these airstream boundaries by hour 48 (Fig. 3.16). Geostrophic adjustment may also play a role in frontogenesis during this period of intensification. To the south of the

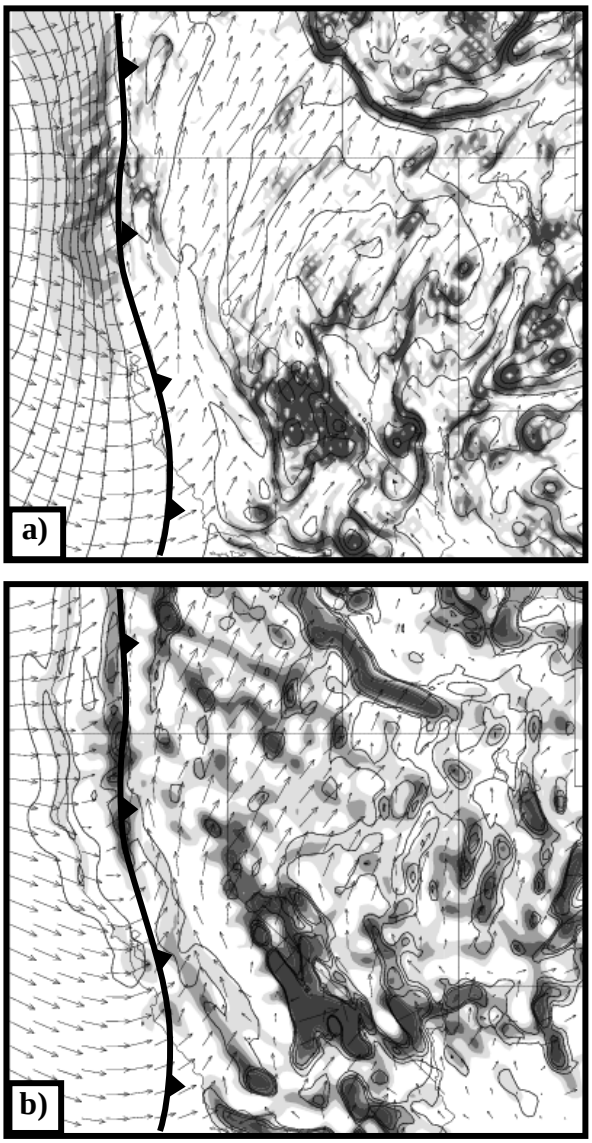

Figure 3.14. Analyses for CENTRAL at 23 h. (a) Lowest η-level baroclinity [shaded according to scale in Fig. 3.11a, K (100 km)$^{-1}$], potential temperature (contoured every 1 K), and wind vectors (m s^{-1}, according to scale in Fig. 3.11a). (b) lowest η-level contraction (shaded according to scale in Fig. 3.11b, x10^{-4} s^{-1}), kinematic frontogenesis [every 1 K (100 km)$^{-1}$ hr^{-1} starting at 0.25], and wind vectors (as in Fig. 3.11a). Fronts denoted using conventional frontal symbols, and airstream boundaries denoted by dotted lines.

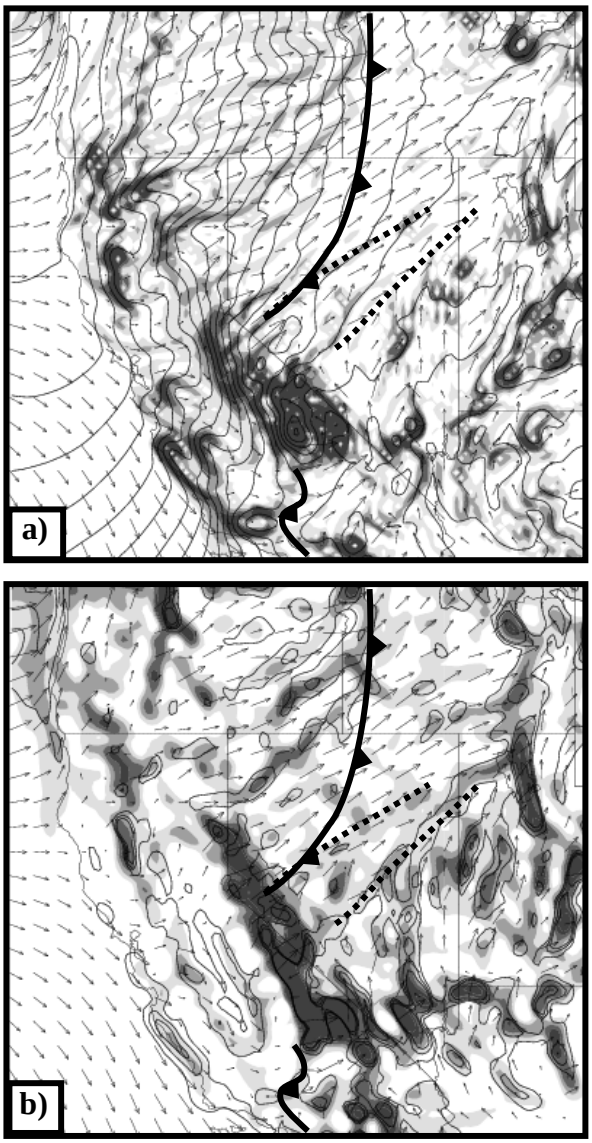

Figure 3.15. Analyses for CENTRAL at 36 h. (a) Lowest η-level baroclinity [shaded according to scale in Fig. 3.11a, K (100 km)$^{-1}$], potential temperature (contoured every 1 K), and wind vectors (m s^{-1}, according to scale in Fig. 3.11a). (b) lowest η-level contraction (shaded according to scale in Fig. 3.11b, x10^{-4} s^{-1}), kinematic frontogenesis [every 1 K (100 km)$^{-1}$ hr^{-1} starting at 0.25], and wind vectors (as in Fig. 3.11a). Fronts denoted using conventional frontal symbols, and airstream boundaries denoted by dotted lines.

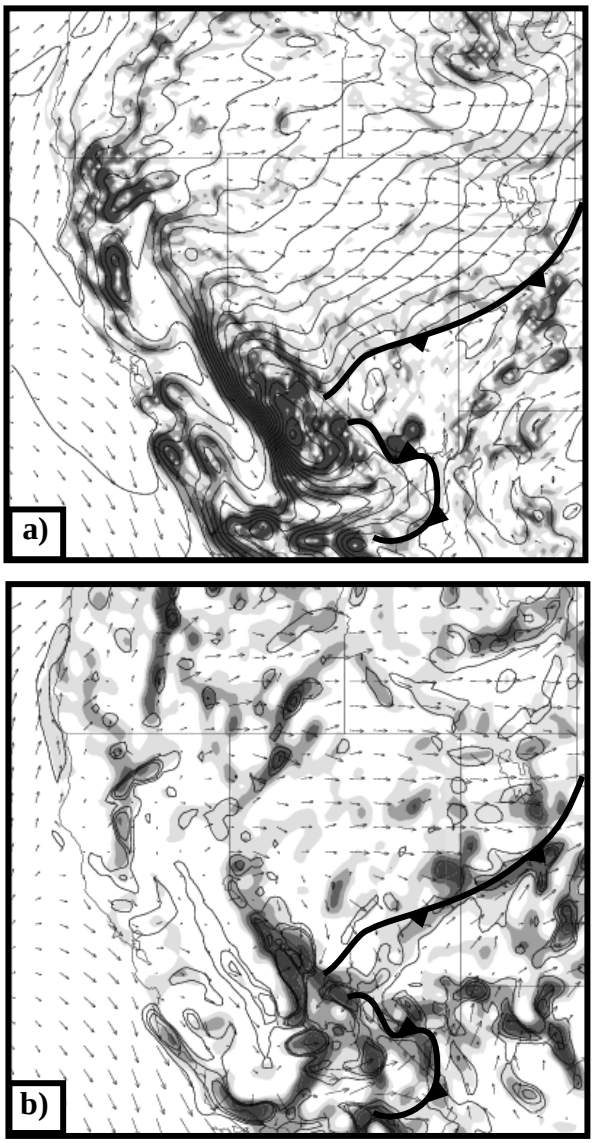

Figure 3.16. Analyses for CENTRAL at 48 h. (a) Lowest η-level baroclinity [shaded according to scale in Fig. 3.11a, K (100 km)$^{-1}$], potential temperature (contoured every 1 K), and wind vectors (m s^{-1}, according to scale in Fig. 3.11a). (b) lowest η-level contraction (shaded according to scale in Fig. 3.11b, x10^{-4} s^{-1}), kinematic frontogenesis [every 1 K (100 km)$^{-1}$ hr^{-1} starting at 0.25], and wind vectors (as in Fig. 3.11a). Fronts denoted using conventional frontal symbols, and airstream boundaries denoted by dotted lines.

high Sierra, cold air penetrates across the Mojave Desert into southern Nevada, similar to the observed and modeled evolutions of the 25 Mar 2006 case (e.g., Fig. 3.7c).

SOUTH Simulation

In SOUTH the front makes landfall at hour 24 (not shown), undergoing contraction and kinematic frontogenesis along the coast, and secondarily in the lee of the Coast Range, as in the previous two simulations. As the front moves inland at hour 30, the Sierra Nevada exert a stronger influence on this front than in previous simulations, likely due to its position and orientation relative to the barrier. Substantial blocking, flow deflection, and kinematic frontogenesis result along the windward slope of the Sierra Nevada, particularly along the central part of the range (Fig. 3.17).

By hour 45 cold air pushes across the northern Sierra Nevada and Cascade ranges as in previous simulations, while remaining blocked along the high Sierra (Fig. 3.18a). As the front pushes into central Nevada, kinematic frontogenesis and baroclinity appear to be locally enhanced downstream from an apparent gradient in flow blocking by the Sierra Nevada (similar to the kinematic structure in CENTRAL at hour 36; cf. Figs. 3.15, 3.18). This is imbedded within large scale confluent flow over Nevada, which also appears to be enhanced by the range. To the south, another cold front, associated with the blocked, deflected cold air, pushes into southwest Nevada and western Arizona, moving northward and eastward (Fig. 3.18a).

As the northern front moves southward and eastward, it encounters areas of contraction along the Nevada/Utah border where flow decelerates into the Great Salt Lake Basin (Fig. 3.18b). These contribute to kinematic frontogenesis along the front, which may be further enhanced by geostrophic adjustment, producing a fairly robust

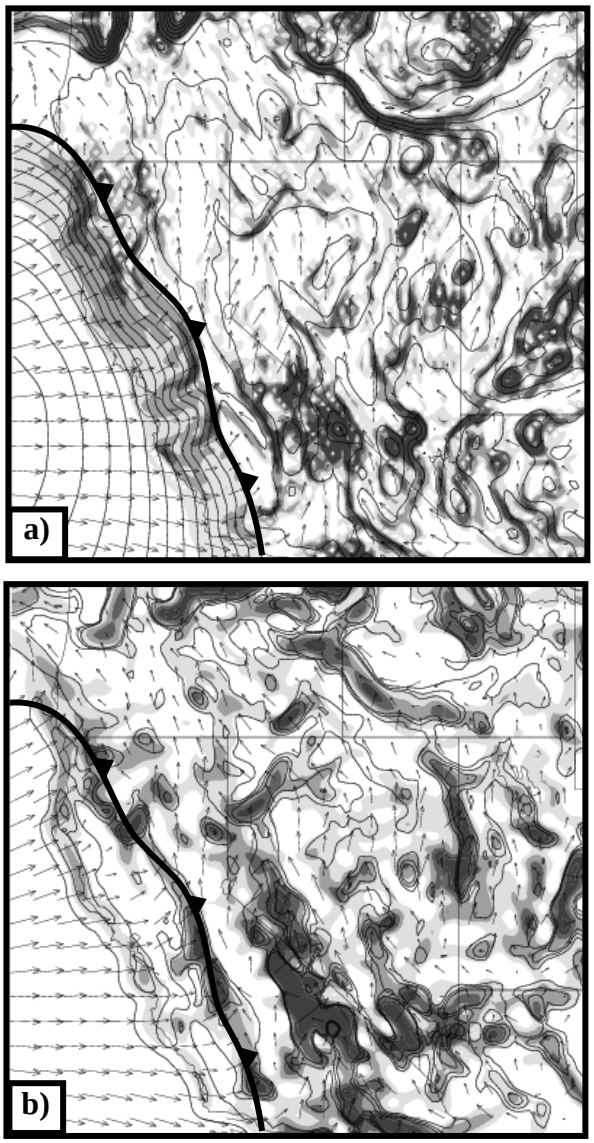

Figure 3.17. Analyses for SOUTH at 30 h. (a) Lowest η-level baroclinity [shaded according to scale in Fig. 3.11a, K (100 km)$^{-1}$], potential temperature (contoured every 1 K), and wind vectors (m s^{-1}, according to scale in Fig. 3.11a). (b) lowest η-level contraction (shaded according to scale in Fig. 3.11b, x10^{-4} s^{-1}), kinematic frontogenesis [every 1 K (100 km)$^{-1}$ hr^{-1} starting at 0.25], and wind vectors (as in Fig. 3.11a). Fronts denoted using conventional frontal symbols, and airstream boundaries denoted by dotted lines.

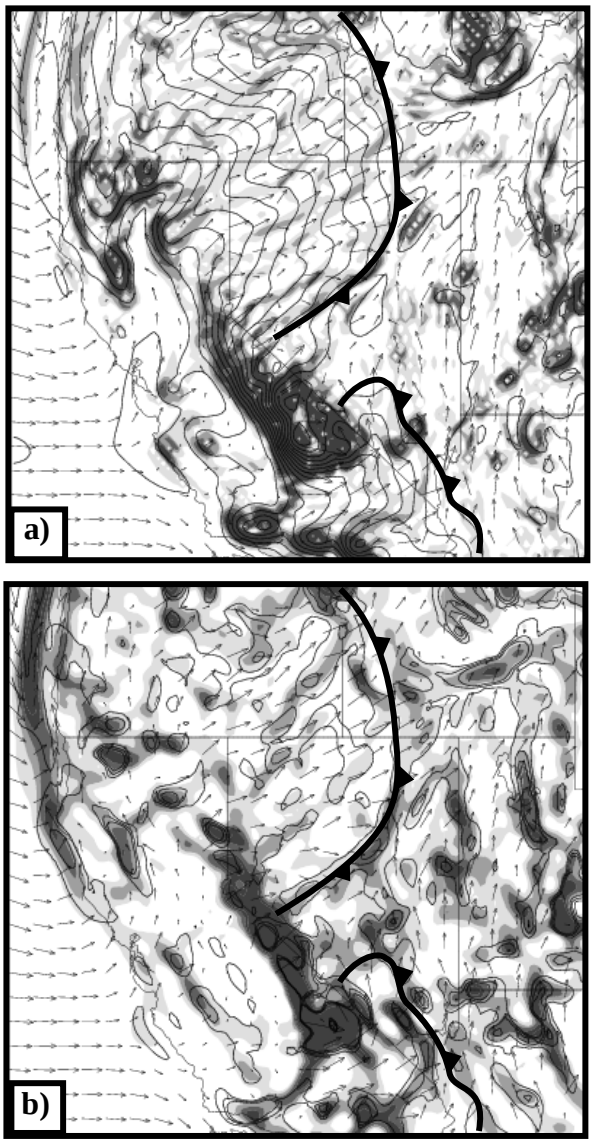

Figure 3.18. Analyses for SOUTH at 30 h. (a) Lowest η-level baroclinity [shaded according to scale in Fig. 3.11a, K (100 km)$^{-1}$], potential temperature (contoured every 1 K), and wind vectors (m s^{-1}, according to scale in Fig. 3.11a). (b) lowest η-level contraction (shaded according to scale in Fig. 3.11b, x10^{-4} s^{-1}), kinematic frontogenesis [every 1 K (100 km)$^{-1}$ hr^{-1} starting at 0.25], and wind vectors (as in Fig. 3.11a). Fronts denoted using conventional frontal symbols, and airstream boundaries denoted by dotted lines.

front over central Utah by hour 54 (Fig. 3.19). Over southern Nevada, the southern cold front (moving northeastward) meets the northern front, and the frontal evolution culminates with a nonclassical type of orographic occlusion [this differs from the classical type of orographic occlusion as defined in Huschke (1959, p. 406), wherein orography retards the warm front, accelerating the cold front catch up process].

Summary

The simulations presented in this synoptic variability study illustrate three very different frontal evolutions over the Intermountain West. In all three simulations, kinematic frontogenesis is initially enhanced along the Pacific Coast where the flow decelerates, likely due to frictional and orographic effects, and secondarily as flow decelerates in the lee of the Coast Range. The greatest blocking and enhancement occurs in SOUTH where the front travels in a direction nearly normal to the Sierra Nevada. In each simulation cold air is able to penetrate across the Cascades and the northern Sierra Nevada, but is largely blocked by the high Sierra to the south. As the fronts progress through the Intermountain West, the front in NORTH is locally enhanced by confluent flow along the southern slopes of the Snake River Plain, whereas over Nevada, there is no evidence of Sierra Nevada-enhanced contraction, and baroclinity along the front remains weak over this area. In contrast, the front in CENTRAL benefits from two apparently terrain-enhanced airstream boundaries and their associated contraction maxima. One extends roughly downstream from an area of differential flow blocking along the Sierra Nevada, whereas the other appears to be characteristic of a GBCZ (as discussed in Chapter 2). In SOUTH frontogenesis is also apparently enhanced by the Sierra Nevada, both along a concentrated contraction maximum and by large-scale

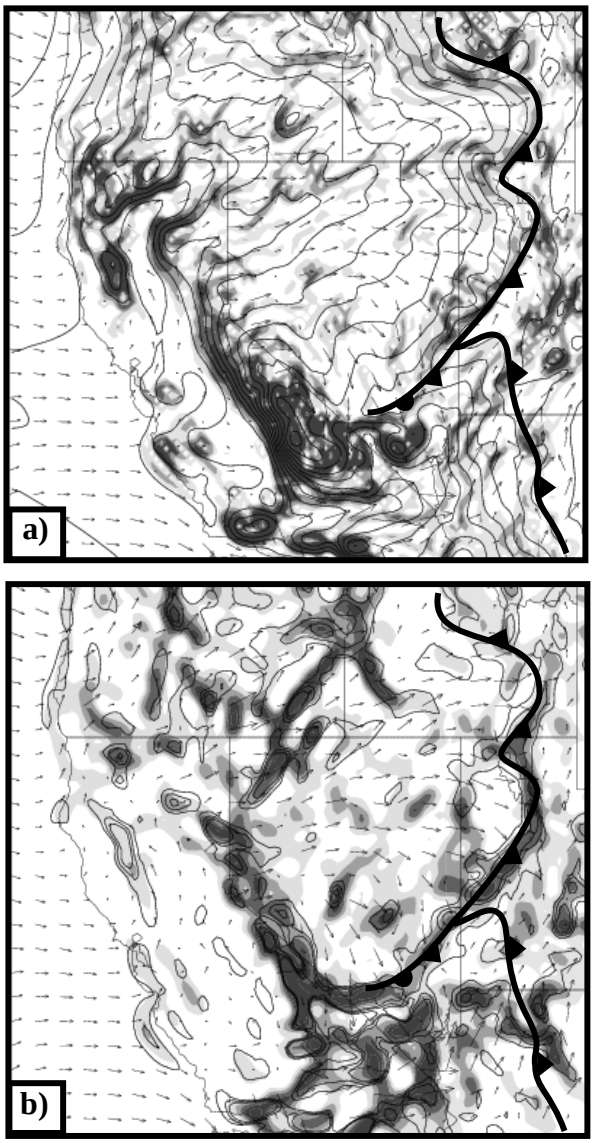

Figure 3.19. Analyses for SOUTH at 54 h. (a) Lowest η-level baroclinity [shaded according to scale in Fig. 3.11a, K (100 km)$^{-1}$], potential temperature (contoured every 1 K), and wind vectors (m s^{-1}, according to scale in Fig. 3.11a). (b) lowest η-level contraction (shaded according to scale in Fig. 3.11b, x10^{-4} s^{-1}), kinematic frontogenesis [every 1 K (100 km)$^{-1}$ hr^{-1} starting at 0.25], and wind vectors (as in Fig. 3.11a). Fronts denoted using conventional frontal symbols, and airstream boundaries denoted by dotted lines.

confluent flow over the region. In each case, after undergoing apparent orographically-induced enhancement, the front continues to intensify as it moves downstream, suggesting that geostrophic adjustment may also be contributing. Lastly, in CENTRAL and SOUTH there is a significant penetration of cold air around the south end of the High Sierra, in the latter simulation leading to a non-classical type of orographic occlusion.

The characteristics of an idealized cyclone synoptic variability study make it a valuable tool, in that it allows for a relatively controlled experiment. Although the simulations contain simplifications, their structure is more realistic than many previous idealized studies, resulting in potentially more realistic results. Along the Pacific Coast, these simulations corroborate findings of the COAST, CALJET, and IMPROVE-2 field campaigns (e.g., Braun et al. 1999a; 1999b; Colle et al. 1999; Colle et al. 2002) as well as some of the findings from idealized studies (e.g., Schumann 1987; Zehnder and Bannon 1988; Williams et al. 1992); namely that flow deceleration along the coast and the lower portion of the windward and leeward mountain slopes, in addition to windward flow deflection, can enhance kinematic frontogenesis. Inland, these simulations provide valuable new insights into Intermountain frontal evolution. For example:

- The high Sierra can effectively block cold air, while the northern Sierra Nevada and Cascade ranges do not, dramatically influencing frontal movement and orientation.
- The effect of the Sierra Nevada on downstream kinematic fields is highly dependent on the cyclone track and frontal orientation. More southerly storm tracks are more likely to generate a GBCZ downstream, which subsequently enhances frontogenesis.

- Flow deceleration into basins, perhaps due to presence of stable air within them, can locally enhance frontogenesis.
- Cold air can penetrate into the Intermountain West from the southern periphery of the high Sierra, and is favored in more southerly track storms.

References

Bannon, P. R., 1983: A semi-geostrophic model of frontogenesis over topography. *Beitr. Phys. Atmos*., **57,** 393-408.

Barnes, S. L., F. Caracena, and A. Marroquin, 1996: Extracting synoptic-scale diagnostic information from mesoscale models: The Eta model, gravity waves, and quasigeostrophic diagnostics. *Bull. Amer. Meteor. Soc.,* **77**, 519-528.

Bjerknes, J., and H. Solberg, 1922: Life cycle of cyclones and the polar front theory of atmospheric circulation. *Geofys. Publ.,* **3**(1), 3–18.

Blumen, W., and B. Gross, 1987: Semigeostrophic flow over orography in a stratified rotating atmosphere. Part I: Steady three-dimensional solutions over finite ridges. *J. Atmos. Sci*., **44,** 3007-3019.

Braun, S. A., R. A. Houze, Jr., and B. F. Smull, 1997: Airborne dual-Doppler observations of an intense frontal system approaching the Pacific Northwest coast. *Mon. Wea. Rev.,* **125,** 3131-3156.

Braun S. A., R. Rotunno, and J. B. Klemp, 1999a: Effects of coastal orography on landfalling cold fronts. Part I: Dry, inviscid dynamics. *J. Atmos. Sci*, **56**, 517–533.

Braun S. A., R. Rotunno, and J. B. Klemp, 1999b: Effects of coastal orography on landfalling cold fronts. Part II: Effects of surface friction. *J. Atmos. Sci*, **56**, 3366–3384.

Chien, F.-C., and Y.-H. Kuo, 2006: Topographic effects on a wintertime cold front in Taiwan. *Mon. Wea. Rev.,* **134**, 3297-3316.

Cohen, R. A., and D. M. Schultz, 2005: Contraction rate and its relationship to frontogenesis, the Lyapunov exponent, fluid trapping, and airstream boundaries. *Mon. Wea. Rev*., **133**, 1353-1369.

Colle, B. A., C. F. Mass, and B. F. Smull, 1999: An observational and numerical study of a cold front interacting with the Olympic Mountains during COAST IOP5. *Mon. Wea. Rev*., **127,** 1310-1334.

Colle, B. A., B. F. Smull, and M.-J. Yang, 2002: Numerical simulations of a landfalling cold front observed during COAST: Rapid evolution and responsible mechanisms. *Mon. Wea. Rev*., **130,** 1945-1966.

Davies, H. C., 1984: On the orographic retardation of a cold front. *Beitr. Phys. Atmos.*, **57,** 409-418.

Doyle, J. D., 1997: The influence of mesoscale orography on a coastal jet and rainband. *Mon. Wea. Rev*., **125**, 1465-1488.

Eliassen, A., 1990: Transverse circulations in frontal zones. *Extratropical Cyclones: The Erik Palmén Memorial Volume*, C. W. Newton and E. O. Holopainen, Eds., Amer. Meteor. Soc., 155-165.

Giorgi, F., and G. T. Bates, 1989: The climatological skill of a regional model over complex terrain. *Mon. Wea. Rev.*, **117,** 2325-2347.

Hong, S.-Y., Y. Noh, and J. Dudhia, 2006: A new vertical diffusion package with an explicit treatment of entrainment processes. *Mon. Wea. Rev.,* **134,** 2318–2341.

Horel, J. D., and C. V. Gibson, 1994: Analysis and simulation of a winter storm over Utah. *Wea. Forecasting*, **9**, 479-494.

Hoskins, B. J., and F. P. Bretherton, 1972: Atmospheric frontogenesis models: Mathematical formulation and solution. *J. Atmos. Sci*., **29**, 11–37.

Huschke, R. E., Ed., 1959: *Glossary of Meteorology.* Amer. Meteor. Soc., 638 pp..

Kurz, M., 1990: The influence of the Alps on the structure and behavior of cold fronts over southern Germany. *Meteor. Atmos. Phys*., **43**, 61-68.

Miller, J. E., 1948: On the concept of frontogenesis. *J. Meteor.*, **5**, 169–171.

O'Handley, C., and L. F. Bosart, 1996: The impact of the Appalachian Mountains on cyclonic weather systems. Part I: A climatology. *Mon. Wea. Rev.,* **124**, 1353-1373.

Olson, J. B., and B. A. Colle, 2007: A modified approach to initialize an idealized extratropical cyclone within a mesoscale model. *Mon. Wea. Rev.,* **135,** 1614-1624.

Peng, M. S., J. H. Powell, R. T. Williams, and B.-F. Jeng, 2001: Boundary layer effects on fronts over topography. *J. Atmos. Sci.*, **58,** 2222-2239.

Petterssen S., 1936: Contribution to the theory of frontogenesis. *Geofys. Publ*., **11**(6), 1–27.

Petterssen, S., 1956: *Weather Analysis and Forecasting.* Vol. 1, *Motion and Motion*

Systems, 2d ed., McGraw-Hill, 428 pp.

Schumacher, P. N., D. J. Knight, and L. F. Bosart, 1996: Frontal interaction with the Appalachian Mountains. Part I: A climatology. *Mon. Wea. Rev.*, **124,** 2453-2468.

Schumann, U., 1987: Influence of mesoscale orography on idealized cold fronts. *J. Atmos. Sci.*, **44,** 3423-3441.

Seaman, N. L., 1987: Program TRAJEC: Documentation and users guide. PSU-NWPLIB-0010-87. 95 pp.

Shafer, J. C., and W. J. Steenburgh, 2008: Climatology of strong Intermountain cold fronts. *Mon. Wea. Rev*., **136**, 784-807.

Shafer, J. C., W. J. Steenburgh, J. A. W. Cox, and J. P. Monteverdi, 2006: Terrain influences on synoptic storm structure and mesoscale precipitation distribution during IPEX IOP3. *Mon. Wea. Rev*., **134**, 478-497.

Sinclair, M. R., 1994: A diagnostic model for estimating orographic precipitation. *J. Appl. Meteor.*, **33,** 1163-1175.

Skamarock, W. C., J. B. Klemp, J. Dudhia, D. O. Gill, D. M. Barker, W. Wang and J. G. Powers, 2005: A Description of the Advanced Research WRF Version 2 NCAR Tech. Note 5, 22 pp.

Smith, R. B., Q. Jiang, M. G. Fearon, P. Tabary, M. Dorninger, J. D. Doyle, and R. Benoit, 2003: Orographic precipitation and air mass transformation: An Alpine example. *Quart. J. Roy. Meteor. Soc.*, **129,** 433-454.

Smith, R. B., I. Barstad, and L. Bonneau, 2005: Orographic Precipitation and Oregon's climate transition. *J. Atmos. Sci.,* **62,** 177-191.

Steenburgh, W. J., and T. R. Blazek, 2001: Topographic distortion of a cold front over the Snake River Plain and central Idaho Mountains. *Wea. Forecasting*, **16**, 301–314.

Steenburgh, W. J., C. R. Neuman, G. L. West, and L. F. Bosart, 2009: Discrete frontal propagation over the Sierra-Cascade Mountains and Intermountain West. *Mon. Wea. Rev*., **137**, 2000-2020.

Stoelinga, M., 2009: A user's guide to RIP version 4.5: A program for visualizing mesoscale model output. [Retrieved online 1 Dec 2009 at http:// www.mmm.ucar.edu/wrf/users/docs/ripug.htm].

Varney, B. M., 1920. Monthly variations of the precipitation-altitude relation in the central Sierra Nevada of California. *Mon. Wea. Rev.*, **48,** 648-650.

Williams, R. T., M. S. Peng, and D. A. Zanofski, 1992: Effects of topography on fronts. *J. Atmos. Sci.,* **49,** 287–305.

Yu, C.–K., and B. F. Smull, 2000: Airborne Doppler observations of a landfalling cold front upstream of steep coastal orography. *Mon. Wea. Rev.*, **128,** 1577-1603.

Zehnder, J. A., and P. R. Bannon, 1988: Frontogenesis over a mountain ridge. *J. Atmos. Sci.,* **45,** 628-644.

CHAPTER 4

CONCLUDING REMARKS

Summary of Findings

This study investigates the influence of orographic, synoptic, and diabatic effects on frontogenesis and cyclogenesis over the Intermountain West. Chapter 2 provides what is perhaps the first detailed analysis of an Intermountain cyclone and mesoscale frontal structure using the high-density MesoWest observational network. It identifies the Great Basin Confluence Zone (GBCZ) and describes its influence on the position and strength of incipient cold frontogenesis. Cyclogenesis occurs along this incipient frontal boundary as QG forcing for ascent moves into the area. Diabatic processes account for up to 40% of baroclinity along parts of the front, and likely aid in the subsequent rapid scale collapse. The last part of the case study describes the mesoscale frontal evolution over northern Utah, documenting the dramatic frontal distortions that complicate frontal analysis and short-range forecasting over the region's basin-and-range topography.

Chapter 3 further examines synoptic and orographic influences on Intermountain cold front evolution using a real-data terrain sensitivity study and a series of idealized baroclinic cyclone simulations. The real-data terrain sensitivity study shows how the Sierra Nevada, in particular the high Sierra, block the penetration of cold air into the Intermountain West and warm and dry the downstream prefrontal airmass. The warmer

prefrontal air creates a substantially larger cross-front potential temperature contrast. The Sierra Nevada also enhance contraction along the front and retard its progression over southern and central Nevada. The idealized baroclinic cyclone simulations further demonstrate the ability of the Sierra Nevada, particularly the high Sierra, to dramatically alter frontal evolution over the region. The simulations show that cold air is able to penetrate relatively easily across the lower northern Sierra Nevada and Cascade Ranges, but is strongly blocked by the high Sierra, ultimately determining the orientation and path of the cold front as it penetrates into the Intermountain West. Further, the results show that the propensity of the barrier to produce a downstream GBCZ, which is important to frontogenesis over the Intermountain West, depends on cyclone track and frontal orientation.

Future Work

While this study adds substantially to our knowledge and comprehension of cold-front and cyclone evolution over the Intermountain West, there is still a great deal we do not understand. Additional observational case studies and real-data model simulations of events will undoubtedly add further insight into the mechanisms contributing to cyclogenesis and frontogenesis over the region, as the limited number of studies conducted to date (e.g., Horel and Gibson 1994, Steenburgh and Blazek 2001; Steenburgh et al. 2009; Chapter 2 of this dissertation) show a great deal of variation in their respective evolutions.

To further understand synoptic-orographic interaction and its importance in Intermountain frontal evolution (in particular, the necessary conditions for the formation of the GBCZ), almost limitless possibilities exist in the realm of idealized baroclinic

cyclone simulations. For example, the initial cyclone and frontal intensity could be altered to examine the effect of a stronger front and/or cross-barrier flow, the tropospheric lapse rate could be changed to investigate stability effects, or the direction of background flow (zonal in the idealized simulations presented here) could be varied, in addition to countless alternate terrain modification possibilities (including removing terrain completely).

Our understanding of cyclones and fronts over this historically data-void region has progressed significantly in recent years. This is largely made possible by the high-density MesoWest observational network and the higher-resolution modeling capabilities available today. As our understanding of cyclones and fronts over the region continues to expand, we will be better able to predict the dramatic sensible weather changes that can accompany these events, an increasingly important task in this rapidly growing region.

References

Horel, J. D., and C. V. Gibson, 1994: Analysis and simulation of a winter storm over Utah. *Wea. Forecasting*, **9**, 479-494.

Steenburgh, W. J., and T. R. Blazek, 2001: Topographic distortion of a cold front over the Snake River Plain and central Idaho Mountains. *Wea. Forecasting*, **16**, 301–314.

Steenburgh, W. J., C. R. Neuman, G. L. West, and L. F. Bosart, 2009: Discrete frontal propagation over the Sierra-Cascade Mountains and Intermountain West. *Mon. Wea. Rev*., **137**, 2000-2020.